5-2010

# Characterization of plutonium particles originating from the BOMARC accident -1960

Richard Charles Gostic
*University of Nevada Las Vegas*

# CHARACTERIZATION OF PLUTONIUM PARTICLES ORIGINATING FROM THE BOMARC ACCIDENT - 1960

By

Richard Charles Gostic

Bachelor of Science
Dowling College
1995

Master of Science
Massachusetts Institute of Technology
2002

A dissertation submitted in partial fulfillment of
the requirements for the

**Doctor of Philosophy Degree in Radiochemistry**
**Department of Chemistry**
**College of Science**

**Graduate College**
**University of Nevada, Las Vegas**
**May 2010**

UNLV
UNIVERSITY OF NEVADA LAS VEGAS

THE GRADUATE COLLEGE

We recommend the dissertation prepared under our supervision by

**Richard Charles Gostic**

entitled

**Characterization of Plutonium Particles Originating from the BOMARC Accident -1960**

be accepted in partial fulfillment of the requirements for the degree of

**Doctor of Philosophy in Radiochemistry**
Chemistry

Kenneth R. Czerwinski, Committee Chair

Kenton J. Moody, Committee Member

Ian D. Hutcheon, Committee Member

Gary Cerefice, Graduate Faculty Representative

Ronald Smith, Ph. D., Vice President for Research and Graduate Studies
and Dean of the Graduate College

**May 2010**

ABSTRACT

**Characterization of Plutonium Particles Originating from the BOMARC Accident - 1960**

by

Richard Charles Gostic

Dr. Kenneth R. Czerwinski, Examination Committee Chair
Professor of Chemistry
Chair of the Department of Radiochemistry
University of Nevada, Las Vegas

Within the U.S. arsenal, 32 accidents with nuclear weapons were reported between 1950 and 1980. One of these accidents occurred at McGuire AFB in 1960. A BOMARC missile armed with a nuclear warhead caught on fire and as a result the warhead was destroyed. Sub-millimeter particles consisting of weapons grade plutonium (WGPu) produced by this accident were distributed around the site and remained in the environment for 47 years.

Soil cores known to contain WGPu particles produced by this accident were obtained. The particles were localized and removed from the soil with the aid of high resolution computed tomography. The isotopic composition of the particles and the date of manufacture of the Pu were estimated using a combination of alpha and gamma spectroscopy. Scanning electron microscopy was used to study the surface morphology of the particles; energy dispersive spectroscopy and synchrotron based x-ray fluorescence were used to determine the composition and elemental distributions of the particles. The results of these experiments and their application to the field of nuclear forensic analysis are discussed in this thesis.

ACKNOWLEDGEMENTS

I would like to take this opportunity to express my gratitude to those individuals that helped me achieve this milestone. First, I thank my thesis advisor, Ken Czerwinski for having the foresight and tenacity to build a multi-disciplinary radiochemistry program at UNLV. I have benefited from his hard work and dedication to the program and would like to thank him in particular for his efforts. I thank the members of my thesis committee for their patience and support throughout my research and writing. In particular, I thank Ken Moody for his thoughtful commentary and hours of time spent reviewing this body of work. Gary Cerefice and Ian Hutcheon provided a great deal of guidance and support through this process and I thank them for their time and effort. This thesis would not have been possible without the assistance of Craig Bias, Steven Rademacher and the cooperation of Cabrera Services in retrieving the particles from the BOAMRC site. And lastly I thank beamline scientists of MR-CAT, Jeremy Kropf and Jeff Fortner. Without their commitment and effort and many late nights the synchrotron experiments would not have been possible. And last, but most importantly, I thank my wife Julie for her help, patience, support and love through this process. Without her this never would have been possible.

TABLE OF CONTENTS

LIST OF TABLES

LIST OF FIGURES

# CHAPTER 1

# INTRODUCTION

## 1.1 Justification of Work

The work presented herein is the result of the study of weapons grade plutonium (WGPu) particles, commonly called ‘hot particles’ (1) and the soils that have contained these particles from a specific site. The particles were produced and dispersed by the accidental combustion of a nuclear weapon in 1960 and have provided an opportunity to advance both environmental science and nuclear forensic analysis through the development and refinement of analytical techniques focused on WGPu particle characterization.

Accidents involving nuclear weapons and the dispersal of radioactive components are more common than imagined. Within the U.S. arsenal, 32 accidents with nuclear weapons were reported between 1950 and 1980 (2). Fortunately less than half of the accidents produced any contamination by or dispersal of radioactive materials (2) and none have resulted in nuclear detonations. Above-ground intentional combustion or non-nuclear destruction of nuclear weapons, resulting in the creation and dispersion of WGPu and U has been carried out as part of weapons development programs and weapons safety testing. Both the United States, at the Johnston Atoll (1) and the British government at the Maralinga site in Australia (3) carried out these types of tests. Outside of the weapons handling and testing community, facilities involved with the production and handling of nuclear material have also accidentally produced and released Pu and U particles. The most famous example is the 1986

Chernobyl accident that produced 1-100 μm particles that contained U, Pu and fission products (4). The Rocky Flats Plant near Golden, Co released WGPu particulates between 1952 and 1989 through several mechanisms including fire and windblown releases from outdoor waste storage (5). Uranium particles were released between 1952 and 1957 from two graphite-moderated, air-cooled reactors at Windscale, U.K. (6).

## 1.2 A New Need: Nuclear Forensic Analysis

The project was anticipated to proceed as a study of WGPu particles and their interaction with the near field environment. As the work progressed, it became clear that the study of these WGPu particles could fill a new need, the refinement and development of techniques that could be applied to pre-detonation nuclear forensic analysis (7). Analysis of these particular WGPu particles could help to develop techniques that could be applied to samples originating from a radiological dispersive device (RDD). This is based on the formation conditions that may be very similar to those experienced by materials released by the detonation of a RDD. Thus, the research effort focused on forensic analysis to better fit the new 'need'.

As an example of meeting the forensic challenge, a new technique has been developed for forensic analysis is the imaging of WGPu particulates by CT (computed tomography) in soil cores (Chapter 3). This technique localizes the WGPu particles in soil cores with micrometer accuracy for easy removal and helps identify other materials, such as solder glass and ion exchange beads, that

would have been passed over by conventional radioanalytical technique. This technique has also benefited environmental work as the high precision images afforded by CT makes it possible to conduct precision microbiological studies on undisturbed soils immediately around the WGPu particle.

## 1.3 The BOMARC Hot Particles: Overview

### 1.3.1 The Accident

On June 7, 1960 an accident occurred at the McGuire Air Force base in New Egypt, New Jersey involving a Boeing Michigan Aeronautical Research Center (BOMARC) air defense missile (Figure 1). A high pressure He tank that serviced the liquid fueling system of the missile exploded and led to the rupture of the primary fuel tank. The missile, though in ready storage condition (i.e. permitting launch in 2 minutes), caught fire and burned but the high explosives associated with the warhead did not detonate (2,8,9,10).

Fire suppression began 30 minutes after the first explosion was heard and continued throughout the night. Large volumes of water were used to suppress the fire and decrease the risk of airborne contamination, which resulted in most of the on and off-site contamination (2). On June 8, 1960, steps were begun to mitigate the spread of contamination including the complete removal of the missile wreckage and the launcher. The interior and exterior walls of the shelter were covered in thick paint to fix contamination on low dose surfaces and the pit inside the shelter was back filled with dirt and cemented over. Additional asphalt and concrete were poured over the apron in front of the missile shelter and

around the drainage ditch that collected some of the contaminated water during fire suppression (11,12). An aerial picture of the site from 2002 is provided (Figure 2).


**Figure 1.** Boeing Michigan Aeronautical Research Center (BOMARC) Missile

The site remained active until 1972 and routine monitoring of well water and the integrity of the cement and asphalt controls were conducted on a regular basis. In 2002, a site remediation campaign began and almost 17,000 $m^3$ of contaminated material was removed from the site (11). During this campaign, analyses of the excavated material determined the presence of WGPu hot particles and prompted additional soil excavation in 2007 (13).

**Figure 2**. Pre-2002 aerial view of the BOMARC site provided by Cabrera Services. Note the white patch in the upper left hand corner, the concrete poured to cover the affected area and shelter 204 (roof missing), the site of the fire.

1.3.2 Material Released By The Accident

The initial estimate of the amount of Pu and U released on the site (or that was unaccounted for) is provided (Table 1) (12). In a recently published report (11), the Air Force and Department of Energy (DOE) estimated that an upper limit of 300 g (post-remediation) of WGPu still remains on the site but no mention was made of remaining U levels. The original Pu isotopic composition of the weapon estimated by Los Alamos National Laboratory (LANL) is given as a

function of mass fraction (Table 1) for an estimated chemical separation date of 1958 (14).

**Table 1.** Plutonium isotopics of the BOMARC weapon material (14).

| Original Composition in 1958 | | | | Site Contamination |
|---|---|---|---|---|
| | **Mass (%)** | **Activity (%)** | **Half- Life (years)** | |
| **$^{238}$Pu** | 0.000099 | 2.95 | 6.27E+07 | 100 -1500 g released (300g remaining on site[3]) |
| **$^{239}$Pu** | 0.937 | 10.10 | 2.15E+09 | |
| **$^{240}$Pu** | 0.056 | 2.21 | 4.70E+08 | |
| **$^{241}$Pu** | 0.0047 | 84.75 | 1.80E+10 | |
| **$^{242}$Pu** | Negligible | Negligible | | |
| **$^{241}$Am** | Not reported | Not reported | 0.00E+00 | |
| **$^{235}$U** | None reported | | | 300 g unaccounted for |
| **$^{238}$U** | None reported | | | 300 g unaccounted for |

The major isotopic constituents by mass of the WGPu are $^{239}$Pu and $^{240}$Pu, with less than 7 % by mass of $^{240}$Pu. Due to the relatively long half lives of $^{239}$Pu and $^{240}$Pu, the radioactivity contribution from these isotopes is only 12.3 %. The primary source of radioactivity in the 1958 material was the relative short-lived beta emitter, $^{241}$Pu (Table 2). With knowledge of the half life for the radioactive decay of each of the parent isotopes, the decay modes and the half lives of the daughters, the build-up of the daughters and granddaughters can be modeled as a function of time using the Bateman equations (15). Using the 1958 mass fraction values as a starting point, the present-day mass fractions of the parent Pu isotopes and their associated daughters have been calculated and are presented (Table 2). The isotope $^{237}$Np, though not a daughter of the listed Pu

isotopes, is the granddaughter of $^{241}$Pu, from the decay of both $^{241}$Am and $^{237}$U, and does make a minor contribution to the mass fraction in 2009.

**Table 2.** Mass fraction corrected for decay (51 years) and build up of Pu daughters. Half life and decay mode data are from (16).

| | Mass Fraction 2009 | Half Life (years) | Primary Decay Mode | Activity Fraction 2009 |
|---|---|---|---|---|
| **$^{238}$Pu** | 0.00007 | 87.7 | Alpha | 0.0089 |
| **$^{239}$Pu** | 0.937 | 24110 | Alpha | 0.457 |
| **$^{240}$Pu** | 0.0558 | 6561 | Alpha | 0.099 |
| **$^{241}$Pu** | 0.0004 | 14.290 | Beta | 0.324 |
| **$^{242}$Pu** | Negligible | 3.75 E5 | Alpha | 0.0000 |
| **$^{241}$Am** | 0.0041 | 432.7 | Alpha | 0.110 |
| **$^{237}$U** | 0.0000 | 6.75 | Beta | 0.0000 |
| **$^{237}$Np** | 0.0002 | 2.16 E6 | Alpha | 0.0000 |
| **$^{236}$U** | 0.0003 | 2.342 E5 | Alpha | 0.0000 |
| **$^{235}$U** | 0.0014 | 7.04 E8 | Alpha | 0.0000 |
| **$^{234}$U** | 0.00003 | 2.46 E5 | Alpha | 0.0000 |

1.3.3 On-site Collection

On June 29, 2007 UNLV researchers traveled to the BOMARC site and with assistance from the onsite Cabrera Services staff and the United States Air Force, a set of samples were collected. This sample set consisted of 19 soil cores that were 25-34 cm in length and 5.1 cm in diameter, 18 small samples (each less than 50 $cm^3$ of soil) that contained hot particles and 9 bulk soil samples (bagged) that contain elevated activity, but could not be collected as a core.

Soil cores were collected from three areas on the site (Figure 3), outside the restroom facility (Figure 4), in a grassy field east of the firehouse and in a low

activity area south of the eastern missile shelter block. High gamma activity areas had been located from previous in-situ gamma site surveys and were marked with flags by Cabrera Services. Using the flagged areas as a guide, a field instrument for detection of low-energy radiations (FIDLER- Ludlum 2221) and a 51 mm steel pipe flange were used to pinpoint the gamma emissions produced by decay of $^{241}$Am. A more detailed explanation of the coring process is presented in Chapter 2.

**Figure 3.** Areas sampled in 2007. Upper red square is the restroom facility, lower red square is the firehouse. The green square is the area where reference cores were taken. Aerial Image provided by Cabrera Services.

**Figure 4**. Outside the restroom facility. Notice the concrete apron and the orange flags designating areas of elevated activity

## 1.4 Scope of Work

Four primary tasks were undertaken to characterize the hot particles and the soils that contain them.

- Separation of hot particles from soil cores (Chapters 3 and 4)
- Characterization of the distribution of radioactivity in the soil cores containing hot particles (Chapter 4)
- Radioanalytical characterization of the hot particles (Chapters 6 and 7)
- Imaging of hot particles (Chapter 5)

Summaries of each task and the analytical methods used to complete each task and the primary results are given below. Each task is described in more detail in subsequent chapters.

### 1.4.1 Separation of Hot Particles from Soil Cores

The purpose of this task was to design a method to replace or improve the separation methods based on the sequential splitting of samples. The process of sequential splitting involves breaking a sample into progressively smaller sections until the segment containing the hot particle is reduced to a few grains. This technique requires substantial handling of the samples which can damage the hot particle, destroys all spatial information and increases the risk of contamination. This method may be required for loose samples or small hot particles, and its effectiveness has been greatly improved through the use of 2-D digital imaging (17).

High-resolution X-ray computed tomography, a non-destructive imaging technique that can build three dimensional (3-D) data sets based on the differential attenuation of x-rays by materials of different atomic number (Z) and densities. It has been used to image the cores and create maps of high density, high Z materials within the core volume (18). Because hot particles contain high Z (92 - 95) elements relative to the soil (bulk Z < 26), they preferentially attenuate x-rays, making discrimination of hot particles from the surrounding soil possible providing the high Z particles occupy a sufficiently large volume. Five soil cores from a sample set collected in 2007 from the accident site were imaged using this technique and the primary hot particle in each core was located using the 3-D data set.

With micron scale maps of the high Z materials, the soil cores can be disassembled and the hot particles removed while preserving spatial information.

Some of the benefits of this technique are minimizing material handling, reducing the possibility of damage to the hot particle and accidental contamination of the work area, and facilitating the sampling of undisturbed soils around the radioactive source for chemical and biological studies. The primary limitation of this method is the spatial resolution that can be achieved. In 51 mm soil cores only hot particles >100 μm can be mapped. A more detailed description of the CT analysis studies is provided in Chapter 3.

1.4.2 The Distribution of Radioactivity in Soil Cores Containing Hot Particles

The purpose of this task was to profile depth, or characterize the distribution of $^{241}$Am along the vertical axis of the 5 soil cores imaged by CT. This task was accomplished by parsing the soil cores into 3.5 mm slices and then performing gamma spectroscopy on each slice. For these experiments, two high resolution planar thin window Canberra Broad Energy Germanium (BEGE) detectors were used to quantify the 59.5 keV gamma emission from $^{241}$Am in each slice. The data from each slice of a core was compiled into a data set representing the $^{241}$Am concentration in the soil as a function of depth.

Two distinct $^{241}$Am distribution patterns were observed in the cores. In some of the cores, $^{241}$Am was concentrated in the slice that contained the hot particle and the concentration dropped off exponentially as a function of depth. Other cores also exhibited high $^{241}$Am concentrations in the slice that contained the hot particle, but also presented concentration spikes in slices not associated with the hot particle.

To determine if the distribution of $^{241}$Am in these slices, was diffuse or particulate, gas proportional counting (GPC) was used. Gas proportional counting is a method primarily used for quantification of alpha and beta particles, based on their interaction with a gas in the presence of a high potential field. When a charged particle collides with the gas, ion pairs are produced that generate a current and the detectable signal. Alpha and beta particles emitted from the surface of the soil would detected by the GPC. Those emitted below the surface of the soil may be attenuated and not counted by the instrument. By changing the surface of the sample, or stirring the dirt, particles will be displaced throughout the soil volume. This process could be repeated several times and the alpha and beta signal from each experiment recorded. If a steady signal over many experiments was observed, the activity is diffuse in nature; however, if the signal varies, or exhibits spikes between experiments then the distribution is particulate in nature.

It has been determined that the $^{241}$Am distributions within individual slices was due to both diffuse and particulate distributions, though the majority of the activity tended to be associated with particles. Both the gamma spectroscopy and gas proportional data indicate that the bulk of $^{241}$Am was not homogenously distributed in the soil at either the macro (core) or micro (slice) scales. A more detailed description of this work is provided in Chapter 4.

### 1.4.3 Radioanalytical Characterizations of Hot Particles

Characterization of hot particles removed from the soil cores and 18 additional small samples collected from the accident site was performed using

alpha spectroscopy and gamma spectroscopy. Alpha spectroscopy is a technique used to identify the energy and quantity of alpha particles emitted by the decay of radioactive material. In many cases the energies and ratios of the emitted alpha particles are unique to individual isotopes and can be used to identify and quantify the amount of a specific isotope present in a sample. Unlike gamma spectroscopy, alpha spectroscopy must be performed in a vacuum and with thin samples to avoid attenuation of emitted particles.

Alpha spectroscopy was performed on thick, intact hot particles As expected this technique provided poor spectra, but it was a useful tool for quickly (< 10 min/sample) evaluating the $^{241}$Am + $^{238}$Pu:$^{240,239}$Pu activity ratio in individual particles. It was found that the $^{241}$Am + $^{238}$Pu:$^{240,239}$Pu activity ratio in individual particles ranged from 0.137 to 0.244 with a population (n=19) mean activity ratio of 0.196 ± 0.030. The mean activity ratio was in good agreement with the literature (11,19). None of the reported values matched the estimated activity ratio of 0.36 (1958-2009) (14).

Gamma spectroscopy was performed on 25 hot particles. Various photon peaks were selected for $^{241}$Am, $^{239}$Pu and $^{235}$U analyses. The $^{241}$Am:$^{239}$Pu activity ratios of the individual particles ranged from 0.15 - 0.25, with the population mean falling between 0.18-0.21. The expected $^{241}$Am:$^{239}$Pu activity ratio was 0.24, which was determined using the Bateman equations (15) and a 51 year decay period (1958-2009).

An alternative method of dating the age of the material based on the decay of $^{241}$Pu through the $^{237}$U decay chain was also developed. The photon peak at 204

keV contains signal from $^{239}$Pu, $^{241}$Am, and $^{235}$U. The photon with energy at 208 keV reflect $^{241}$Am and $^{237}$U. The yields of the gamma emissions were known for each of these isotopes and the $^{239}$Pu and $^{235}$U activities were determined independently from measurements taken at 129 keV and 185 keV photon energies respectively. The activity of both $^{241}$Am and $^{237}$U were determined from a series of linear equations. From the present-day activity of $^{237}$U, an initial $^{241}$Pu concentration was calculated, giving an effective date of last chemical separation. A separation date of 1955 ± 3 years was calculated from the weighted average of 12 samples using three different sets of peaks.

Substantial $^{235}$U was detected in some of the particles (185 keV), this was unexpected because the atomic ratio of $^{235}$U to $^{239}$Pu, due to the decay of $^{239}$Pu to $^{235}$U, should be 0.0014 for a 50 year decay period. These low atomic ratios of $^{235}$U should be nearly undetectable at the modeled $^{239}$Pu activity. Particles were observed with $^{235}$U:$^{239}$Pu atomic ratios ranging from 0.01 to 3.98, indicating that a $^{235}$U source must have been in the original weapon material.

Direct analysis of hot particles by alpha spectroscopy and gamma spectroscopy are useful tools. Alpha spectroscopy can rapidly define the $^{241}$Am + $^{238}$Pu:$^{239,240}$Pu activity ratios prior to sample dissolution and separation chemistry. Gamma spectroscopy provides $^{241}$Am:$^{239}$Pu activity ratios, $^{235}$U concentrations and also provides an alternative method for dating the materials through the $^{241}$Pu to $^{237}$U decay chain. The key to using these tools is the understanding that each particle is unique and that its characteristics may not be representative of the whole population. To successfully interpret the data from

both alpha spectroscopy and gamma spectroscopy a population of particles must be analyzed. A detailed description of these experiments is provided in Chapters 6 and 7.

### 1.4.4 Imaging of Hot Particles

Hot particle imaging experiments can be broken into two general groups based on the hardware required to run the experiments; scanning electron microscopy (SEM), and elemental mapping by x-ray fluorescence using a synchrotron. Three types of scanning electron microscopy experiments were performed; secondary electron imaging experiments (SEI), backscatter experiments (BES), and energy dispersive x-ray analysis (EDS/EDX).

Secondary electron imaging (SEI) uses the low energy electrons produced when the primary electron beam interacts with the sample surface. This produces secondary electrons and is used to study the morphology of the sample surface. Backscatter (BES) experiments make use of backscattered electrons from the primary electron beam. When the primary beam high energy electrons interact with material in the sample some are backscattered. The probability of back scatter increases with increasing Z, so high Z materials such as U, Pu, and Am will cause more backscatter events than low Z materials such as Si or Fe. Hot particles typically appear as bright spots when imaging a soil sample by BES, making them easy to identify. Energy dispersive x-ray spectroscopy (EDS/EDX) uses the primary electron beam to remove the inner shell electrons of the material being studied, resulting in the production of x-rays as outer shell electrons to fill the created holes. The energies of the x-rays

produced by this process are unique to specific elements and can be used as a qualitative tool to identify the material on the surface of a sample and as a semi quantitative tool to estimate elemental concentrations on the surface of the sample. The utility of SEI, BES and EDS is that a properly equipped SEM can perform all three experiments on a 3-D sample with a minimal sample preparation. The SEM data collected for several hot particles is presented in Chapter 5.

The synchrotron based x-ray fluorescence studies and elemental maps were conducted at Sector 10-IDB, MR-CAT at the Advanced Photon Source located at Argonne National Laboratory, Argonne, Illinois. These experiments require a sample with a flat, polished surface, and selection of the observed x-ray energies based on the scattering angle. This technique uses a monochromatic x-ray beam produced from a synchrotron light source to generate the x-ray fluorescence signal. This synchrotron-based system provides a constant, high flux and highly tunable x-ray beam to produce x-ray fluorescence. Because the conditions at a synchrotron can be optimized for specific elements and matrices, very precise and high resolution maps can be produced. The x-ray fluorescence data is presented in Chapter 5.

The primary result of the imaging studies was the observation that the elements that make up the hot particle matrix were not homogenously distributed in the particles. Images collected by SEM/EDS showed discrete U/Pu structures, and microprobe and synchrotron studies illustrated the separation of Am, U and Pu in some, but not all of the hot particles studied. These data are supported by

the variable $^{235}U$ concentrations and $^{241}Am$:$^{239}Pu$ activity ratios observed with gamma and alpha spectroscopy.

## 1.5 Source Term Characterization

The combined gamma, alpha, EDS and elemental mapping data provide information about the composition of the energetic materials, the configuration of the weapon and the conditions that formed the hot particles. An overview of the entire data set is presented in Chapter 8.

Data interpretation was approached from two viewpoints. The first is presented without reference to the historical narrative associated with the weapon and accident. This interpretation of the data represents a typical forensic scenario where the unknown material needs to be analyzed with little or no information available about its point of origin and limited information available about its recent past. The use of the Pu age data as a reference point is omitted from this interpretation. A detailed discussion of why the Pu isotopic data may not be useful or even misleading is presented in the second interpretation of the data set which includes historical information associated with the accident and the U.S. weapons production data from 1955-1960.

# CHAPTER 2

# SAMPLING AND CORING PROCESS

## 2.1 Introduction

The focus of this work was to characterize WGPu hot particles in terms of interactions with the near field environment and to develop novel techniques for nuclear forensic analysis. In the initial phase of this work, UNLV researchers traveled to the BOMARC accident site to collect soil cores and various samples that contained elevated activity levels due to the presence of hot particles. This chapter provides a brief overview of the site location and geologic conditions and the sampling techniques that were used to locate and collect samples of interest.

## 2.2 Site Location and Geological Significance

During the missile shelter fire, large volumes of water were used for fire suppression and it was recognized early on that water movement and human activity around the accident site resulted in conditions that aided the transport of Pu as both small pieces and as low levels of sub-granular particles (8). Contaminant mitigation in and around the burned missile shelter occurred soon after the accident, however, low levels of contamination were spread across the site. These areas of low contamination remained untouched until remediation efforts began in 2002. The samples that were collected by the UNLV team in 2007 were in an area of interest that had been determined by in-situ gamma field measurements but were otherwise undisturbed. It is important to note that the WGPu hot particles studied in this work persisted in the surrounding soil

environment for over forty years and therefore, understanding the site conditions in terms of geological characteristics is important for understanding hot particle interactions with the near field environment.

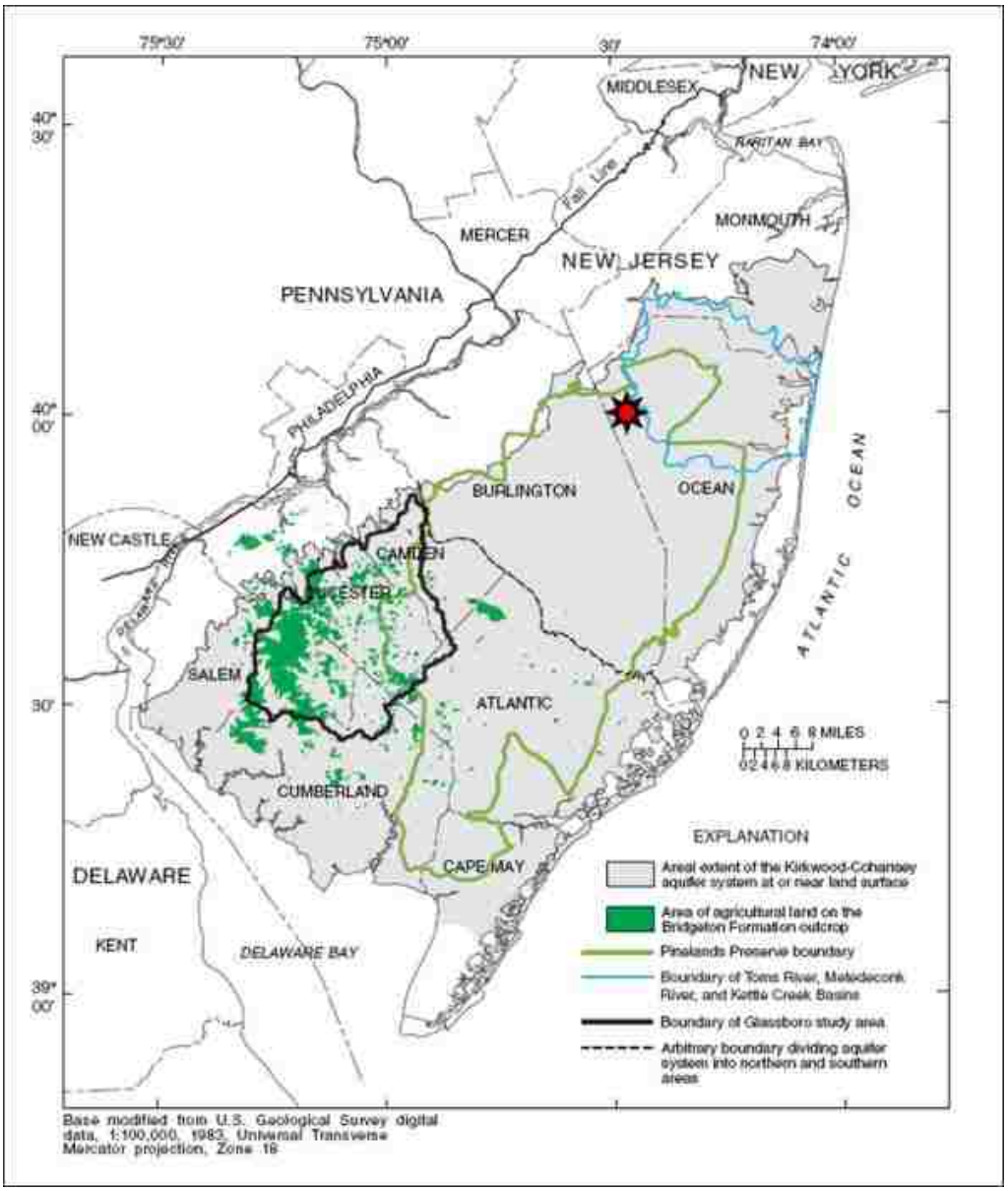


**Figure 5.** Map of New Jersey (20) with the BOMARC site highlighted by the red star.

The BOMARC accident site is located in the New Jersey Pine Barrens preserve (Figure 5). The soils in this area are composed of fine to coarse quartz sand and are slightly acidic (21). Daily temperatures vary from a normal minimum of -7°C in January to a normal maximum of 30°C in August, the state receives 1020-1270 mm of precipitation per year, and the frost line, or the depth at which ground water trapped in the soil may be frozen, is at 380-510 mm (22). The hot particles studied were found in the top 15 cm of soil, therefore it can be assumed that the particles were exposed to multiple freeze/thaw cycles.

## 2.3 Hot Particle Localization and Sampling Procedure

### 2.3.1 Soil Coring

Soil cores were collected from three areas on the site, outside the restroom facility, in a grassy field east of the firehouse and in a low activity area south of the eastern missile shelter block (Figure 3). High gamma activity areas had been located prior to the UNLV team arrival and were marked with flags by Cabrera Services. Using the flagged areas as a guide, a field instrument for detection of low-energy radiations (FIDLER, Ludlum 2221) and a 51 mm steel pipe flange were used to pinpoint the gamma emissions (59.5 keV, 35.9 % yield) produced by decay of $^{241}$Am (Figure 6).

The FIDLER was moved over the soil surface until the count rate was maximized (Step 1, Figure 6), then the pipe flange was placed between the FIDLER and soil surface (Step 2, Figure 6). The flange was then moved until the count rate on the FIDLER was maximized again. At this point the FIDLER could

be removed and a 51 mm diameter PVC pipe could be driven into the ground capturing the hot particle (Step 3, Figure 6 and Figure 7). This localization process was successful in 17 out of 19 attempts.

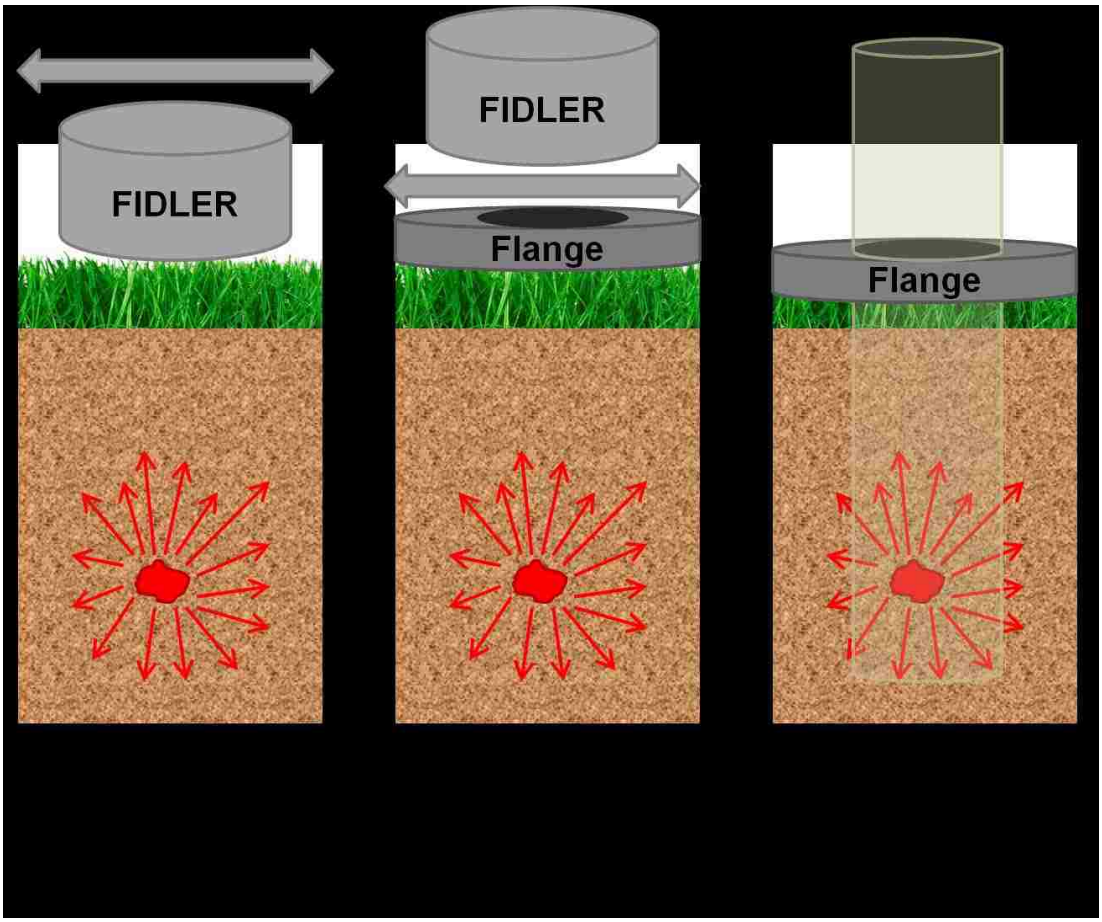


**Figure 6.** Procedure for capturing a hot particle using a FIDLER survey instrument and a pipe flange.

Position data was captured for each core using a handheld Garmin GPS (Rino 120) with 3 m accuracy. Once a core was pulled from the ground, a pressed-on steel cap was placed on the penetration end of the PVC tube to prevent the sample loss from the 'bottom' of the core. The outside of the tube

was wiped down and surveyed for residual activity using the FIDLER and a maximum count rate was determined to estimate the core activity for shipping purposes. The spatial integrity of the soil core inside the PVC pipe was secured for shipping purposes using a plastic cap, which was pressed down to the surface of the soil. The remaining head space between the cap and the end of the pipe was filled with a fast curing (< 1 hr) isocyanate catalyzed, closed cell polyurethane foam. The 'top' of the core was closed with a steel press-on cap (Figure 8).

**Figure 7**. Obtaining a core containing a WGPu hot particle. The 51 mm diameter PVC tube was manually driven into the ground to collect the core. The FIDLER used to locate the $^{241}$Am signal from the hot particle is located in the background.


**Figure 8.** Picture of a typical core. The white material on the left side is expanding foam used to fill headspace prior to shipping. A plastic cap (red) is used to isolate the soil from the foam. Steel caps were used to seal both ends of the core.

Core identification numbers and count rate data were marked on both the tube bodies and tube caps. A list of cores with locations, lengths and count rate data is given (Table 3). With the exception of cores Ref1 and Ref2, all of the cores collected are believed to contain at least one hot particle. Cores Ref1 and Ref2 were collected from the eastern side of the site in an area that was not impacted by the accident

**Table 3**. Location, length and count rate of BOMARC cores. The background count rate of the FIDLER was 4500±1000 cpm. Count rates are not background corrected.

| Core Number | Location Lat/Long | Description of Location | Length (cm) | Count Rate (CPM) |
|---|---|---|---|---|
| **1** | N 40$^{O}$ 02' 1.3" W 74$^{O}$ 26' 27.3" | Outside Restroom by Concrete Pad | 34 | 110,000 |
| **2** | N 40$^{O}$ 02' 1.2" W 74$^{O}$ 26' 27.4" | Outside Restroom by Concrete Pad | 37 | 85,500 |
| **3** | N 40$^{O}$ 02' 1.1" W 74$^{O}$ 26' 27.2" | Outside Restroom by Concrete Pad | 37 | 202,000 |
| **4** | N 40$^{O}$ 01' 50.9" W 74$^{O}$ 26' 26.0" | Grassy Field East of Firehouse | 17 | 215,000 |
| **5** | N 40$^{O}$ 01' 50.8" W 74$^{O}$ 26' 26.1" | Grassy Field East of Firehouse | 26 | 38,000 |
| **6** | N 40$^{O}$ 01' 50.8" W 74$^{O}$ 26' 25.8" | Grassy Field East of Firehouse | 15 | 23,000 |
| **7** | N 40$^{O}$ 01' 50.6" W 74$^{O}$ 26' 26.1" | Grassy Field East of Firehouse | 30 | 385,000 |
| **8** | N 40$^{O}$ 01' 50.6" W 74$^{O}$ 26' 25.9" | Grassy Field East of Firehouse | 28 | 52,000 |
| **9** | N 40$^{O}$ 01' 50.5" W 74$^{O}$ 26' 25.9" | Grassy Field East of Firehouse | 20 | 41,500 |
| **10** | N 40$^{O}$ 01' 50.3" W 74$^{O}$ 26' 25.9" | Grassy Field East of Firehouse | 14 | 149,000 |
| **11** | N 40$^{O}$ 01' 50.4" W 74$^{O}$ 26' 25.6" | Grassy Field East of Firehouse | 18 | 43,500 |
| **12** | N 40$^{O}$ 01' 51.2" W 74$^{O}$ 26' 25.5" | Grassy Field East of Firehouse | 33 | 28,000 |
| **13** | N 40$^{O}$ 01' 51.2" W 74$^{O}$ 26' 25.5" | Grassy Field East of Firehouse | 25 | 14,500 |
| **14** | N 40$^{O}$ 01' 51.2" W 74$^{O}$ 26' 25.5" | Grassy Field East of Firehouse | 26 | 470,000 |
| **23** | N 40$^{O}$ 01' 51.1" W 74$^{O}$ 26' 27.3" | Grassy Field East of Firehouse | 14 | 15,000 |
| **24** | N 40$^{O}$ 01' 51.1" W 74$^{O}$ 26' 25.8" | Grassy Field East of Firehouse | 12.5 | 38,000 |
| **25** | N 40$^{O}$ 01' 50.4" W 74$^{O}$ 26' 26.0" | Grassy Field East of Firehouse | 30 | 290,000 |
| **Ref 1** | N 40$^{O}$ 02' 1.3" W 74$^{O}$ 26' 25.2" | Field South of Eastern Shelters | 26 | 3,500 |
| **Ref 2** | N 40$^{O}$ 02' 1.1" W 74$^{O}$ 26' 24.7" | Field South of Eastern Shelters | 18 | 5,200 |

2.3.2 Bulk Sampling

In cases where a soil core could not be taken, soil was extracted using a small hand trowel and double bagged in PVC (6 mil) plastic bags. The outsides of the bags were wiped down with a towel, and the towel was surveyed with the FIDLER to check for contamination. The bags were then surveyed with the FIDLER to determine a maximum count rate and estimate an activity for shipping purposes. Nine samples ranging from 20 to 2500 g were collected (Table 4). Bulk sample 14a, was located adjacent to core sample 14. In this case, core 14 was extracted with elevated activity but some activity remained in the soil. An attempt was made to capture the residual activity in a second core but the footing from the firehouse slab made extraction of a second core impossible. In this case a bulk soil sample was extracted and labeled 14a. The description of location for sample 17 is currently unreadable but will be visible when the seal on this sample is broken. Data for Bulk Sample 20 is not currently available because this sample is sealed in the top of Core-13 and Core-13 has not been disassembled. A bulk sample (6a) consisting of 190 g of grass clippings from the field east of the firehouse was also collected. This sample was labeled 6a because the grass collected was located directly above core 6.

2.3.3 Particles Removed from Excavated Soil.

Eighteen small samples (< 50 $cm^3$ of soil per sample) each containing a hot particle were collected from soil excavated and being prepared for remediation by Cabrera Services. No site specific location data was available for these

samples. Detailed activity information for the individual hot particles extracted from the 18 small samples can be found in Chapters 6 and 7.

**Table 4**. Location, mass and count rate of bulk samples by FIDLER.

| Bulk Sample Number | Location Lat/Long | Description of Location | Mass (g) | Count Rate (CPM) |
|---|---|---|---|---|
| **14a** | N 40$^{O}$ 01' 51.2" W 74$^{O}$ 26' 25.5" | Firehouse next to concrete slab (East) | 1088 | 32,000 |
| **15** | N 40$^{O}$ 01' 51.2" W 74$^{O}$ 26' 25.5" | Firehouse next to concrete slab (East) | 21 | 12,000 |
| **16** | N 40$^{O}$ 01' 51.2" W 74$^{O}$ 26' 25.5" | Firehouse next to concrete slab (East) | 641 | 8,000 |
| **17** | N 40$^{O}$ 01' 51.2" W 74$^{O}$ 26' 25.5" | Not Available | 627 | 180,000 |
| **18** | N 40$^{O}$ 01' 51.2" W 74$^{O}$ 26' 25.5" | Firehouse next to concrete slab (East) | 1096 | 10,000 |
| **19** | N 40$^{O}$ 01' 51.2" W 74$^{O}$ 26' 25.5" | Firehouse next to concrete slab (East) | 622 | 14,000 |
| **20** | N 40$^{O}$ 01' 51.3" W 74$^{O}$ 26' 26.0" | Not Available | Not Available | 106,000 |
| **21** | N 40$^{O}$ 01' 50.8" W 74$^{O}$ 26' 26.0" | Moss From Firehouse Drainage Pit (East) | 1345 | 9,000 |
| **22** | N 40$^{O}$ 01' 50.8" W 74$^{O}$ 26' 26.0" | Soil from Firehouse Drainage Pit (East) | 2430 | 9,000 |

# CHAPTER 3

# LOCALIZATION AND ISOLATION OF HOT PARTICLES BY COMPUTED TOMOGRAPHY

## 3.1 Abstract

Fate and transport of hot particles in the environment are a particular concern for environmental modeling and forensic analysis. Traditionally, particles are located with field deployable radiometric equipment and the surrounding soil is collected and sub-sampled for bulk analysis. The inherent problem with this approach is the loss of spatial information associated with the particle and the near field environment. The objective of this work was to determine if particles could be identified in soil cores with minimal disruption using high resolution computed tomography (CT). Data was collected for intact soil cores (n = 5) from the BOMARC site and then each core was segmented into vertical slices. Particles (≥ 0.006 $mm^3$) were isolated from the relevant slices based on intensity mapping results. Other particles and debris of interest were also identified that would have been lost using traditional analytical methodologies.

## 3.2 Introduction

Traditionally, isolation of hot particles from kilograms of soil is performed using a sequential splitting technique (Figure 9) and successive radiometric analysis. This iterative process is time-consuming and limited to materials emitting radiation that can be externally detected. The introduction of real time digital imaging (17) has greatly reduced the time required to complete the last

steps of the separation process, but can only be applied to small sample masses (<1 mg). Sequential segmentation also destroys spatial information about the particle, which can be used to more fully understand fate and transport processes. As an example, particles have undergone both physical (shear or mechanical) and chemical degradation in simulated soil column studies (23,24). Smaller particles (or colloids) were formed under these conditions and were preferentially passing through the macropores of the soil column. This information is difficult to obtain in situ without knowing the exact location of the particle within the soil core and therefore, bulk characteristics are generally reported.

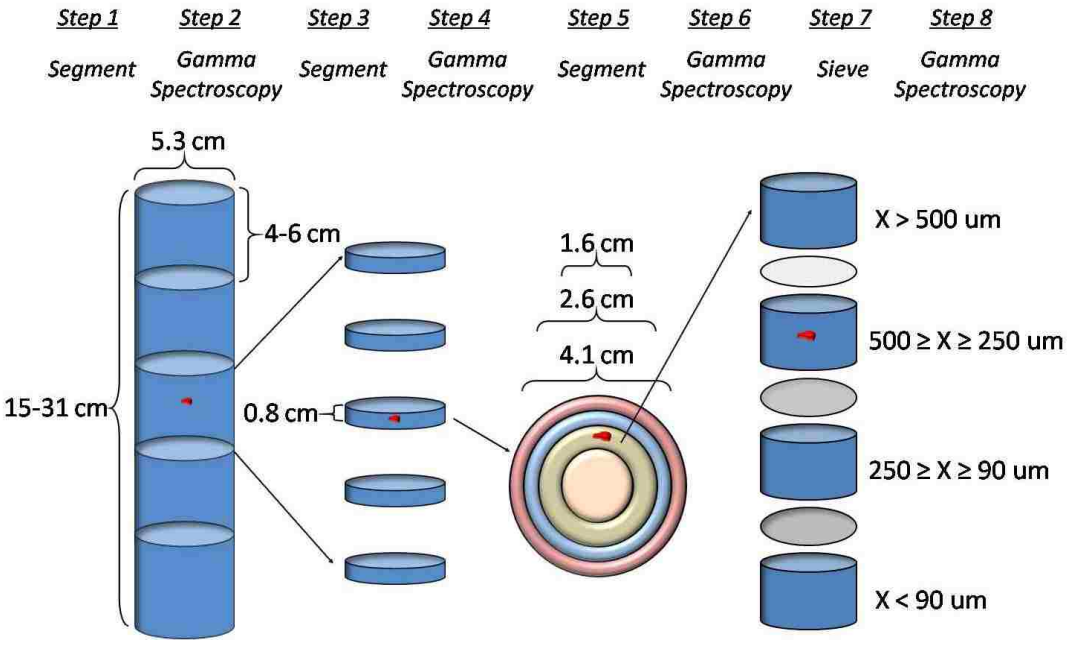


**Figure 9.** Traditional hot particle separation process.

An ideal method to locate hot particles in a soil core would be non-destructive, independent of decay processes and provide spatial information at the micron level without extensive handling of the core. Industrial CT, an x-ray based active imaging technique, meets these requirements and has been used in this work to image the BOMARC soil cores.

## 3.3 Computed Tomography Overview

Images collected by the CT scanner are produced by contrasting the x-ray attenuation characteristics, the atomic number *Z*, and density of the different materials present in the soil core. This concept can be quantified by Beer's Law (Equation 1), regarding the attenuation of a mono-energetic x-ray beam by a homogeneous material (15,25):

$$I = I_0 e^{-\mu t} \qquad \text{Equation 1}$$

where I and $I_0$ are the intensity of the attenuated and incident photon beams, respectively, μ is the linear attenuation coefficient in units of per cm, and t is the thickness of the material in cm. A compilation of materials expected to be present in the BOMARC cores is provided (Table 5). The data reported is based on a target thickness of 1 cm and incident x-ray energy of 210 keV. The material that constitutes the bulk of the sample mass, $SiO_2$, has a calculated $I/I_o$ value five orders of magnitude greater than the particle matrix, $PuO_2$. The relative extinction of the beam by the hot particle should be visible in a quartz sand matrix.

**Table 5.** Attenuation of a 210 keV x-ray beam by material that may be found in the BOMARC soil core.

| Material | Mass Attenuation Coefficient ($cm^{-1}$) (26) | Density ($g\ cm^{-3}$) | Fraction of the beam passing through the material ($I/I_o$) |
|---|---|---|---|
| **Air** | 0.1233 | 1.20E-03 | 0.999 |
| **PVC** | 0.1308 | 1.38 | 0.834 |
| **Fe (metal)** | 0.131 | 7.30 | 0.359 |
| **FeO(OH)** | 0.128 | 4.27 | 0.561 |
| **$Fe_2O_3$** | 0.128 | 5.26 | 0.491 |
| **$FeCO_3$** | 0.125 | 3.96 | 0.595 |
| **$SiO_2$** | 0.121 | 2.65 | 0.721 |
| **Pb (metal)** | 0.832 | 11.37 | 4.03E-5 |
| **Pu (metal)** | 1.170 | 19.82 | 0.000 |
| **$PuO_2$** | 1.040 | 11.46 | 3.0E-5 |
| **U (metal)** | 1.090 | 19.10 | 0.000 |
| **$UO_2$** | 0.973 | 10.63 | 1.76E-5 |
| **$U_3O_8$** | 0.941 | 8.30 | 2.48E-4 |

3.3.1 CT Instrumentation

A CT scanner consists of an x-ray source and a detector sitting in the same plane, arranged 180º from each other. The sample is placed between the beam and the detector and a series of intensity measurements are acquired while the source and detector assembly are rotated along the central axis of the sample (25). Industrial scanners in use today typically employ a fan-type x-ray beam and a bank of detectors in a planar or arc configuration (Figure 10). The fan-type x-ray beam and multi-detector array allow for faster data acquisition because a full view can be captured without having to move the x-ray source and detector assembly.

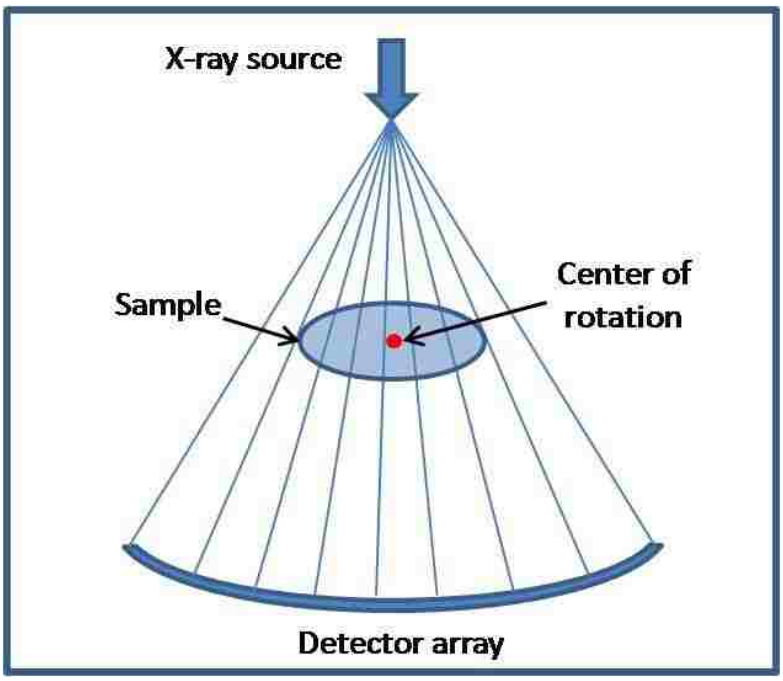


**Figure 10.** Configuration of a 3rd generation scanner using a fan type x-ray beam and arc shaped detector array

3.3.2 Image Processing

As the x-ray source and detector assembly is rotated around the sample, a series of projections are acquired. Each projection is converted to a function that is filtered in the spatial domain (convolution) or in the frequency domain (Fourier Transform) to reduce noise (27). The filtered signal or back-projections are then integrated across the steps producing a 2-D image that constitutes a single slice of the sample.

Slices are collected along the vertical axis of the soil core and must be registered and normalized to be processed into a 3-D data set after collection. Registration and normalization are critical image processing steps. Registration corrects for poor sample placement and any uncontrolled movement in the

sample as it is being scanned while normalization corrects for drift in the average x-ray energy and intensity between scans. In this work, the wall of the PVC tube that contained the soil core was used as the normalizing signal.

After registration and normalization have been completed, artifact removal may be performed on the image. Artifacts are undesirable components that can be introduced during the image acquisition or signal processing steps. For example, beam hardening may result in the edges of a sample appearing brighter than the center (25). This intensity shift is caused by the selective attenuation of low energy x-rays by the sample, but is undesirable for distinguishing different materials. Details on the treatment of artifacts are available in the literature (27).

The final image processing step is the conversion of the data set to a file format suitable for data analysis. A lossless TIFF format is preferable to JPEG because the data will not be subject to potential errors introduced by a data compression algorithm. From a practical point of view the smaller size of the JPEG files (kilobytes) makes them easier to work with and analyze using a desktop PC than the TIFF files (megabytes).

### 3.3.3 Dimensional Elements

Images are parceled into dimensional elements, pixels and voxels. A pixel represents a single point in an array that makes up a 2-D image (27). A voxel or volume element (28) is the same as a pixel except a third dimension, usually depth, is associated with the point. For the CT imaging experiments, a single slice outside the context of the core, is treated as a 1024 x 1024 pixel image.

That same slice, when taken within the context of neighboring slices, has a defined spatial representation, 1024 x 1024 x 1 voxels or elements. Voxels help to determine volume and spatial information for objects that occupy multiple slices. Both picture elements are used for particle localization.

## 3.4 Method Summary

### 3.4.1 Core Preparation

Five cores collected from the BOMARC site were selected for CT analysis. Specific details about the coring process are provided elsewhere (Chapter 2). A description of each core is provided (Table 6). Prior to imagining, the location of the maximum activity in each core was estimated (± 10 mm) using a shielded, collimated NaI detector. The cores were prepared for shipping by solvent welding polyvinyl chloride (PVC) plugs to the ends of the cores. Each core was vacuum sealed to provide secondary containment (Figure 11).

**Table 6.** Description of cores analyzed.

| Core ID | Total Length (cm) | Soil Length (cm) | Volume ($cm^3$) | Location of Activity Maximum (cm below surface) | Total Activity kBq (uCi) |
|---|---|---|---|---|---|
| **Core 6** | 18.4 | 15.3 | 312 | 3.1 | 72 (2.0) |
| **Core 9** | 23.5 | 21.4 | 437 | 1.3 | 144 (3.9) |
| **Core 11** | 20.3 | 17.5 | 357 | 1.0 | 216 (5.9) |
| **Core 14** | 28.9 | 25.4 | 518 | 18.4 | 361 (9.8) |
| **Core 24** | 17.2 | 12.0 | 245 | 4.6 | 96.2 (2.6) |


**Figure 11.** Soil core containment for shipping purposes.

3.4.2 Image Acquisition

Soil cores were imaged at the University of Texas High Resolution X-ray CT (UTCT) facility in Austin, Texas using an ultra-high resolution system (ACTIS, Bio-Imaging Research Inc). The acquisition parameters are provided (Table 7). Cores exceeding 20 cm in total length were imaged in two sections because they exceeded the length of travel along the vertical axis of the instrument. Image registration, normalization and artifact removal were performed by UTCT. An image of the cross sectional area of a core is provided (Figure 12). Dark objects correspond to materials that do not attenuate x-rays. Light or white objects correspond to materials that highly attenuated the x-rays and are referred to as blobs (27).

**Table 7.** Additional imaging parameters

| UTCT Image Acquisition Parameters | |
|---|---|
| **Beam Energy (keV)** | 210 |
| **Operational Current (mA)** | 0.15 |
| **Views per rotation** | 1000 |
| **Slice Thickness (µm)** | 74.3 |
| **Pixel Size (µm)** | 63.5 x 63.5 |
| **Pixels per Field of View** | 1024 x 1024 |
| **Voxel Volume ($mm^3$)** | 3.0E-4 |
| **Total Slices (per core)** | 1300-2000 |
| **Scan time (hrs)** | 1.5 – 2 hours |
| **Image Type** | JPEG (8 bit)<br>TIFF (16 bit) |
| **Gray Scale Range** | 256 |
| **File Size (MB)** | 25 - 45 |
| **Process and Archiving Time (hrs)** | 3.25 – 4.5 |

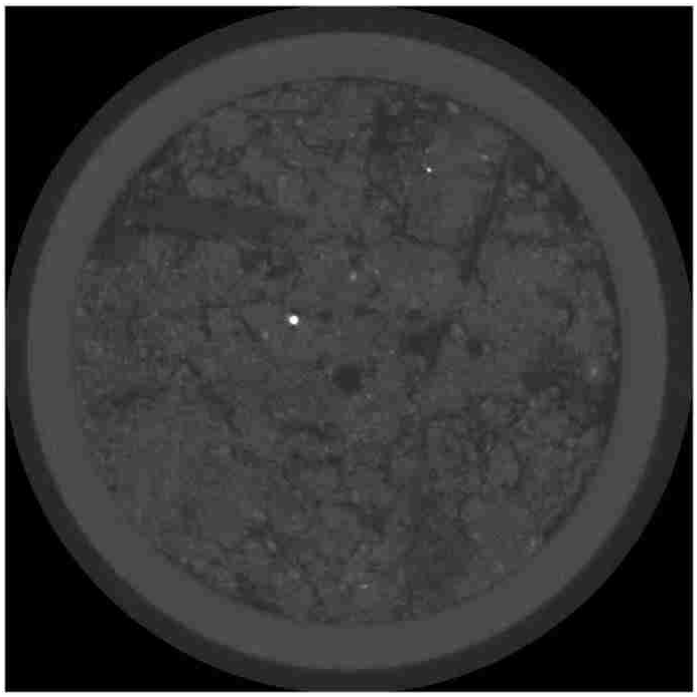

**Figure 12.** Digital image of the cross sectional area of a BOMARC soil core.

### 3.4.3 Image Analysis

All image analysis was done using Matlab Version 7.4 (29) and BLOB3D (30) utilizing IDL Virtual Machine (31). Analysis of the core images is a four-step process:

- Binary conversion of the gray scale image
- Assembly of a 3-D array of binary images
- Compression of the descriptive data (position, size and maximum intensity)
- Data compilation for blob population analysis

Image conversion is accomplished by setting a threshold intensity value. If the intensity value of a given pixel is less than the threshold value, it is assigned a 0. Pixel values equivalent to or greater than the threshold are assigned a 1. For core analysis, the threshold value was 0.152; therefore pixel intensity values < 39 (256 X 0.152) were set to 0. The result is a binary image that only highlights blobs (Figure 13).

After conversion, the binary images are stacked into a 3-D array, representing only the blobs in the core. Blob connectivity is checked using a 26 voxel inspection process (Figure 14). This process combines blobs from multiple slices that represent a single 3-D object in the core. The position, dimensions and maximum intensity for each blob is calculated and compiled into a separate data set for further analysis.

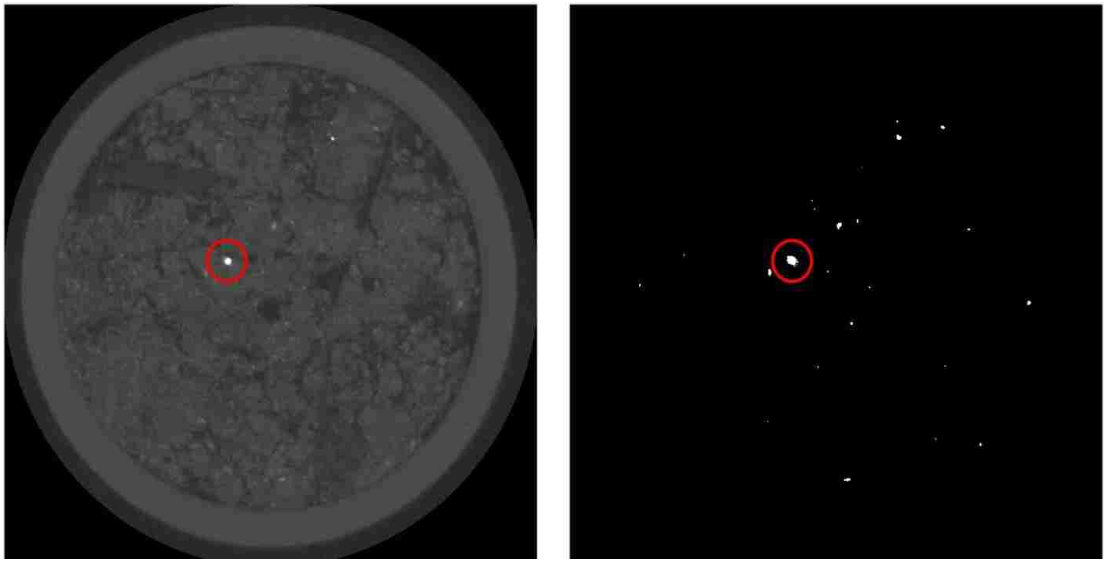

**Figure 13**. Conversion of a 256 grayscale image (left) to a binary image (right). The red circle denotes the same feature in both images.

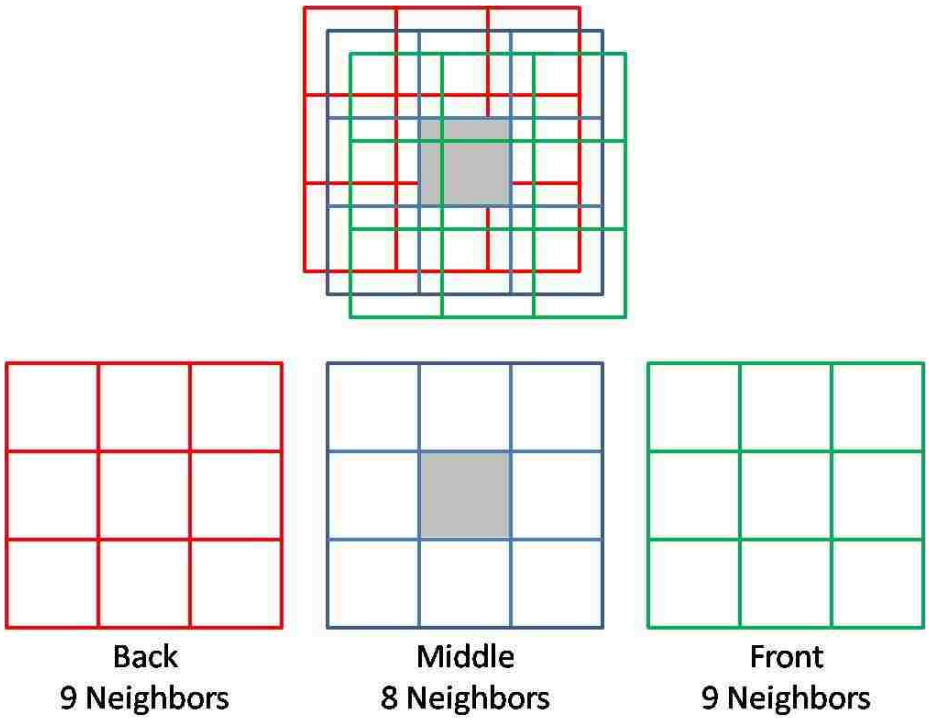


**Figure 14.** Nearest neighbors, the 26 voxels surrounding the center (gray) pixel

### 3.4.4 Blob Population Analysis

The spatial data for each blob was complied and the blob population was plotted in terms of intensity, volume and position. The highest intensity blobs were identified and were selected as objects of interest (potential hot particles) in the core. The cores were then disassembled (Chapter 4) to retrieve the objects of interest for further analysis (Chapter 6). Cores were portioned vertically into 3.5 mm slices to retain spatial information, and particles were identified by gamma detection. The position data obtained during core disassembly was compared to the blob population analysis to correlate hot particle location and blob intensity.

## 3.5 Results and Discussion

### 3.5.1 Blob Populations

An example of the processed core data is provided (Figure 15). The normalized blob intensity was plotted in terms of slice number and the corresponding vertical core depth. The blobs that are located above the core surface are experimental artifacts that are attributed to initial sample preparation.

The top 1 – 2 cm of the core had a high organic content that may have been unevenly compressed during the coring process. As an example, a surface slope offset of 1 mm, would affect 13 slices in the imaging process. The expanding foam that was used to keep the core intact during shipping may have also incorporated foreign debris during the curing process (Figure 11).

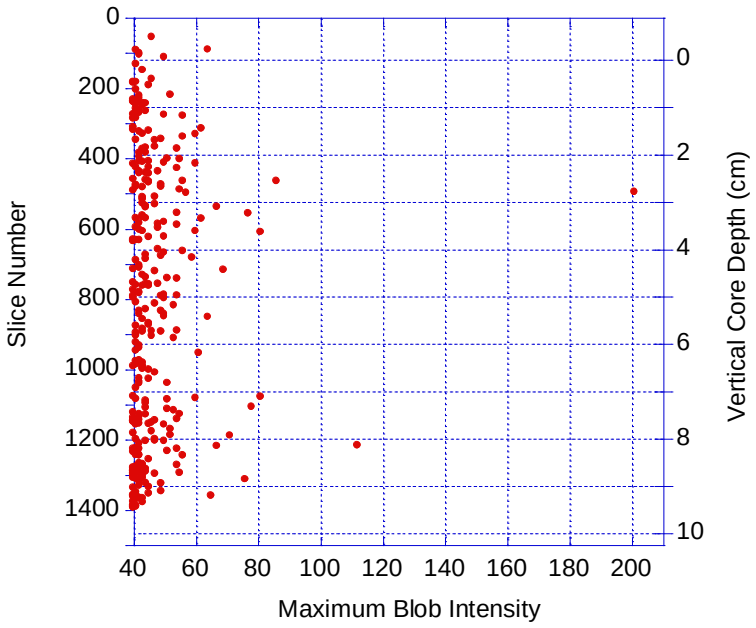


**Figure 15.** Vertical blob distribution by maximum intensity for a soil core.

The majority of the blob population had intensity values below 60 for all five cores (Figure 16). Hot particles were expected to have high intensity values based on attenuation characteristics (Table 5) therefore, blobs with values > 70 were selected as potential objects of interest. This corresponded to approximately 1 - 2% of the total blob population.

Additionally, the intensity should be highly localized for hot particles, i.e. the blob volume should be small (> 1 $mm^3$) based on the isotopic information (Table 1) and the initial activity estimation (Table 6). Volumes of the selected blobs were calculated based on a minimum voxel intensity of 39, which is twice the average voxel intensity (Figure 17). All nearby pixels with intensity >39 are associated with the brightest pixel to define the cross sectional area of the particle.

The bulk of the selected blobs were < 1 $mm^3$ based on the selection criteria (Figure 18) with two exceptions. The largest blobs were later identified as a piece of leaded glass, material commonly used in vacuum tubes (32) and Pb shot. Blob population analysis provided likely candidates for hot particles based on intensity and volume thresholds that could be localized in the core by slice number and core depth.

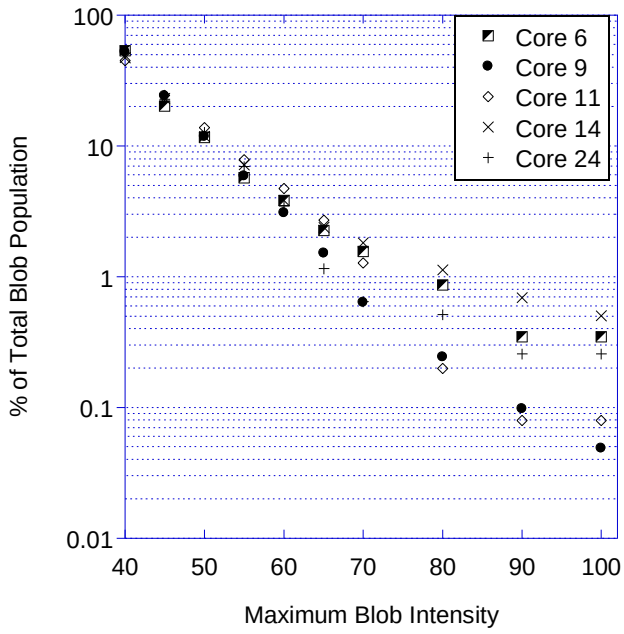


**Figure 16.** Population distribution as a function of blob intensity for n = 5 soil cores.

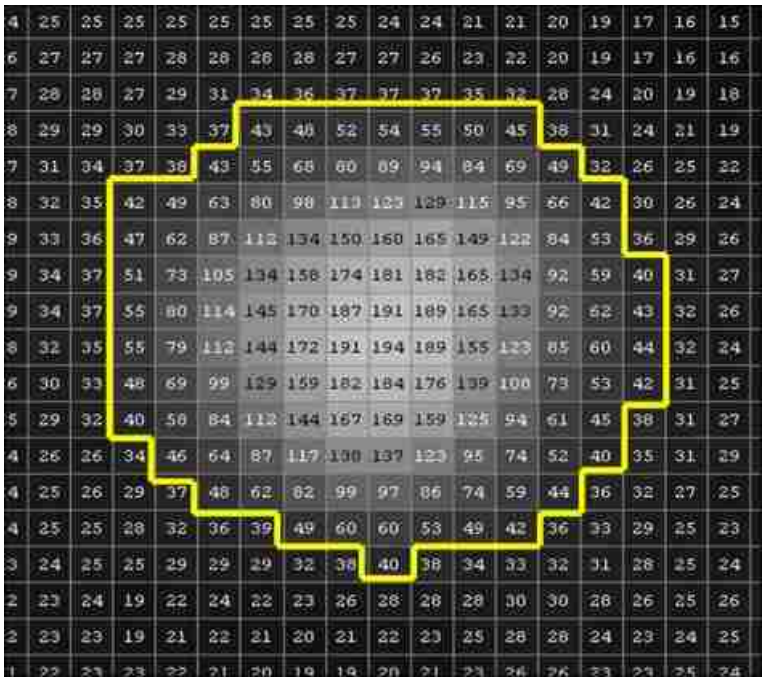

**Figure 17.** Area selected to determine blob volume and cross-sectional area in 2-D.

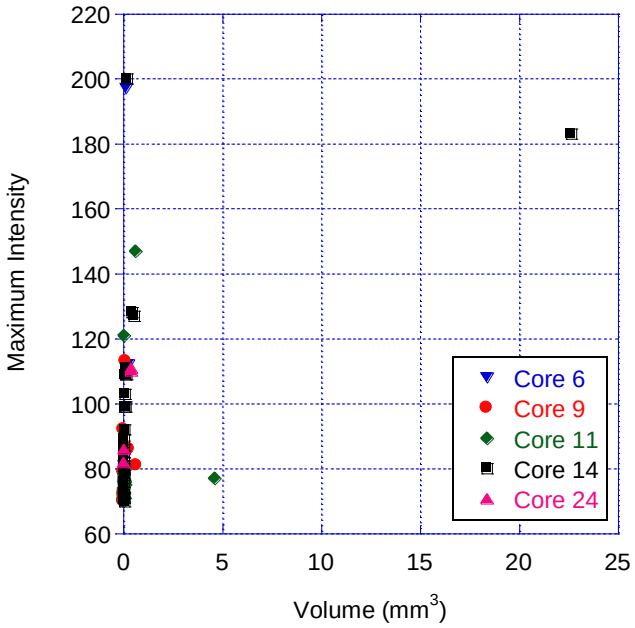


**Figure 18.** Maximum intensity versus volume for the selected blob population.

### 3.5.2 Particle Analysis

Particles were localized by the spatial and morphological characteristics in the gray scale images during core disassembly. Each slice of interest was scanned with a NaI detector to isolate particles with elevated activity. Other non-radioactive particles of interest were also isolated for additional analyses. The intensity and location information of hot particles that were removed from each core is provided (Table 8). Many of the particles that were initially identified based on the selected threshold values could not be located. This was attributed to the small particle size, similar morphology to the soil granules and the elevated background in the glovebox that was used for core disassembly. Several non-radioactive spherical white beads were identified (Figure 19). Energy dispersive spectroscopy (EDS) indicated that the bead matrix was primarily Ti and Ce, which would explain the high intensity values (Table 9).

**Table 8.** Hot particles identified during core disassembly.

| Core ID | Intensity | Slice Number | Depth (cm) | Particle Location (cm) | HP Activity (kBq) |
|---|---|---|---|---|---|
| **6** | 201 | 497 | 2.8 | 2.4 - 2.8 | 41 |
| **9** | 89 | 463 | 0.7 | 0.7 – 1.0 | 60 |
| **11** | 122 | 221 | 1.2 | 1.0 – 1.4 | 80 |
| **14** | 199 | 2779 | 18 | 18-18.4 | 551 |
| **24** | 86 | 1250 | 3.7 | 3.8 – 4.1 | 64 |

The hot particles exhibited a larger maximum intensity to volume ratio than the other material found in the cores (Figure 20). An empirically fit line placed

through the hot particle data set outlines the region where hot particles would be expected to fall based on this preliminary data set. The expected hot particle limit of detection (LOD) for the current experimental set up is an intensity of 82 and a volume of 0.006 $mm^3$. Some of the particles that could not be located share similar intensity and volume characteristics with the Ce/Ti beads that were recovered. It is possible that these particles were beads that were not identified.

**Table 9.** Non-radioactive Ce/Ti beads removed from the soil cores.

| ID | Depth (cm) | Estimated Volume ($mm^3$) | Intensity |
|---|---|---|---|
| **Core-24-1** | 7.7 | 0.404 | 110 |
| **Core-14-1** | 1.3 | 0.519 | 127 |
| **Core-14-2** | 1.6 | 0.429 | 128 |
| **Core-14-3** | 3.1 | 0.019 | 82 |
| **Core-14-4** | 4.0 | 0.029 | 89 |
| **Core-14-5** | 4.1 | 0.021 | 85 |
| **Core-14-6** | 5.8 | 0.059 | 99 |
| **Core-14-7** | 6.0 | 0.060 | 92 |

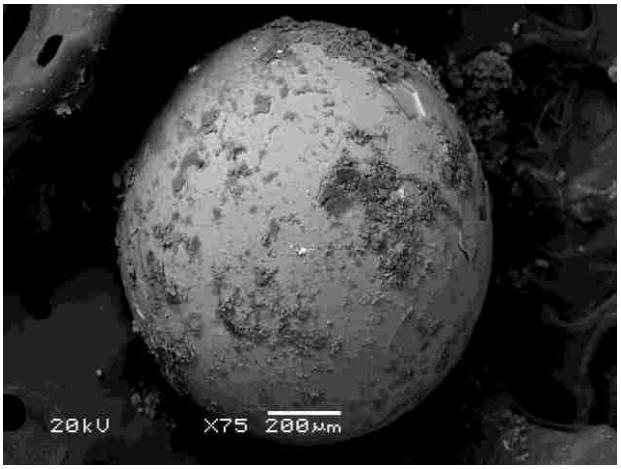


**Figure 19.** Image of an intact bead removed from Core 14, obtained by secondary electron microscopy (SEM).

The intensity values for particles with volumes under 0.1 $mm^3$ are provided on an expanded scale (Figure 21). Many of the unknown particles have intensity values < 82. These could be representative of hot particles that fall below the LOD. Evidence of discrete micro-particles was determined by gamma and alpha analysis on the vertical distribution of $^{241}Am$ in the soils (Chapter 4) after the primary hot particles were removed. Physical isolation of these micro-particles may be possible using technique similar to those discussed in the literature (17).

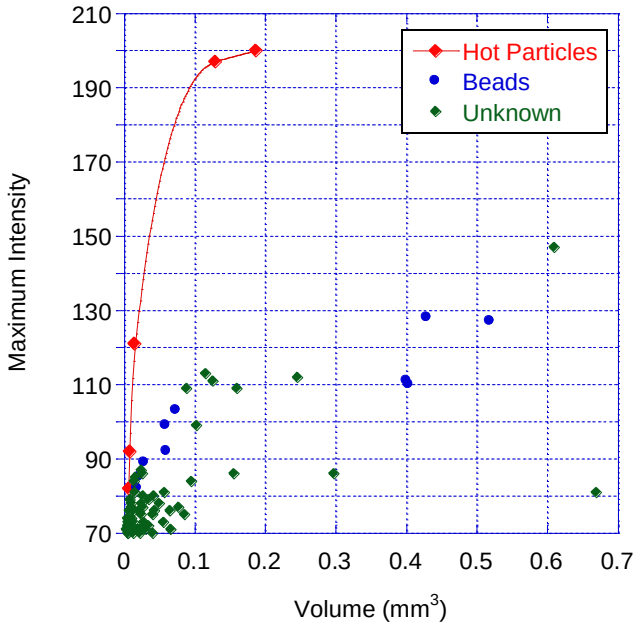


**Figure 20.** Blob intensity versus volume based on particle identification.

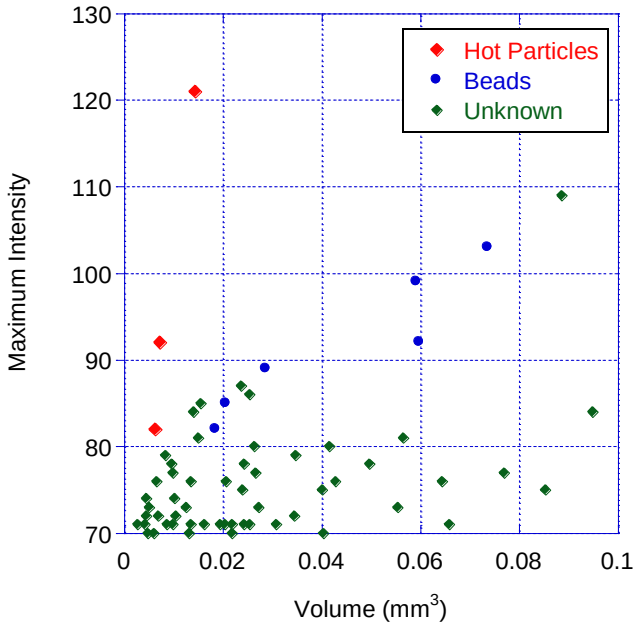


**Figure 21.** Maximum intensity distribution for particles with volumes < 0.1 $mm^3$.

## 3.6 Conclusions

High resolution CT has been successfully applied to the precision localization of hot particles in a soil core and is non-destructive. Analysis by CT provides additional advantages for locating particles of interest that are high Z, but low in specific activity. As an example, a $UO_2$ particle that is < 1 $mm^3$, may not have sufficient counts for gamma detection, but can be identified using the current method. Hot particle analysis indicated that U was a separate component in close contact with the Pu. A few particles isolated from other soil samples were predominantly U. From attenuation values provided (Table 5), $UO_2$ particles would have lower intensity values than $PuO_2$ particles. It is possible that some of the unknowns (Figure 21) with high intensity values and small volumes were U based particles. Standards or reference materials that contain actinides must be

developed to determine if U and Pu particles can be differentiated based on intensity distributions. This would establish better background and threshold estimations for blob population analysis.

The combination of CT and radiometric localization provide additional information about particle transport in the soil column. Particle driven physicochemical processes can be confirmed *in situ* once actinide particles can be localized with greater certainty. The blob population profiles (Figure 15) are similar to the activity distribution plots (Chapter 4), but more data will be required for direct comparison.

In addition to locating hot particles, other non-radioactive objects were also isolated. The Ce/Ti beads and leaded glass could provide additional forensic evidence about the source term of the material or activities that were conducted on the site. These materials may have been missed using classical methods. Another utility that was not specifically discussed in this work is the opportunity to study microbe populations surrounding the hot particles. Microbial influence on actinide speciation and transport in the environment is of great concern (33) for remediation and repository management. Microbiology studies are currently being conducted in collaboration with the Dessert Research Institute (Las Vegas, Nevada) on BOMARC soil cores.

# CHAPTER 4

# $^{241}$AM DISTRIBUTION IN SOILS COLLECTED FROM THE BOMARC SITE

## 4.1 Abstract

The vertical distribution of $^{241}$Am in five soil cores (5 cm diameter by 15-30 cm long), containing mixed actinide oxide particles ($10^5$-$10^6$ Bq/particle) have been characterized using high purity Ge (HPGE) gamma spectroscopy and alpha/beta gas flow proportional counting. Although more than 95% of the activity present in each core is contained within a single particle, a residual amount of Am and Pu remains in the soil. This residual material provides a window into the mechanisms driving the dispersion of Am and Pu in the soil. For these experiments, each core was segmented into a series of 3.5 mm thick slices. The hot particles were manually removed from the relevant slice and the residual Am concentration in each slice was determined. Plutonium was identified in many of these slices but concentrations could not be determined. The results of this work indicate that the vertical distribution patterns of residual Am and Pu are highly core dependent and near field dispersion is being driven by a combination of sorption/desorption and particle transport processes.

## 4.2 Introduction

The presence of Pu particles in the environment is neither rare nor unique, but common and geographically well distributed (2,3,4,6). Each site where Pu particles have been dispersed provides an opportunity to study the interaction of Pu and its daughter products within a variety of environments and conditions. As

more is learned about the behavior of Pu, the level of understanding and ability to model the behavior of this material is improved.

The soil cores from the BOMARC site provided an opportunity to study the distribution of material shed by Pu particles in an acidic fine quartz sand soil (21). The particles were located in the top 15 cm of the soil column and were affected by the seasonal freeze thaw cycles and the meter of precipitation this region experiences annually (22). This combination of environmental factors indicates that the particles have been subject to mechanical as well as chemical degradation processes during their residence in the soil.

The distribution of material shed from the particles as a function of depth was determined by gamma spectroscopy using photons associated with the decay of $^{241}$Am. The cores that were selected for non-destructive computed tomography (CT) imaging (Chapter 3) were disassembled as 3.5 mm slices post imaging to aid in removal of the Pu particle contained in each core. Unlike $^{241}$Am and Pu concentrations previously reported in surface samples (19), the results of these experiments quantify the $^{241}$Am concentrations both above and below the region from which the hot particles were isolated.

## 4.3 Gamma Analysis of Pu Distributions Using $^{241}$Am as a Surrogate

In this work, $^{241}$Am was used as a surrogate for the distribution of Pu in the soil core, because it is directly incorporated into the Pu matrix through the decay of the short-lived $^{241}$Pu. This assumes that the surface area relative to the volume of the particle was small and that Pu and Am would be transported

together through the soil. It should be noted that in materials where the matrix surface area relative to the total volume of the sample is large, Pu and Am may separate due to differences in their chemical behavior resulting in different transport properties. Because the exact physico-chemical composition of the hot particle was unknown at the time, it was important to be able to verify that the $^{241}$Am and Pu were both present in the particle and soil sample. This was accomplished by high resolution gamma spectroscopy analysis. Though the WGPu particle matrix is dominated by $^{239}$Pu in both mass and activity, it yields few unique photons when it decays (Table 10), making direct detection of low concentrations difficult by gamma spectroscopy. However, the 59.5 keV photon associated with the decay of $^{241}$Am can be easily detected with the HPGE system.

**Table 10**. Energy and yields of some of the photons associated with the decay of $^{239}$Pu and $^{241}$Am (16).

| Radionuclide | Energy (keV) | Yield (%) | BEGE Detector Efficiency (%) | Relative Peak Area |
|---|---|---|---|---|
| **$^{241}$Am** | 59.5409 | 35.9 | 25 | 1 |
| **$^{239}$Pu** | 38.661 | 0.01044 | 20 | 9.3E-4 |
| **$^{239}$Pu** | 51.624 | 0.02722 | 25 | 3.03E-3 |

The relative isotopic composition of the hot particle matrix as a function of time can be determined using the information provided (Table 11) and the Bateman equations (15). Assuming a 50-year decay period the $^{241}$Am:$^{239}$Pu activity ratio is estimated to be 0.24. Using high resolution gamma spectroscopy

for analysis and assigning the peak area due to the $^{241}$Am photon at 59.5 keV a value of 1, then the two most intense $^{239}$Pu peaks would have areas of 9.3E-4 and 3.3E-3 of the $^{241}$Am peak after correcting for radiative yield and changes in the detector efficiency (Table 10). These signals are three orders of magnitude smaller than the $^{241}$Am signal observed at 59.5 keV. The 51.6 keV $^{239}$Pu photon sits on the Compton continuum generated by the interaction of the $^{241}$Am photon with the BEGE detector (Figure 22) making quantification of the Pu signal difficult.

**Table 11.** Pu isotopic information for the BOMARC weapon estimated by LANL with a 1957/1958 separation date.

| Isotope | Mass Fraction 1958 | Half Life ($t_{1/2}$, yrs) | Primary Decay Mode | Activity Fraction 1958 |
|---|---|---|---|---|
| **$^{238}$Pu** | 0.000099 | 87.7 | Alpha | 0.0295 |
| **$^{239}$Pu** | 0.937 | 24,110 | Alpha | 0.1010 |
| **$^{240}$Pu** | 0.056 | 65,61 | Alpha | 0.0221 |
| **$^{241}$Pu** | 0.0047 | 14.290 | Beta | 0.8475 |
| **$^{242}$Pu** | Negligible | 3.75 E5 | Alpha | Negligible |
| Mass fraction data and separation date are from (14), half life and decay modes are taken from (16). | | | | |

Even though quantification of the $^{239}$Pu concentration in the soil may not be possible, the presence of the Pu in the soil can be verified by the 38.7 and 51.6 keV $^{239}$Pu photon peaks (Figure 22). This would indicate that both Am and Pu are present in the sample, The lack of peaks at 38.7 and 51.6 keV cannot be used to exclude the presence of Pu, as the activity concentration may be below detection limit of gamma spectroscopy for a 24 hour counting period, which for

the utilized system is 16 ± 5 Bq $^{239}$Pu. For the samples where $^{239}$Pu cannot be detected total dissolution of the soil followed by chemical separation of Am, U and Pu from the dissolved soil matrix must be conducted. Once chemically separated into U, Am and Pu aliquots, the concentration of each of these elements can be determined by liquid scintillation counting. If isotopic ratios are desired the separated aliquots can be measured by alpha or mass spectroscopy.

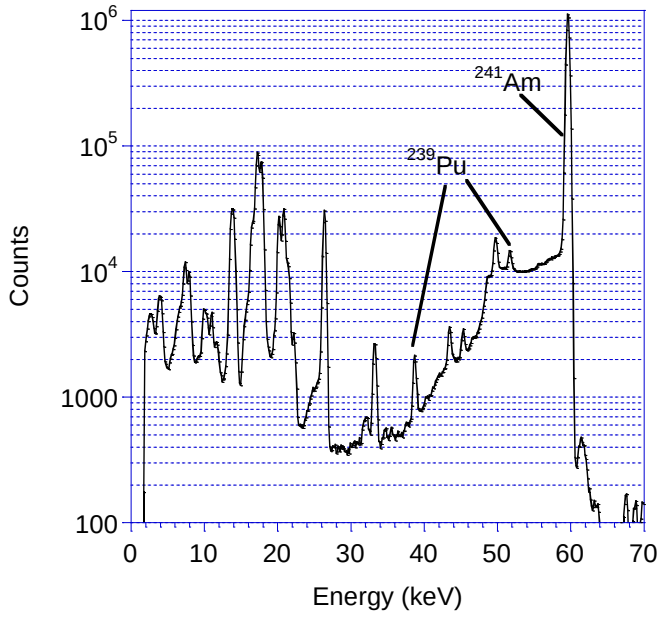


**Figure 22.** Low energy spectrum of $^{241}$Am and $^{239}$Pu in soil

## 4.4 Hot Particle Extraction from Soil Cores

The cores studied were 13-26 cm in length and 5 cm in diameter. The location of the hot particle in each core had been established by CT mapping studies (Chapter 3), and the hot particles were extracted from the soil prior to starting these experiments. The extracted particles consisted of a mixture of

WGPu, $^{241}$Am and $^{235}$U and ranged in activity from 5 to 66 kBq of $^{241}$Am as determined by gamma spectroscopy (Chapter 6). The results of these experiments are summarized (Table 12). The range of $^{235}$U relative to $^{239}$Pu over the hot particle population was broad, indicating that the weapon contained both Pu and U components (Chapters 6 and 8).

**Table 12.** Activity ratios of selected WGPu hot particles isolated from the soil cores. Analysis is based on gamma spectroscopy analysis.

| Radionuclide | Average Activity Ratio |
|---|---|
| **$^{235}$U: $^{239}$Pu** | 5.56E-5 ± 1.58E-4 (0 to 6.62E-4) |
| **$^{241}$Am: $^{239}$Pu** | 0.22 ± 0.026 (0.19 to 0.288) |
| **Sample Population** | n = 18 |

## 4.5 Method Summary

### 4.5.1 Soil Core Disassembly

Each core was disassembled along its vertical axis, using a bottle jack jig (Figure 23) that displaced 3.5 ± 0.1 mm of soil with each pump. After the soil was raised with the bottle jack, the material extending past the lip of the PVC pipe was scraped into a second jig that fit over the PVC pipe and then placed in a sample cup. It was found that the sample volumes were kept relatively constant using this technique. The few large rocks and twigs transecting multiple slices were kept with the last slice that contained them. To minimize the impact of cross contamination between samples the soil retaining jig, upper section of the

core and the core lip were wiped down using a clean, damp kimwipe between each 3.5 mm soil slice.

The volume of soil occupying each 3.5 mm slice was placed in a 120 mL plastic container (Figure 24). Larger rocks and twigs were removed from the sample and were checked using a hand held alpha detector (Ludlum 43-93 probe and Ludlum 2224-1 scaler/ratemeter) but none of these materials were found to contain elevated activity. Each sample was dried at 20 °C in a hood for at least 24 hours and then the total mass was determined. The average mass across all 5 cores was 10.2 ± 2.6 g per 3.5 mm soil slice volume. The large standard deviation in the average sample mass was due to a change in soil characteristics between soil slices within a given core, such as shifts from organic layers to sandy layers and from samples that contained large rocks or numerous pebbles, thereby decreasing the volume of soil in the slice.

**Figure 23.** The core disassembly unit. The bottle jack jig (left) displaced 3.5 mm of soil per pump. The soil retaining jig (right) captured the soil volume in each 3.5 mm slice.

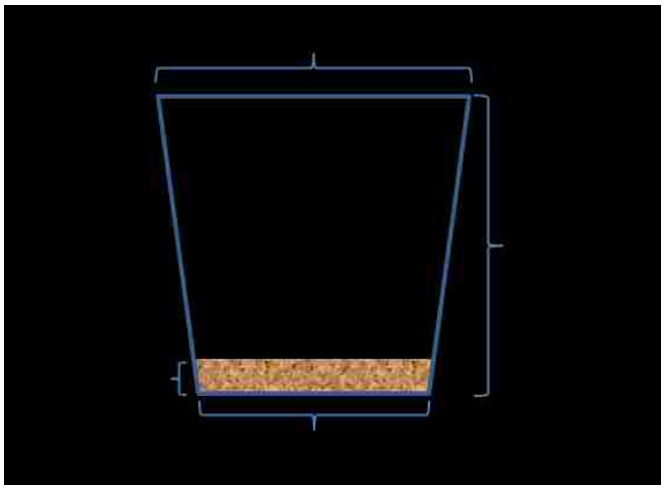

**Figure 24.** Illustration of sample container used for the soil volume from each 3.5 mm slice.

4.5.2 Gamma Analysis

A Canberra BE3830 BEGE detector with a 63.5 mm diameter by 30 mm thick planar detector with a carbon composite window was used for all gamma measurements. All samples (3.5 mm soil slice volume) were counted for 24 hours with dead times below 0.5 %. The $^{241}$Am and $^{239}$Pu in the soil was quantified or identified through gamma decay (Table 10).

Although the hot particles were removed from each slice, the physical distribution of the residual $^{241}$Am within each sample was not known. Therefore the efficiency of the HPGE detector had to be determined for the sample geometry used in this work. If the $^{241}$Am distribution was from particles with activity concentrations below the detection limit of the hand held device used to isolate the hot particles from the soil slices, then the relative position of the particle within the sample container will greatly affect the counting efficiency. To

illustrate this effect, an $^{241}$Am point source standard was used to determine the geometrical dependence on the counting efficiency of the detector. As the source was moved away from the center of the detector face, the efficiency dropped as much as 27% at the lateral edge of the sample container (Figure 25).

All counting results were subject to this 27% relative uncertainty because the distribution of $^{241}$Am within each sample was not known. Because the samples were relatively thin (3.5 mm), and the point source was centered in a 6 mm thick epoxy button, the 0.5 mm difference in vertical displacement was not considered in these efficiency calculations.

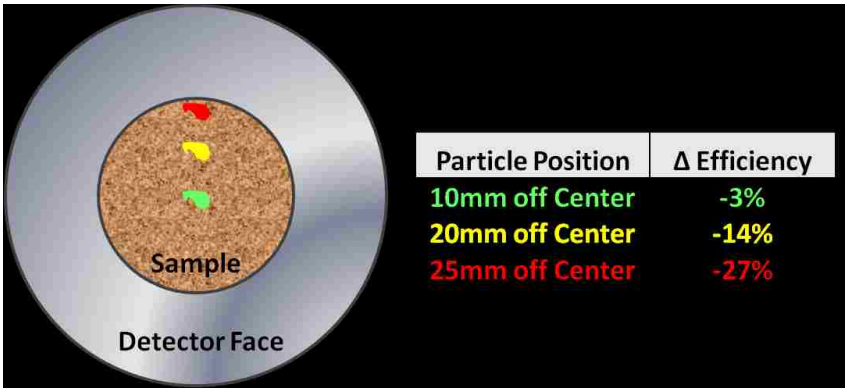


**Figure 25.** The influence of a point source (or particle) position on detector efficiency.

4.5.3 Soil Particle Size Distribution Analysis

After each 3.5 mm slice was analyzed by HPGE gamma spectroscopy, several slices were selected for particle size distribution analysis as a function of core depth. For each core, every fifth sample, 1.75 cm vertical displacement was

passed through a series of five sieves; 1250 μm, 500 μm, 250 μm, 125 μm, 63 μm.

4.5.4 Particle versus Diffuse Activity Analysis

To determine if micro hot particles were present in these samples, a second set of experiments was devised. A soil sample that had been measured by gamma spectroscopy and had the large objects removed (> 1250 μm) was parsed into 8-10 sub samples of equal volume. Each sample was placed on a 3.81 cm (1.5 in) planchet and then counted on a Berthold α/β gas proportional counter for 1000 minutes. The sub samples were then stirred and returned to the same chamber and counted again for 1000 minutes. This process was repeated for multiple trials, effectively changing the surface of each sub sample for each trial. If micro hot particles were diffusely distributed, a continuous level of activity should be observed for each sub sample across all the trials. If particles or point sources were present, the count rate would change between trials, as the surface area of each sub sample was exchanged, covering or uncovering the particles. The alpha and beta plateaus for the α/β counter were configured using $^{90}Sr/^{90}Y$ and $^{232}Th$ calibration sources, respectively.

## 4. 6 Results and Discussion

4.6.1 Core Activity Distribution

Activity distributions of $^{241}Am$ as a function of depth for 5 cores were determined. The location and activity of the hot particles in each core are summarized (Table 13). Most of the hot particles were isolated in the top 5 cm of

soil and contained ≤ 10 KBq of $^{241}$Am activity. Core 14 was the exception, where the hot particle was more than 17 cm below the surface of the core and had six times the activity of the other particles.

**Table 13.** Summary of the cores that were analyzed by HPGE gamma spectroscopy.

| Core ID | [1]Total Residual Activity (Bq) | Core Length (cm) | [2]Hot Particle Activity (kBq) | [3]Hot Particle Location (cm) |
|---|---|---|---|---|
| **6** | 78.8 ± 21.3 | 15 | 5.1 | 2.8 |
| **9** | 126.9 ± 34.3 | 20 | 7.0 | 1 |
| **11** | 21.1 ± 5.7 | 18 | 10 | 1.4 |
| **14** | 2,641 ± 713 | 26 | 66 | 17.2 |
| **24** | 44.0 ± 11.9 | 12 | 7.6 | 4.3 |

[1]Residual core activity after removal of the hot particle.
[2]The hot particle was removed from the surrounding soil prior to analysis and characterized separately (Chapters 6 and 7). Activity is based on the 59.5 keV photon associated with the $^{241}$Am decay.
[3]Hot particle location is relative to the surface (or top) of the core.

Data for each core is presented in the horizontal bar graphs below. The x axis represents the activity concentration in Bq/g (log scale) of $^{241}$Am for soil particles smaller than 1250 μm, the y axis represents the depth in cm below the surface of the soil from which each sample was originally isolated. The depth profile for Core 6 (Figure 26) indicated that the bulk of the residual $^{241}$Am remained in the soil layer that had contained the hot particle (2.8 cm vertical displacement) and the layers of soil immediately below the hot particle. The presence of $^{239}$Pu was qualitatively confirmed for these same samples using the photon peaks previously mentioned (Section 4.5.2). As soil depth increased, the average $^{241}$Am concentration was approximately 0.01 Bq/g of soil. At depths

greater than 11 cm below the surface the $^{241}$Am concentration began to decrease.

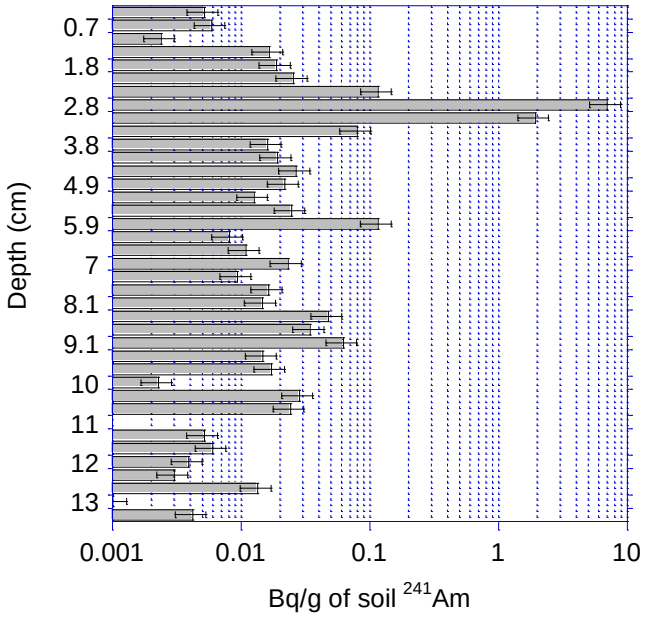


**Figure 26.** Core 6 $^{241}$Am depth profile.

The depth profile for Core 9 (Figure 27) also indicated an area of high residual $^{241}$Am activity associated with the layer of soil that contained the hot particle. The residual activity declined as the soil depth increased. Unlike Core 6, additional activity spikes occurred further down the core at 13, 15 and 18 cm. The $^{239}$Pu photon peak was observed with the $^{241}$Am activity spikes at 13 cm and 15 cm as well as in the layer (1 cm) from which the hot particle was removed. It is possible that these spikes were from additional hot particles below the detection limits of both the CT imaging analysis (particle volume < 0 .006 mm$^3$) and hand-held devices.

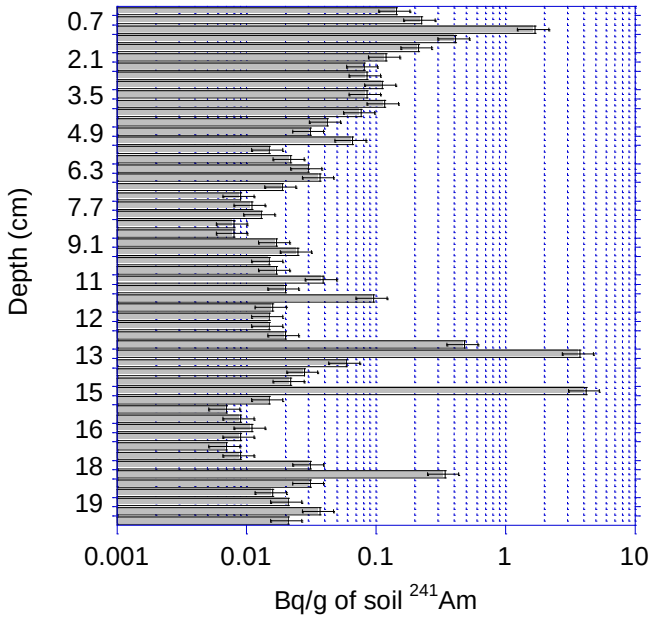


**Figure 27.** Core 9 $^{241}$Am depth profile.

The depth profile for Core 11 (Figure 28) shows areas of high residual $^{241}$Am concentrations found in the soil layer that contained the hot particle as well as in the soil layers immediately above the hot particle. Below the layer that contained the hot particle the residual $^{241}$Am concentration declined with increasing depth and then stabilizes at approximately 0.01 Bq/ g of soil. Small activity spikes were observed at 9.1 and 10.1 cm. Below 11 cm the $^{241}$Am concentration decreased again. The $^{239}$Pu photons were observed with the spike occurring at 1.4 cm (slice where hot particle was removed) but not in the lower slices with spiked $^{241}$Am activity.

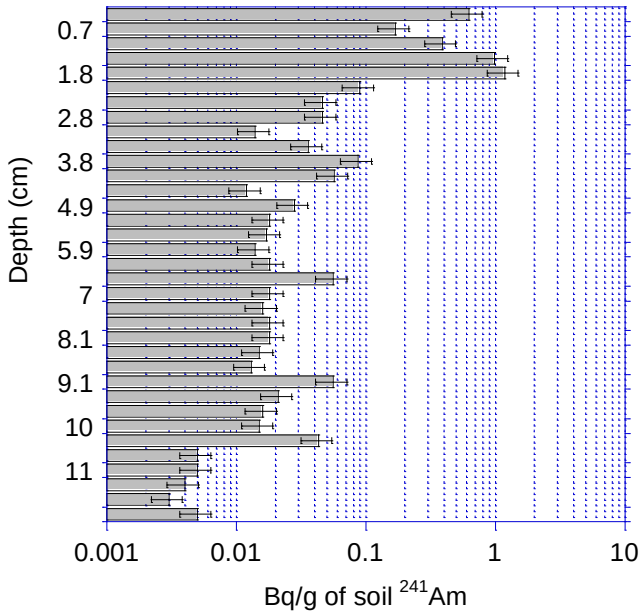


**Figure 28.** Core 11 $^{241}$Am depth profile.

Considerable $^{241}$Am was found in the top soil layers of Core 14 (Figure 29). The highest activity spike occurred at 2.1 cm below the core surface. The region of elevated $^{241}$Am concentration extended down to 5.6 cm and $^{239}$Pu was also observed in these samples. At depths below 6 cm the $^{241}$Am concentration decreased. However several $^{241}$Am concentration spikes were observed between 9 and 13 cm. The $^{239}$Pu photons were observed for all of these activity spikes.

For core 14 the hot particle was removed from a slice that was located 17.2 cm below the surface. As with the other cores, the soil in the slice that contained the hot particle as well as several underlying soil slices contained high residual $^{241}$Am concentrations. The $^{239}$Pu photon peaks were also observed in these

slices. Another activity spike was detected at 23 cm below the surface that contained both $^{241}$Am and $^{239}$Pu.

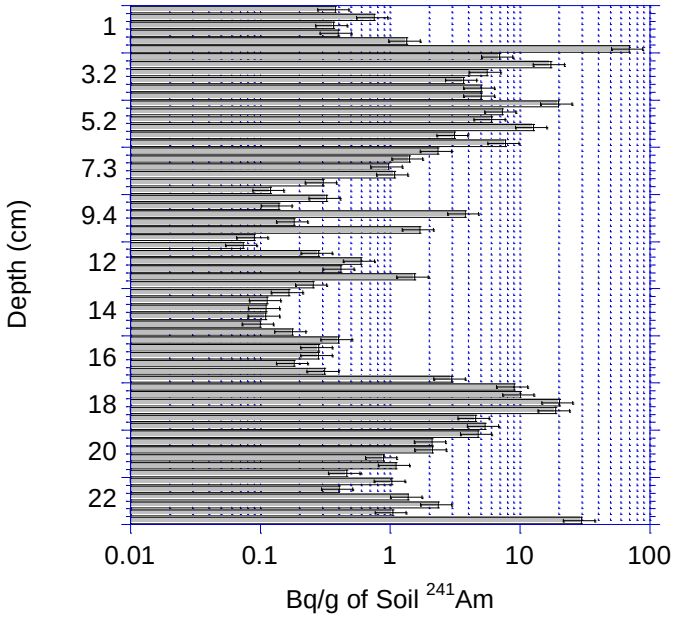


**Figure 29.** Core 14 $^{241}$Am depth profile.

It is likely that the hot particle identified 17.2 cm below the surface was found by accident, and that the signal identified during field sampling originated in the top 6 cm of the core. This assumption is based on the composition of the soil and Beer's Law (18,34):

$$I = I_0 e^{-\mu t} \qquad \text{Equation 2}$$

where I and $I_0$ are the intensity of the attenuated and incident photon beams, respectively, μ is the linear attenuation coefficient in units of inverse cm, and t is the thickness of the material in cm. If it is assumed for simplicity that the core consisted of mainly $SiO_2$ where μ =0.601 $cm^{-1}$ (26,35) and that the primary photon measured by the field instrumentation was the 59.5 keV from the decay

of $^{241}$Am, then approximately 2.7% of the photons emitted 6 cm below the soil surface will penetrate the surface, while only. 0.0036% of the photons escape at 17 cm below the surface. The integrated activity in the top 6 cm of the core was measured to be 1,347 ± 364 Bq ($^{241}$Am) while the hot particle removed from 17.2 cm below the surface of the core had an evaluated activity of 93,402 ± 4670 Bq ($^{241}$Am).

The depth profile of Core 24 (Figure 30) was similar to Core 6. The $^{241}$Am concentration was elevated at the top of the core, above the layer that contained the hot particle. At 5.5 cm below the surface the $^{241}$Am concentration diminished. Several activity spikes were observed at 6.7, 7.4 and 11.6 cm. The presence of $^{239}$Pu was verified at 6.7 and 11.6 cm.

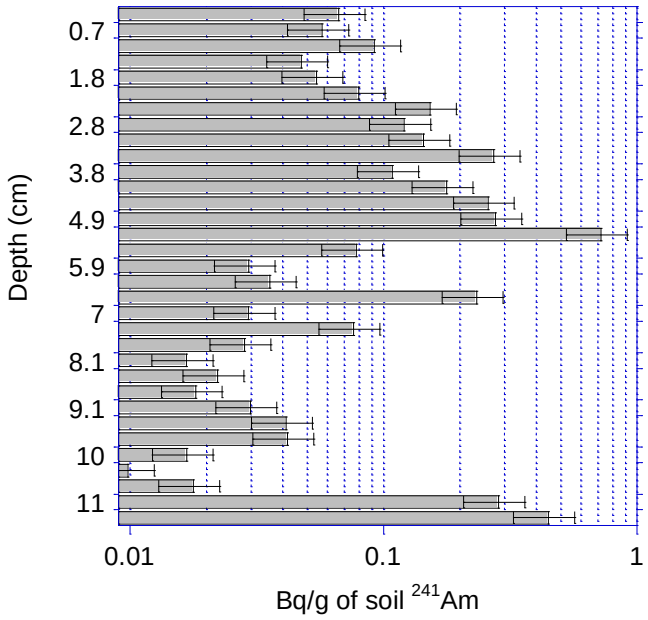


**Figure 30**. Core 24 $^{241}$Am depth profile.

Once activity distributions for each core were collected the total residual $^{241}$Am activity was calculated by integrating each slice (Table 13). This data was combined with those for the isolated hot particles (Chapter 6) to determine if there was a correlation between residual activity and hot particle activity (Figure 31). No trend relating hot particle activity to the amount of residual activity present in the soil was observed. This indicates that hot particle activity is not a major factor driving the $^{241}$Am distribution in the soil.

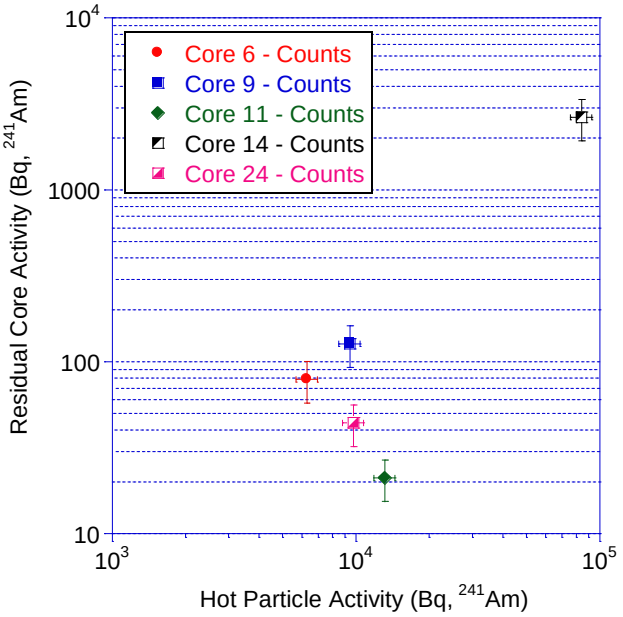


**Figure 31**. The total $^{241}$Am activity found in each core compared to the $^{241}$Am activity of the hot particle removed from the corresponding core.

These depth profile data sets exhibited 6 trends.

(1) There was an elevated concentration of $^{241}$Am in the soil column directly above the hot particles.

(2) The $^{241}$Am concentration decreased in the soil immediately below the hot particle.

(3) There were regions where the $^{241}$Am concentration was stable or remained constant with depth.

(4) No clear relationship existed between hot particle activity and the residual activity found in each core.

(5) There were discrete $^{241}$Am concentration spikes not associated with the isolated hot particle.

(6) The presence of $^{239}$Pu was identified with most of the $^{241}$Am concentration spikes.

The first three trends are indicative of surface area driven processes such as sorption and desorption, an exchange of material between the soil and the particle. With the assumption the hot particle was initially deposited on the surface of the soil, $^{241}$Am found above the particle would indicate that particle movement down into the soil column released $^{241}$Am. This released $^{241}$Am sorbed to the soil and is now fixed in place or moving very slowly under the site conditions. The continuous decrease of $^{241}$Am concentrations to a fixed minimum concentration below the hot particle indicates that $^{241}$Am is shed from the particle at a rate greater than that at which the surrounding soil can sorb it. Sorption and desorption processes are expected to produce $^{241}$Am concentration gradients (36,37) based on the composition of the soil, the metal ion species present in the soil column, and the interaction of the metal ion species with the various exchange sites. Of greater interest is the discrete $^{241}$Am concentration spikes

found in the core samples, suggesting a particle-like behavior in the soil column. This is supported in the subsequent studies conducted by gross alpha/beta measurements that demonstrate spatial dependence of $^{241}$Am in small soil samples (Section 4.6.3).

4.6.2 Soil Particle Size Distribution

After gamma analysis, several slices from each core were sieved to determine the soil particle size distribution as a function of core depth. A typical particle size distribution is provided (Figure 32). The x axis is the percent of the sample by mass (% by mass) that was characterized by the indicated sieve, and the y axis refers to the depth or distance below the surface of the soil from which the sample originated. A significant portion of the core particles were greater than 250 µm in diameter. The size of the hot particles removed from the cores (which were identified by CT) ranged between 150 to 1000 µm along their longest axis.

4.6.3 Particle versus Diffuse Activity Analysis

Gross alpha/beta analysis was performed on four soil samples taken from two cores ranging in activity from 0.008 to 6.05 Bq/g $^{241}$Am (Table 14). These soil samples were split into 9 or 10 sub-samples of equal size prior to counting. The data from the gas proportional counter are reported as a gross alpha count rate in counts per minute (cpm) and cannot be directly reconciled with the activity concentrations determined by gamma spectroscopy. In this case the data from the gas proportional counter was exclusively used for trend analysis. The background signal was 0.07±0.12 cpm alpha and was not subtracted from the

reported results. Examples of the trend analysis for each the sample is provided (Figure 33 through Figure 36).

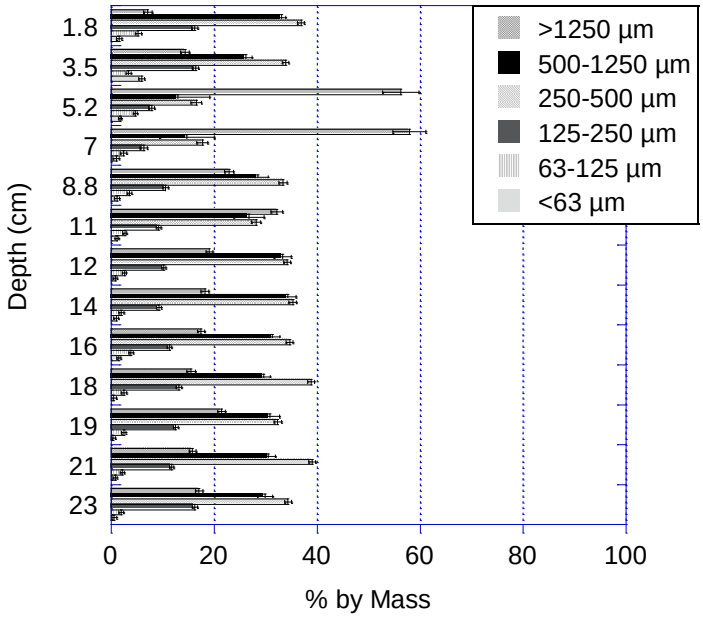


**Figure 32.** Particle size distribution as a function of depth for soil core (Core-14).

**Table 14**. Summary of the core samples chosen for gross alpha/beta analysis.

| Core ID | Core 14 | Core 6 | Core 6 | Core 6 |
|---|---|---|---|---|
| **Slice Number** | 15 | 16 | 17 | 18 |
| **Sample Location (cm)** | 5.25 | 5.6 | 5.9 | 6.3 |
| **Activity of Sample (Bq/g soil, $^{241}$Am)** | 6.05 | 0.025 | 0.116 | 0.008 |
| **Slice Mass (g)** | 6.4 | 6.8 | 9.4 | 6.2 |
| **Sample Splitting** | 10 | 9 | 9 | 9 |
| **Split Sample Mass (g)** | 0.6 | 0.8 | 1.0 | 0.6 |
| **Number of Trials** | 11 | 5 | 5 | 6 |

All four experiments exhibit the same trends. Some sub samples had consistent count rates that were independent of experimental trials, indicating a

homogenous or diffuse activity distribution. Other sub samples had variations in the count rate for separate trials, indicating localized regions of high surface-area-specific activity (particles or disseminated activity). This data supports the observations made during gamma spectroscopy analysis, and suggests that transport is driven by both particle migration and sorption/desorption processes. Imaging analysis using Secondary Electron Microscopy (SEM) of the hot particles that were isolated from the cores discussed in this work provided physical evidence of the presence of micro hot particles sorbed to a soil substrate (Chapter 5).

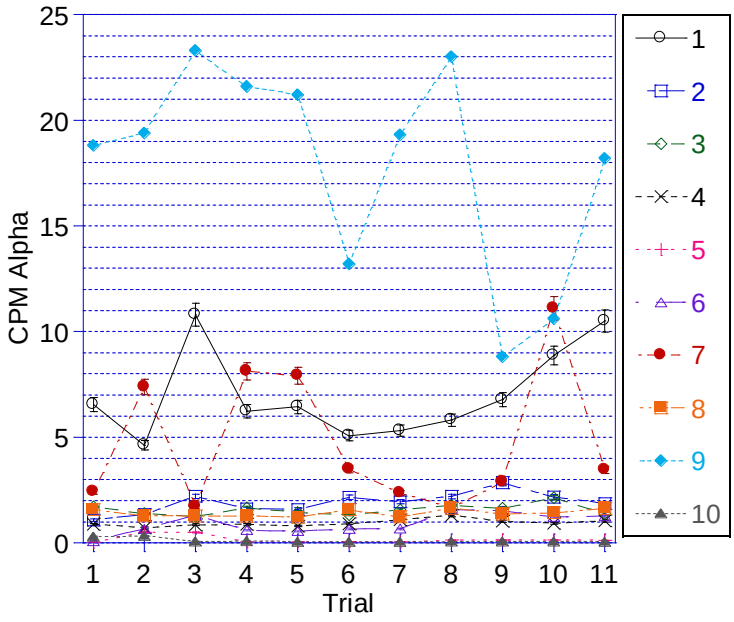


**Figure 33**. Core 14 – Slice 15, gross alpha count rates for 10 sub samples and 11 trials. Background signal for these experiments was 0.07±0.12 cpm α and was not subtracted from the reported results.

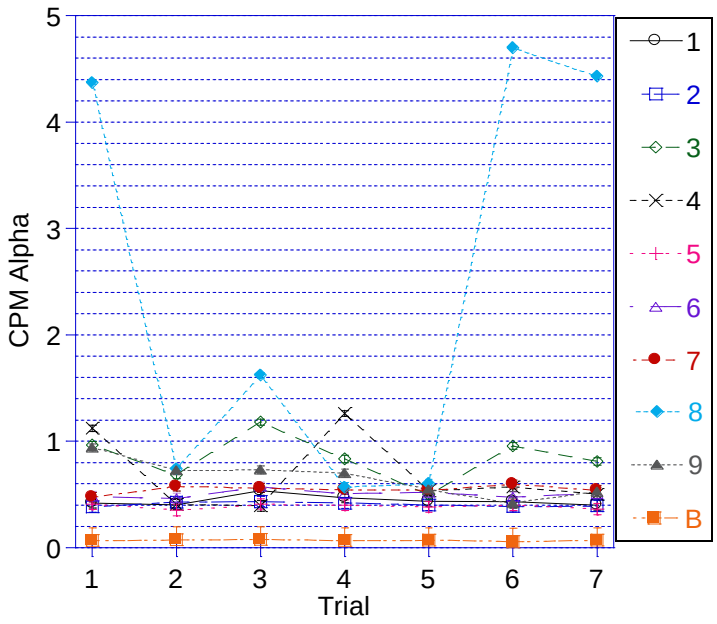


**Figure 34**. Core 6 – Slice 16, gross alpha count rates for 9 sub samples and 7 trials. Error bars may be covered by the data point markers. The background count rate is identified by 'B'.

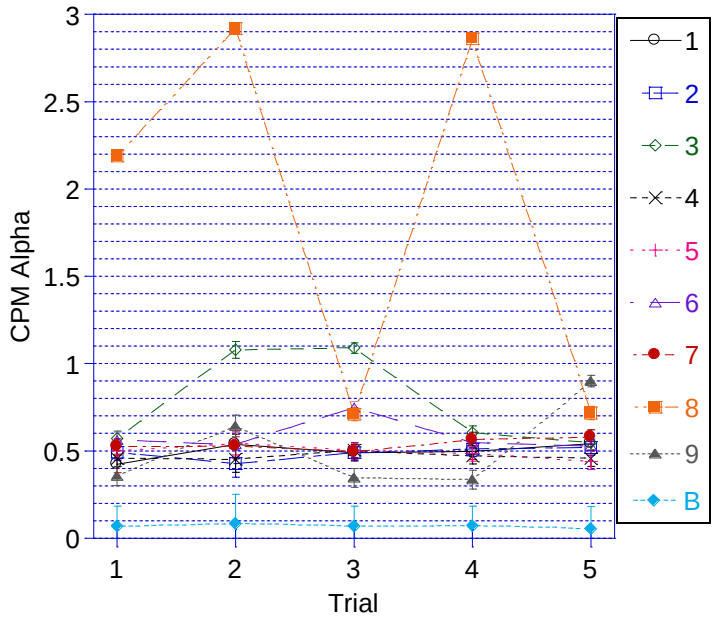


**Figure 35**. Core 6 – Slice 17, gross alpha count rates for 9 sub samples and 5 trials. Error bars may be covered by the data point markers. The background count rate is identified by 'B'.

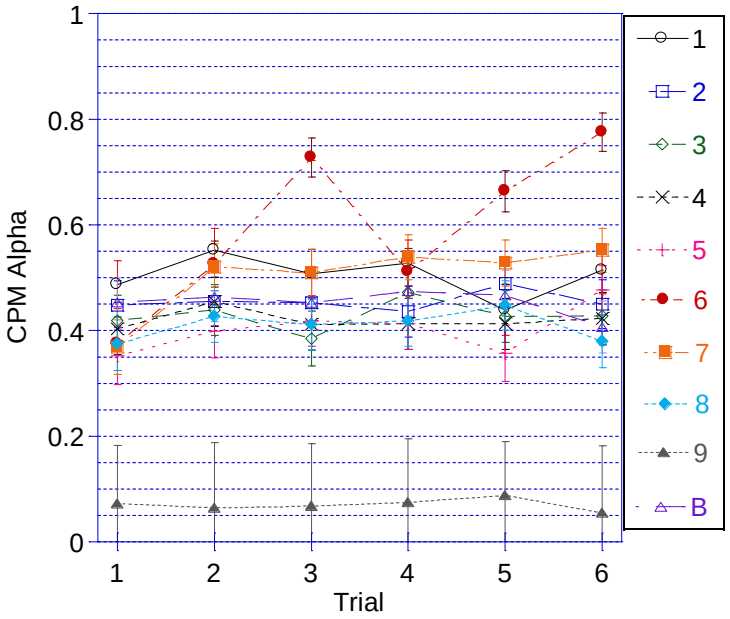


**Figure 36**. Core 6 – Slice 18, gross alpha count rates for 9 sub samples and 6 trials. Error bars may be covered by the data point markers. The background count rate is identified by 'B'.

## 4.7 Conclusions

These experiments have shown that hot particles contribute $^{241}$Am and Pu to the near field environment, producing both heterogeneous, or particle-like, and homogenous distribution patterns. The presence of micro particles in the soil presents both opportunity and problems. The opportunity arises in the area of forensics. These particles contain a great deal of information about their source term, but can only be detected through the use of high resolution screening techniques such as gamma spectroscopy and SEM. Because they are difficult to detect, and their dispersion in the soil column appears to be random, it is unlikely that they could be completely removed from an area where this type of material may have been dispersed. The problem occurs with modeling of the long term

transport of Am and Pu in the environment when particles are present. Chemically controlled processes like sorption/desorption driven transport can be modeled using statistical methods (37) because of the large number of small, continuous interactions that occur over time. Particles do not behave this way. They appear to have discrete distributions that make large, localized impacts on the concentrations of Pu and Am. Particles may also be mobile, subject to transport by mechanical rather than chemical processes. The potential for transport of micro particles by mechanical factors resulting in resuspension of this material needs to be studied in greater detail. Imaging techniques such as SEM and EDS should be employed to determine if the micro particles can be identified as independent entities, and if they are, then particle size distributions should be developed.

# CHAPTER 5

# IMAGING OF HOT PARTICLES

## 5.1 Abstract

Hot particles isolated from soils originating from the BOMARC site were imaged using scanning electron microscopy (SEM) coupled with energy dispersive spectroscopy (EDS), and synchrotron based x-ray fluorescence mapping (XRF). The two techniques are complimentary in that both surface and volume characteristics can be determined for the particles of interest. Analysis by SEM and EDS provided information about the morphology and elemental composition for each particle. Morphological differences were observed across the particle population and the elemental constituents were not homogenously distributed throughout the matrix. Five particles were selected for x-ray fluorescence mapping experiments. Fractionation of Pu, Am and U was observed in several of the particles and may be indicative of fire exposure during the accident. Several particles also contained Ga, a common dopant used for stabilizing δ-Pu (38).

## 5.2 Introduction

Hot particles from various nuclear events and accidents have been characterized by SEM and EDS (1,4,6,17,39-43). These methods provide surface morphology and composition data within several hours, require minimal sample preparation, and are non-destructive. Synchrotron based XRF imaging is complementary to SEM and has been previously used to characterize hot

particles from both the Palomares and Thule weapon accidents (40,42). The intensity and penetration depth of the x-rays that are generated permits elemental characterization of the matrix volume versus the near surface distribution sampled by the SEM based techniques. These volume based experiments provide additional information about the particle interaction with the environment. As an example, Am has built-up in the Pu matrix over time and gamma spectroscopy experiments have shown that it is distributed throughout the soil cores (Chapter 4). Mapping the Am distribution throughout the particle volume may determine if fractionation is occurring in the particle itself, or only at the surface. Another benefit of using a synchrotron-based mapping system is that the experimental setup can be easily modified to perform x-ray absorption fine structure (XAFS) experiments to characterize the oxidation state, speciation, and local structure of the matrix material.

Imaging the BOMARC particles provides information that is subject to both forensic and environmental interpretation. Particles originating from the same source term and dispersal conditions (pre-detonation fire) may be expected to share some common morphological characteristics and should be similar in nature. However, these particles have persisted in the environment for 48 years, from 1960 to 2008, and have been subject to a variety of weathering effects (Chapter 2) that may have influenced their morphologies. These particles are therefore a link between the past and present, and the challenge is to determine what physical characteristics can be attributed to the source term and how environmental processes have affected them over time. A population of hot

particles was isolated from various soil samples for non-destructive analysis by SEM/EDS. Five particles were selected for XRF experiments. The distribution of Pu, Am, U and Ga is discussed for both sets of particles.

## 5.3 Method Summary – XRF and SEM Experiments

### 5.3.1 XRF Experimental Setup

Hot particles were mounted in 25 mm epoxy pucks. The epoxy was then ground and polished, exposing a smooth surface of the particle. Optical and SEM images were taken of the polished particle surface for comparison with the XRF imaging experiments. The epoxy puck was cut to fit in the sample holder (Boyd Technologies, Manchester, CA), and fixed in place using a high temperature Si adhesive. A schematic of the sample containment is provided (Figure 37).

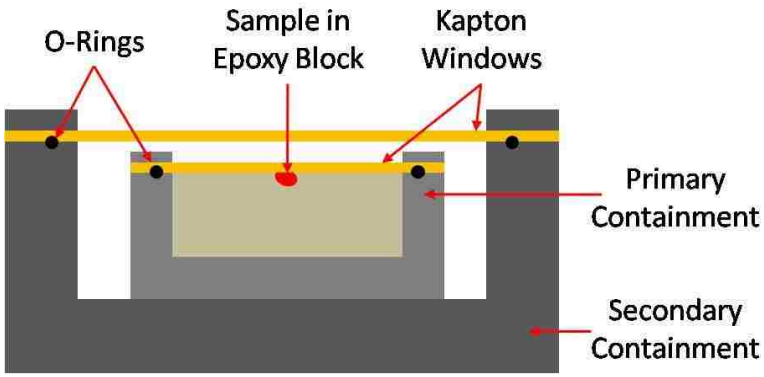


**Figure 37**. Illustration of the cross section of an assembled sample cell.

The XRF experiments were conducted at the Advanced Photon Source (APS) facility (Sector 10-ID, MR-CAT) at Argonne National Laboratory. The experimental set up for the multiple element mapping system is provided (Figure 38). The sample holder was mounted on a three axis staging platform at a 45º angle to the incident beam. The beam was focused to a 3 x 3 μm spot and passed through an ionization chamber to normalize the intensity of the beam hitting the surface of the sample.

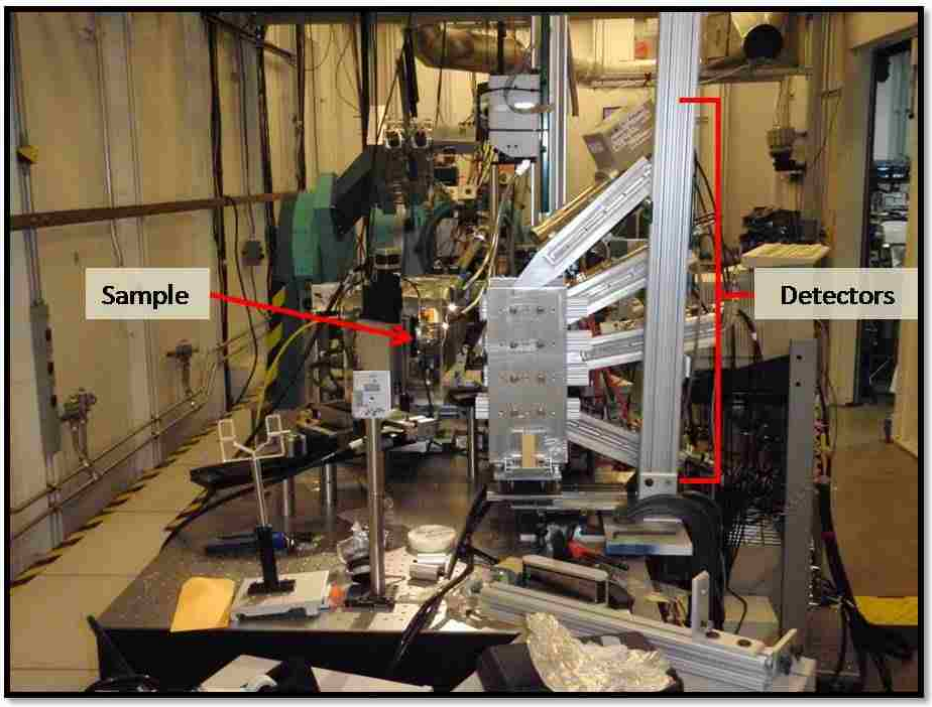


**Figure 38.** The experimental configuration for XRF experiments.

Elemental maps of the particle were created by incrementing the sample stage under the incident x-ray beam with 3 μm steps in both the horizontal and vertical directions. The detector suite collected the fluorescence signal for 0.5 to

3 seconds per step and the process was repeated until the entire surface of the particle was mapped. The fluorescence signal generated while the sample holder was in motion was discarded. Multiple detectors were used during the XRF experiments for simultaneous acquisition of Pu, Am, U and Ga signals to accelerate the mapping process. The observed $L_\alpha$ transitions of these elements are provided (Table 15). Elemental maps were acquired at incident beam energies of 18,600 - 18,650 eV and 17,180 - 18,000 eV. These energies are above the Am $L_3$ edge and below the Pu $L_3$ edge, respectively. The Pu signal at the lower beam energy was used to monitor for scatter or other signals that may not be visible in the high energy scan.

**Table 15.** Elements and the transitions observed during the mapping experiments (44).

| Element | Edge | Edge Energy (eV) | Observed Transition | Transition Energy (eV) |
|---|---|---|---|---|
| **Ga** | K | 10,367 | $K_{\alpha 1}$ (K-$L_3$) | 9,251 |
| **U** | $L_3$ | 17,166 | $L_{\alpha 1}$ ($L_3$-$M_5$) | 13,438 |
| **Pu** | $L_3$ | 18,057 | $L_{\alpha 1}$ ($L_3$-$M_5$) | 14,087 |
| **Am** | $L_3$ | 18,510 | $L_{\alpha 1}$ ($L_3$-$M_5$) | 14,414 |

5.3.2 XRF Image Processing

Images obtained from the mapping experiments were processed with Matlab Version 7.4 (29). The signal was normalized to the incident beam flux, to correct for drift ($\Delta$ = 10 – 15%), noise or other events that may have occurred during a mapping experiment. The filtered data sets were complied into a series of 2-D

arrays and plotted as 256 gray scale intensity maps. Image intensities were adjusted (45) and gamma corrected (27) to enhance the maps.

5.3.3 SEM Experimental Setup

Each hot particle was adhered to a 25 mm stainless steel planchet with a piece of double-sided carbon tape. Prior to imaging, the surface of the planchet was sputter-coated (Cressington 108) with Au for 30 seconds. The Au coating provides a conductive surface and has a minimal impact on electron interactions with the particle surface. Imaging experiments were performed on an SEM (JOEL 5610) equipped with an EDS (Oxford, 6587) controlled with INCA x-ray microanalysis (Oxford, version 4.11). The accelerating voltage ranged from 20 to 30 kV to induce $L_{\alpha}$ transitions of the actinides of interest.

Hot particles were located in backscatter mode under low magnification (18-30X) by manually scanning the surface of the carbon tape. Using this technique, any material containing high Z components appeared as bright objects in the field of view. Only a few grains of material besides the hot particle were introduced to the surface of the carbon tape which reduced the probability that the hot particle could be obscured by material from the soil matrix.

Particles located in backscatter mode were then imaged by secondary electron imaging (SEI) to produce high resolution images for morphological characterization. Both SEI and BES images were used to select regions of interest for EDS analysis. Several spectra were acquired at points across the particle surface to identify elemental composition, and elemental mapping analyses were also completed for selected areas. Point experiments produced

spectra based on the x-rays generated from the material incident to a fixed primary beam position and are collected in under 5 minutes. Elemental maps are created by rastering the primary beam over a region of interest and collecting the x-ray signal with position data. The mapping experiments can take several hours to perform and are very sensitive to sample morphology. In cases where the morphology of the particle is highly irregular, the electron beam or the x-ray detector's field of view may be blocked by structures on the sample surface, preventing acquisition of the mapping data.

## 5.4 Results and Discussions

### 5.4.1 Volume Composition – XRF Analysis

The Pu, Am, U and Ga distribution maps are provided in sequence and are numbered 2 – 5 respectively for each of the imaged particles. Brighter areas indicate high elemental concentrations while darker regions indicate lower elemental concentrations. Without reference materials for comparison the elemental intensities cannot be directly compared in terms of atom percent composition between particles. The outer boundary of the particle is outlined in each map and an optical image is included for comparison (top image, labeled 1). The elemental distribution in Particle 1 (Figure 39) is homogeneous; with the exception of two bright spots on the edge of the U map (Image 4). These spots were confirmed in the maps obtained at the lower beam energy and are not likely artifacts. The bright streaks along some areas of the particle boundary were

assumed to be a by-product of the polishing process where fines were trapped at the interface between the epoxy and particle.

The optical image of Particle 2 contains bright white regions distributed throughout the cross-sectional area (Figure 40) which corresponds to a band of Ga (Image 5) that cuts across the top half of the particle. Plutonium and Am are homogenously distributed throughout the particle; however, some bright regions were identified in the U map (Image 4). Plutonium and Ga intensities are homogenous in Particle 3 (Figure 41), but U and Am are unevenly distributed. The swirled pattern in the U map is similar to the morphological feature in the optical image. It is possible that separate U and Pu components fused during the accident, which would lead to the mixing pattern. This has been observed for other particles originating from a WGPu matrix (42). The Am was also more concentrated in the swirled region; however, the brightest Am spots are in areas where the U is depleted. Uranium and Ga are concentrated in the central region of Particle 4 (Figure 42), while Pu and Am are evenly distributed across most of the particle. The Ga and U distributions have the same shape and appear to fill the voids in both the Pu and Am maps.

Plutonium and Ga intensities are homogenous in Particle 3 (Figure 41), but U and Am are unevenly distributed. The swirled pattern in the U map is similar to the morphological feature in the optical image. It is possible that separate U and Pu components fused during the accident, which would lead to the mixing pattern. This has been observed for other particles originating from a WGPu matrix (42). The Am was also more concentrated in the swirled region; however,

the brightest Am spots are in areas where the U is depleted. Uranium and Ga are concentrated in the central region of Particle 4 (Figure 42), while Pu and Am are evenly distributed across most of the particle. The Ga and U distributions have the same shape and appear to fill the voids in both the Pu and Am maps. The dominant feature of Particle 5 (Figure 43) is the undefined particle edge in the distribution maps (Images 2-5). This may be indicative of fines that were removed and embedded in the epoxy during the polishing process, which is more pronounced in this particle than others. The excessive sloughing indicates the mechanical properties of the particle are significantly different from the other particles. Within the boundaries established by the optical image, the U signal was concentrated in areas where Am and Pu were depleted. It is possible that U is layered on top of the Pu matrix, attenuating both the Am and Pu signals. This observation is supported by the layered characteristic of the particle surface in the optical image (Image 1).

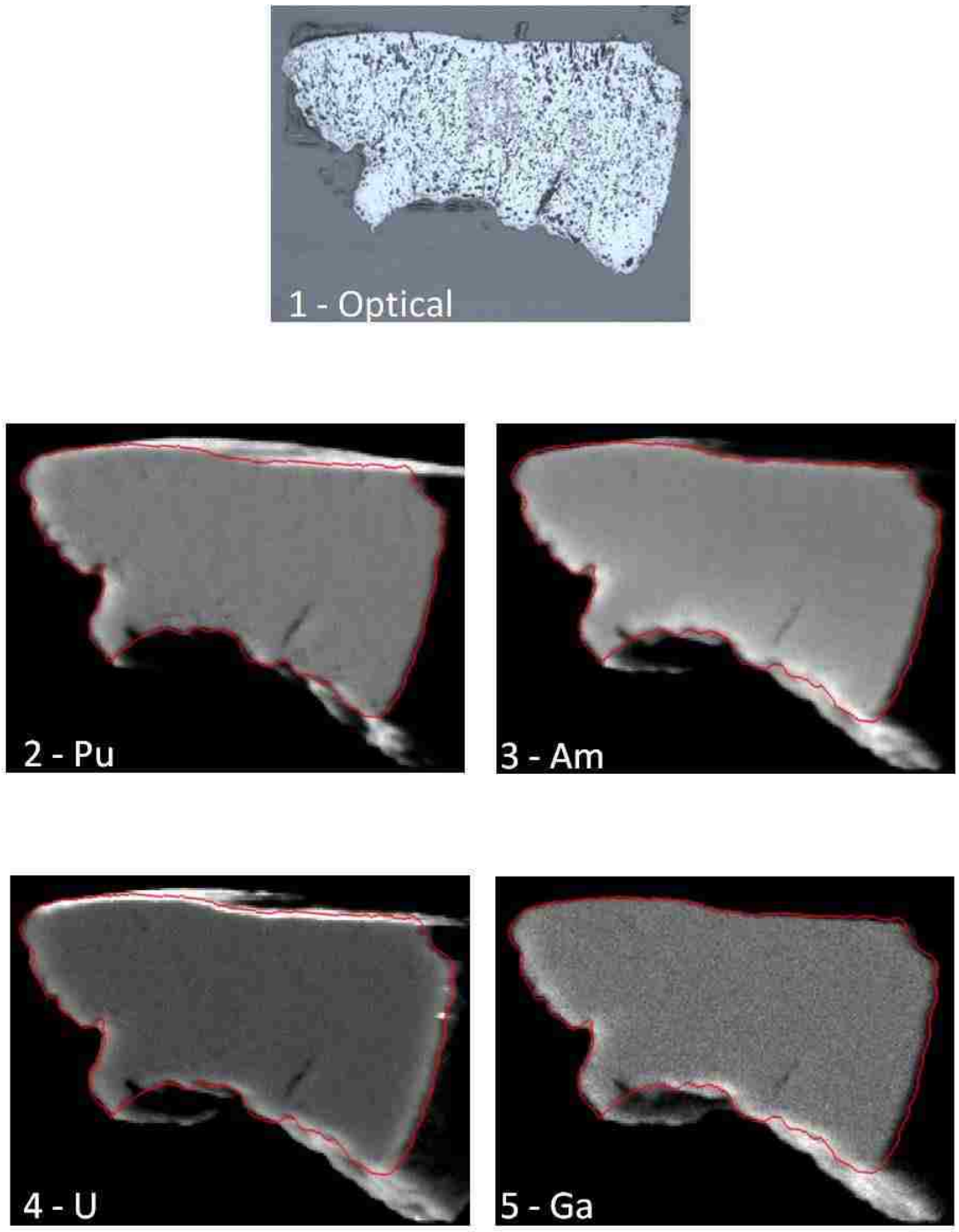


**Figure 39.** Elemental distribution maps for Particle 1.

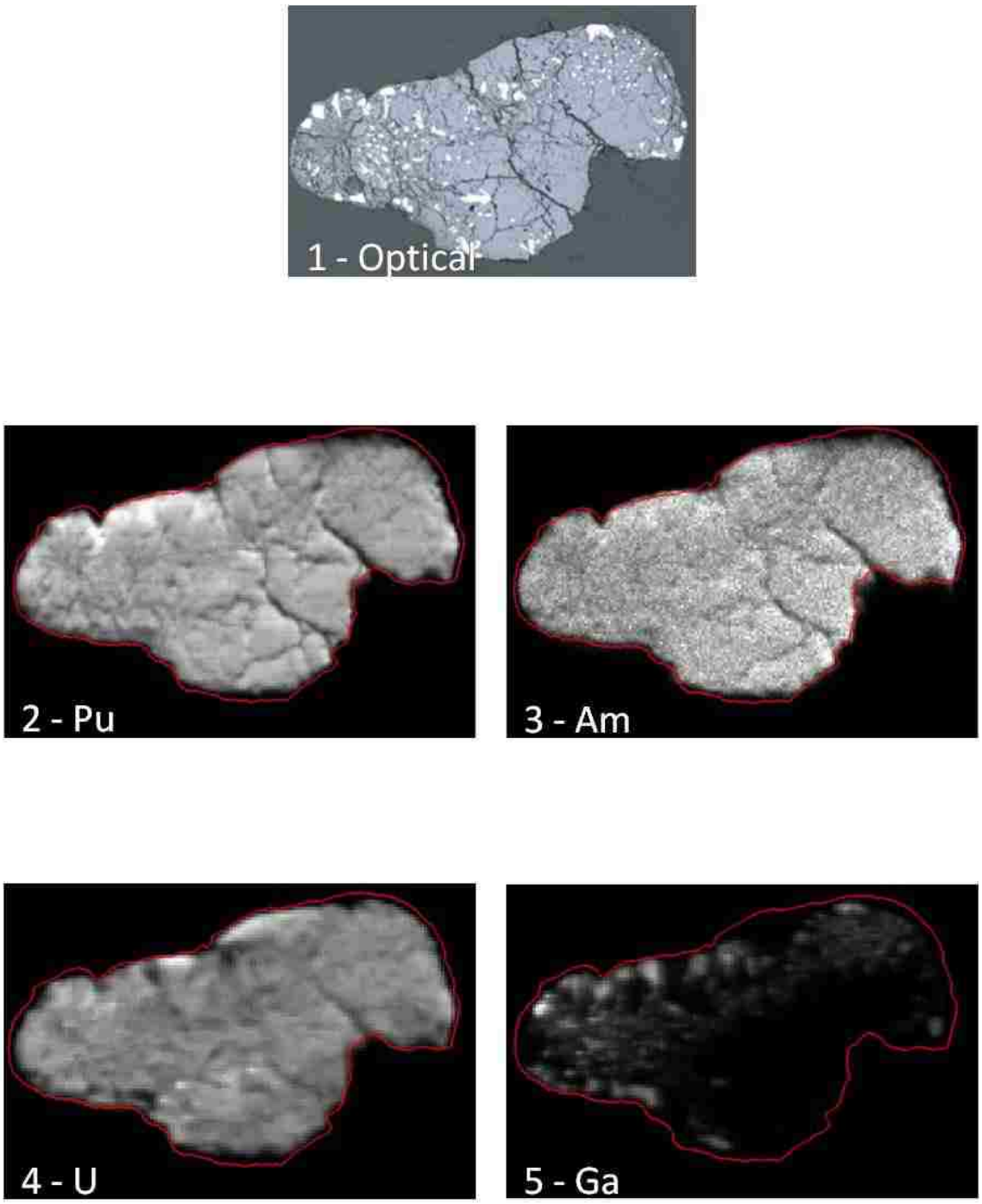


**Figure 40.** Elemental distribution maps for Particle 2.

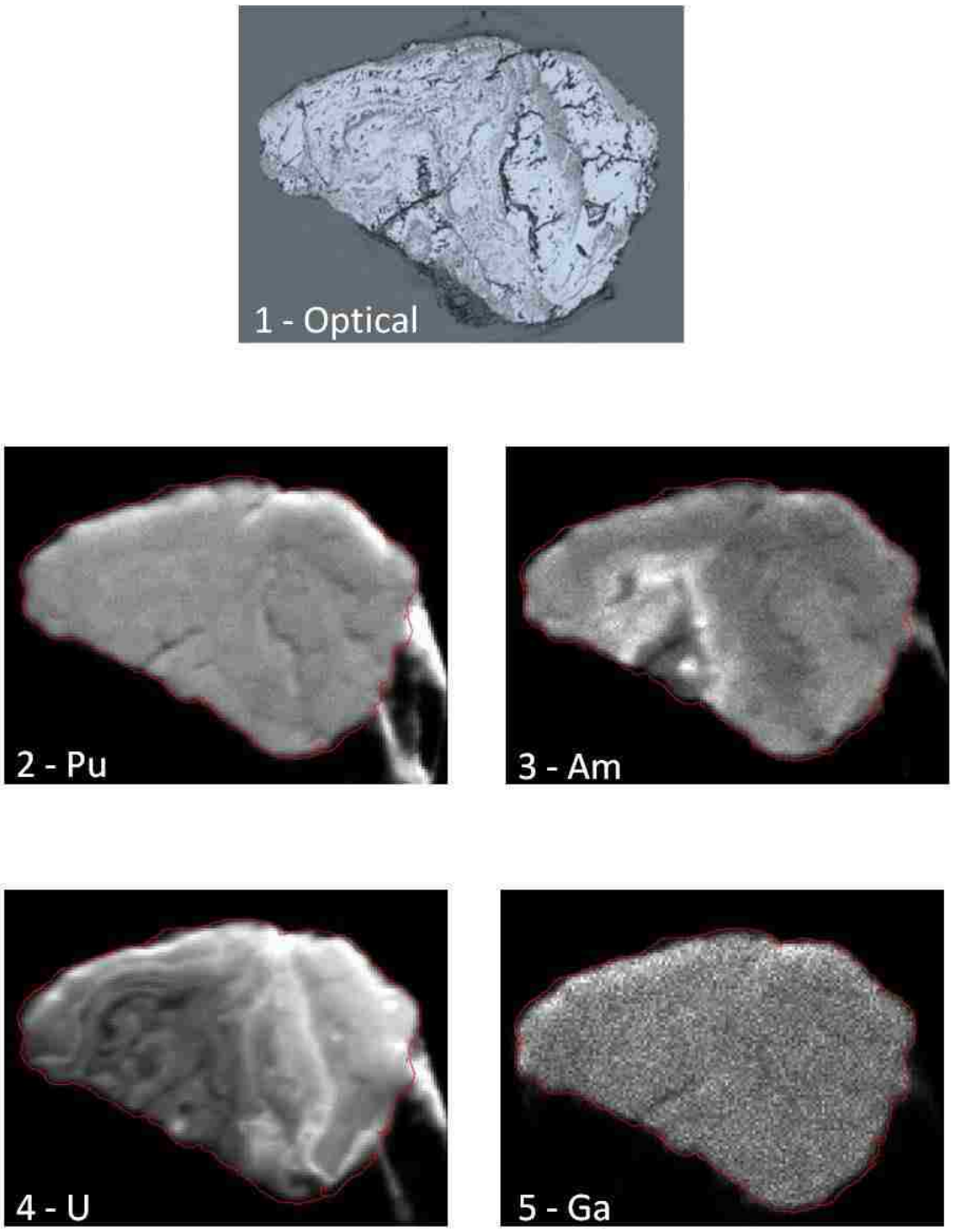


**Figure 41.** Elemental distribution maps for Particle 3.

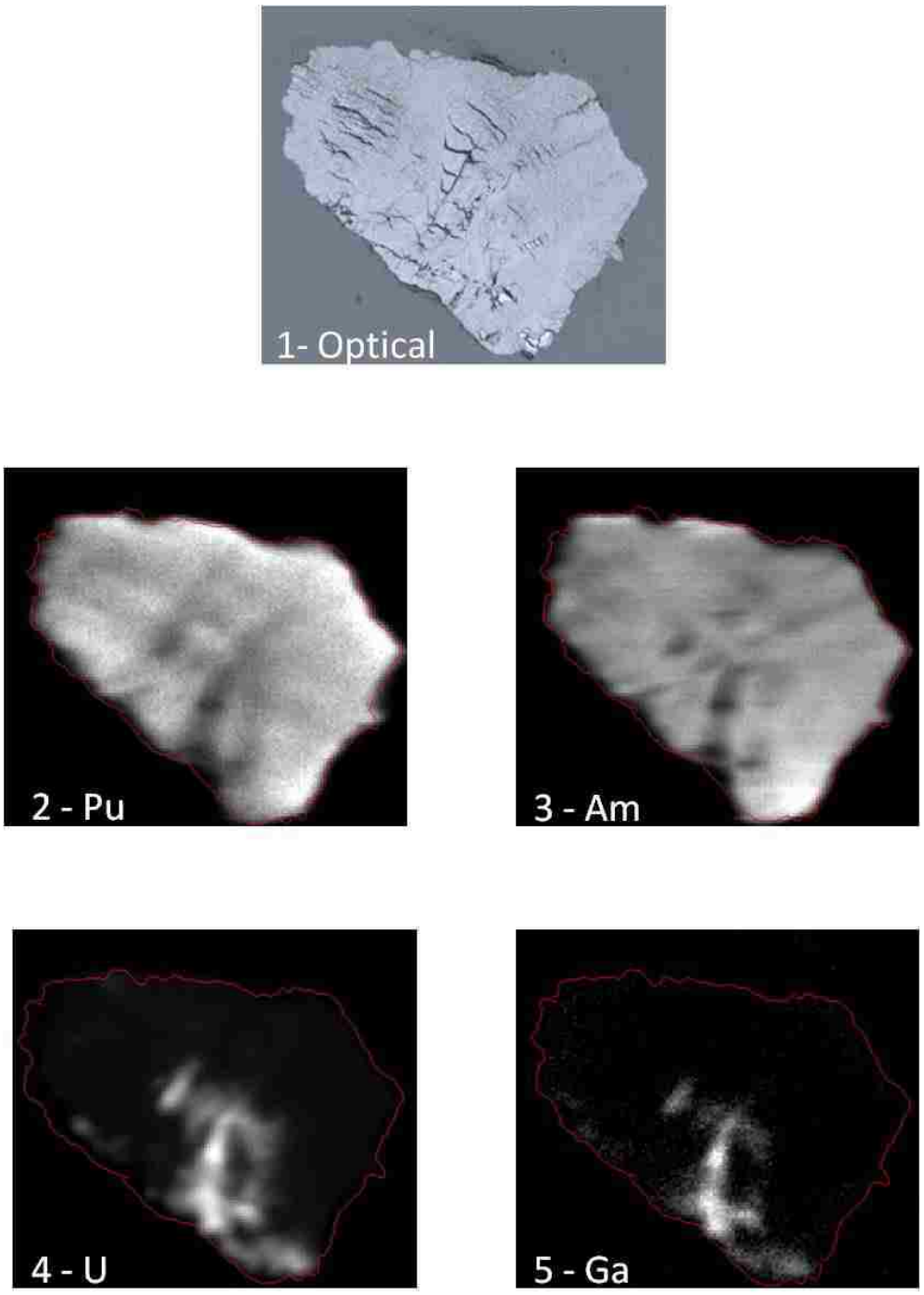


**Figure 42.** Elemental distribution maps for Particle 4.

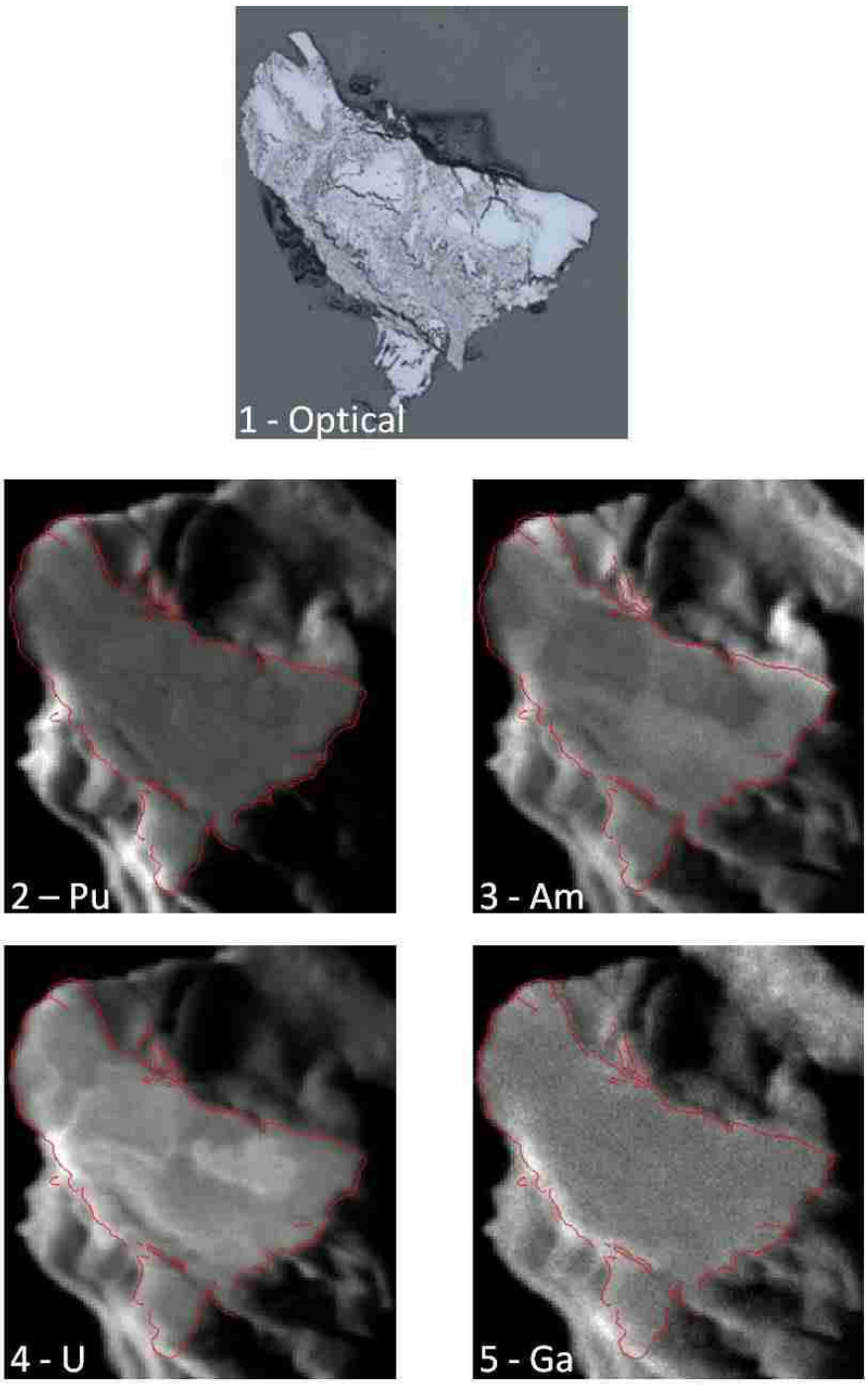


**Figure 43.** Elemental distribution maps for Particle 5.

### 5.4.2 Particle Morphology and Surface Composition - SEI/EDS Analysis

Images were acquired for the particle population (n = 16) between 100x and 700x magnification depending on the particle size using SEI (Figure 44 and Figure 45). The morphological characteristics of each particle are unique, despite originating from the same incident. Limited information can be derived about the structural differences in the SEI images without reference material for comparison. It is unclear if these differences are from environmental processes or from the initial incident. Each particle was analyzed by EDS to confirm the presence of Pu and U and to identify other surface matrix constituents.

An example of the spectral data and image files is provided (Figure 46). Two regions of interest were selected for point analysis on the particle. In the BES image they are the dark center region (labeled 1) and the brighter surrounding edges (labeled 2). The dark region implies that this material has a lower average Z value relative to the brighter surrounding material. The EDS spectra indicated that U was the primary constituent of the dark region (labeled 1) and the lighter regions were primarily Pu (labeled 2).

Most particles analyzed by EDS contained a mixture of Pu and U, but the distribution was not homogenous across the population. Surface elemental mapping was completed for two particles (Figure 47 and Figure 48). The first particle contained U depleted regions relative to Pu (Figure 47). Plutonium and O were evenly distributed across the surface of the particle while U, Ga, Si and Al were concentrated in specific regions. The dark areas in the Pu map correlate with intense Al or Si signals and Ga was concentrated in O depleted regions.

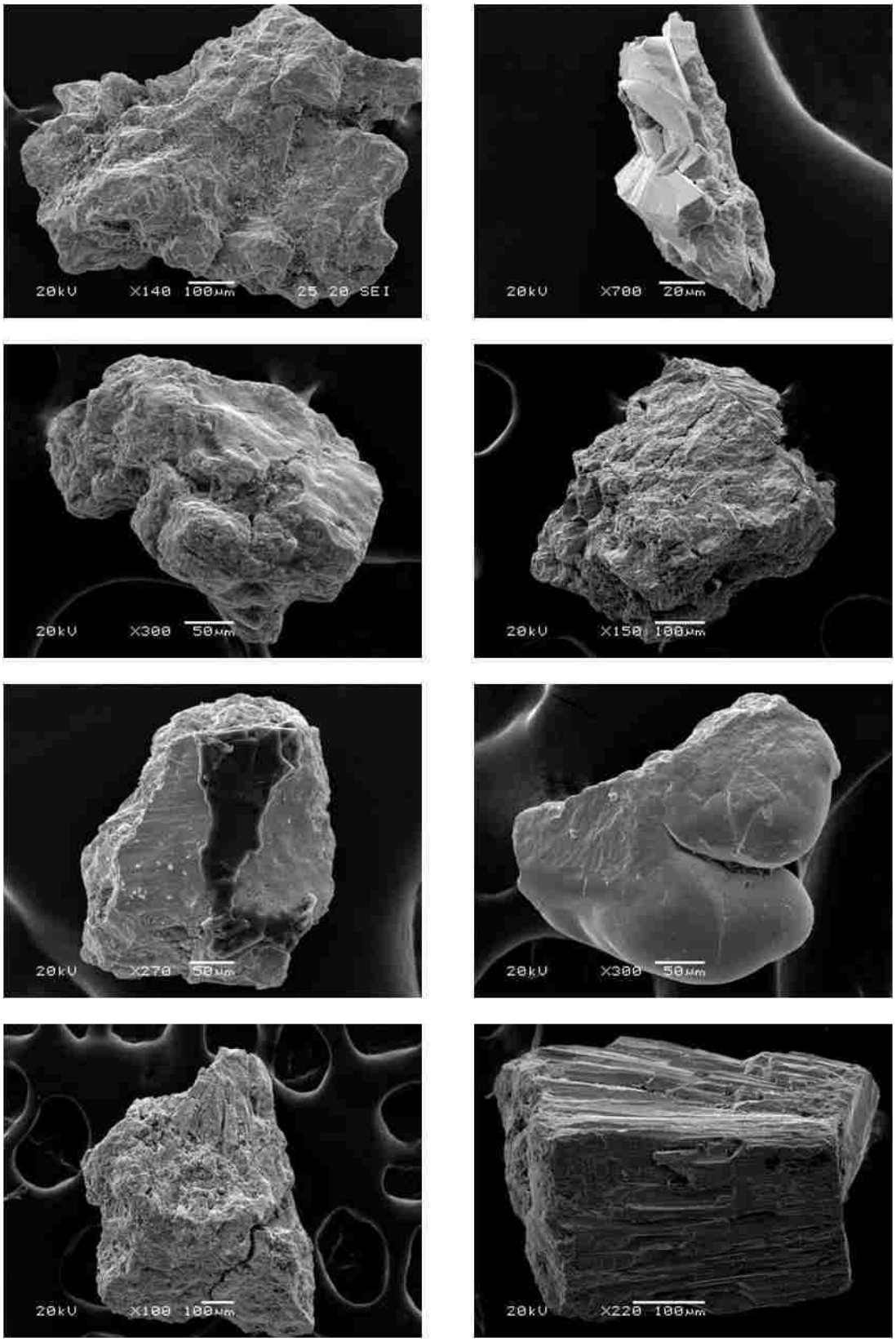


**Figure 44.** Secondary electron images of 8 particles (set 1 of 2).

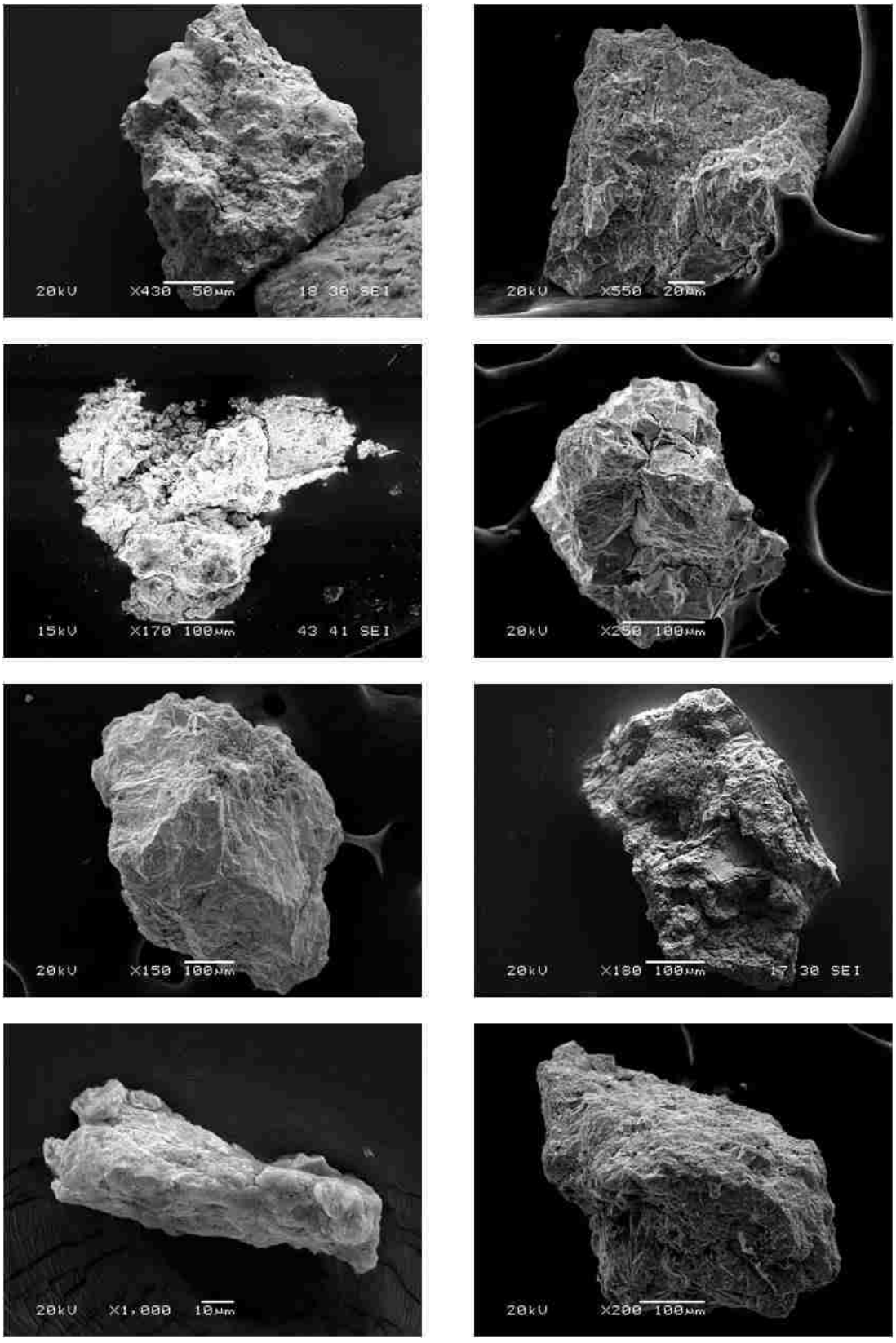


**Figure 45**. Secondary electron images of 8 particles (set 2 of 2).

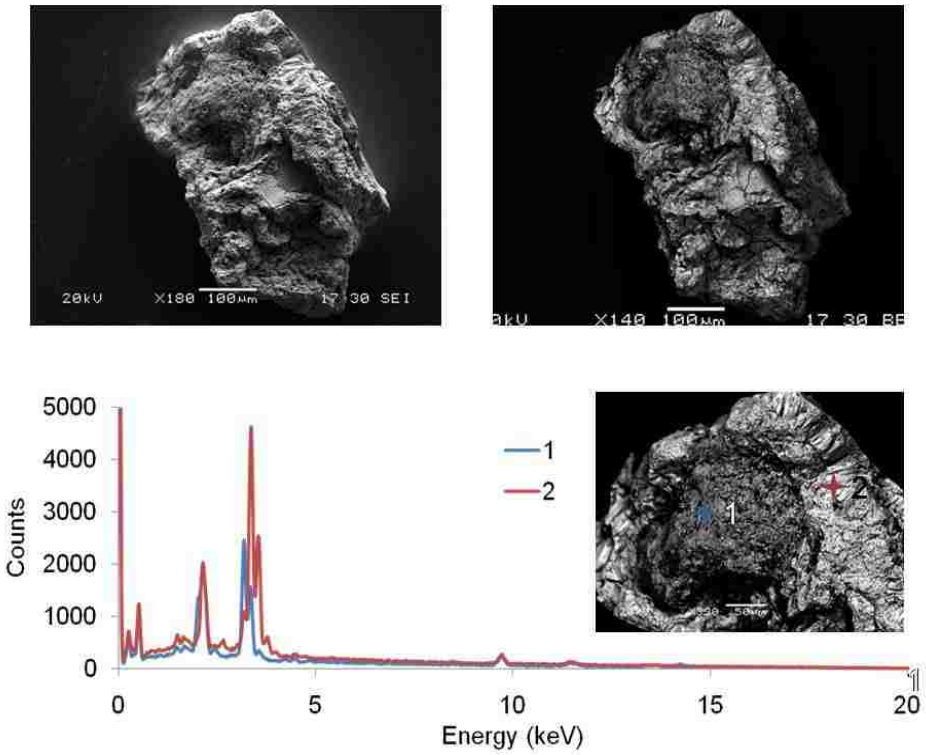


**Figure 46.** The SEI (left) and BES (right) images for an isolated hot particle. The EDS spectra are for the two points highlighted in the image (lower right).

The distribution of Pu and U in the second particle was homogeneous (Figure 48). Aluminum and Si were detected in isolated regions of the particle, and the most intense O signal was associated with Al. Point spectra analysis of the particle population determined that Al, O and Si were present in most of the particle population.

Data from the elemental maps can be used to correlate matrix composition and structure (Figure 49). The Pu and U signals from the elemental maps were averaged along the vertical axis (top to bottom) and plotted over the SEI image. The U signal decrease is consistent with changes in morphology, while the Pu signal remains unaffected.

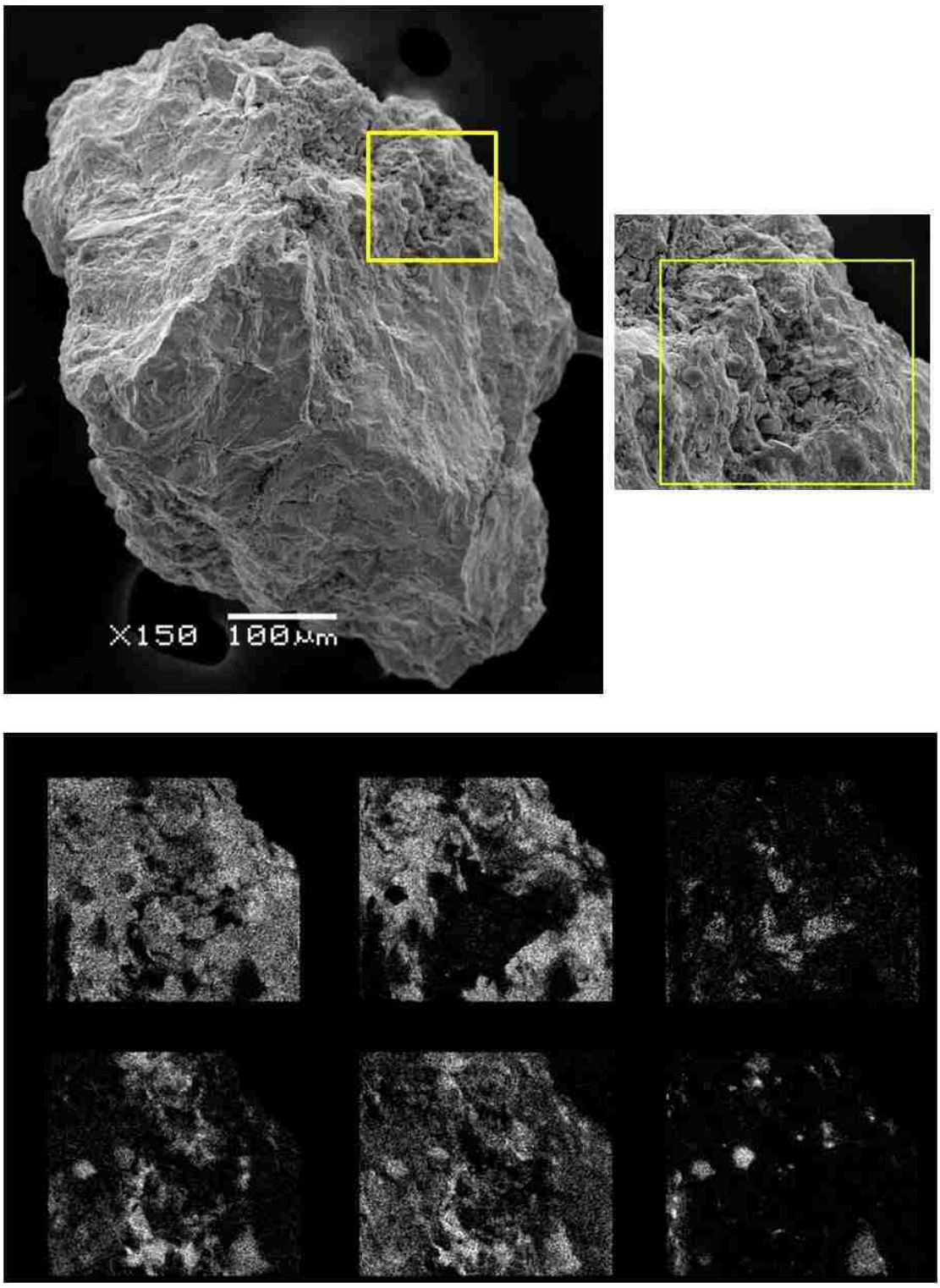


**Figure 47.** Elemental maps of the region defined by the yellow square, from the top left and moving clockwise are Pu, U, Ga, Si, O and Al

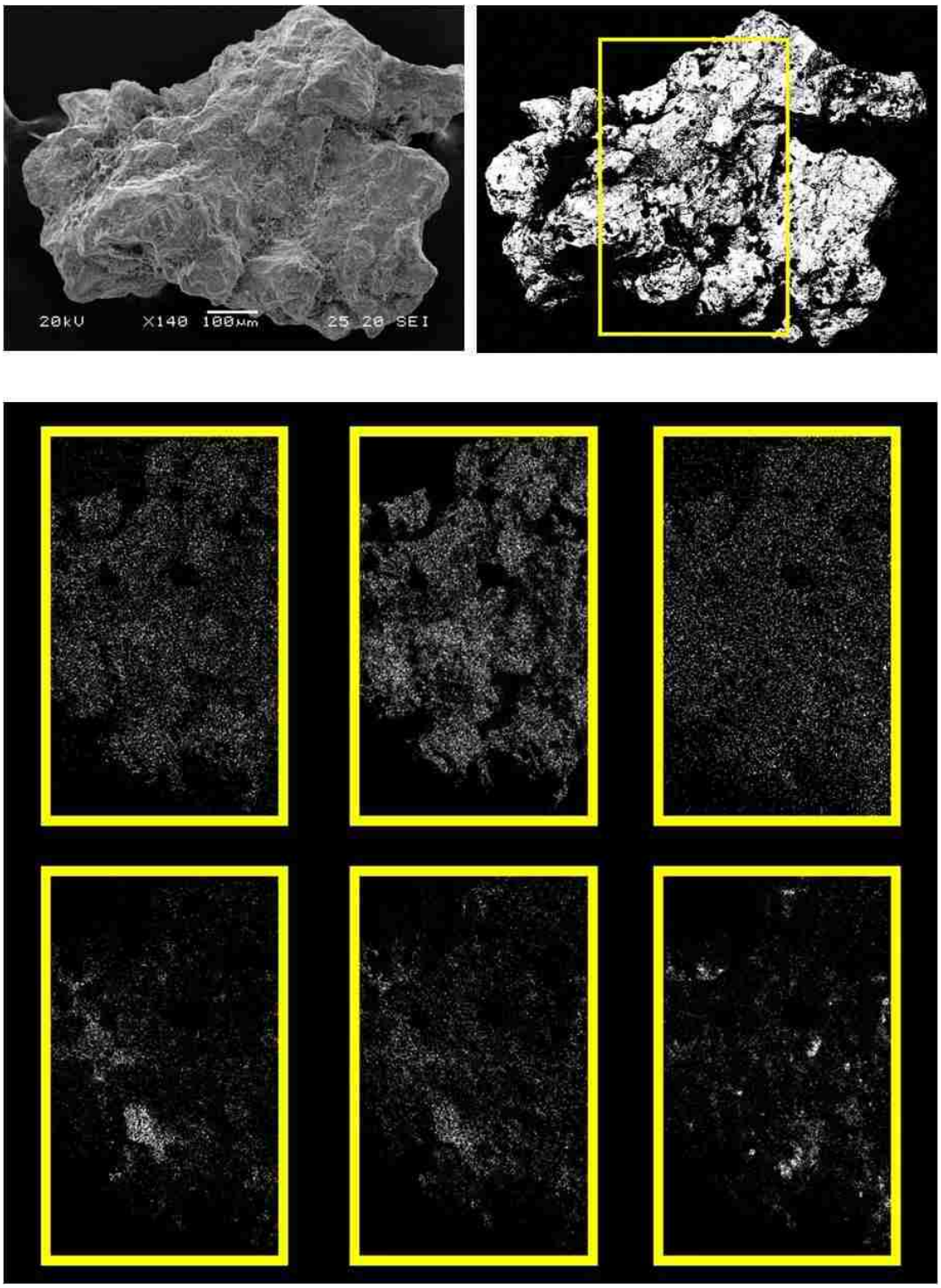


**Figure 48.** Elemental maps of the region defined by the yellow rectangle, from the top left and moving clockwise are Pu, U, Fe, Si, O and Al

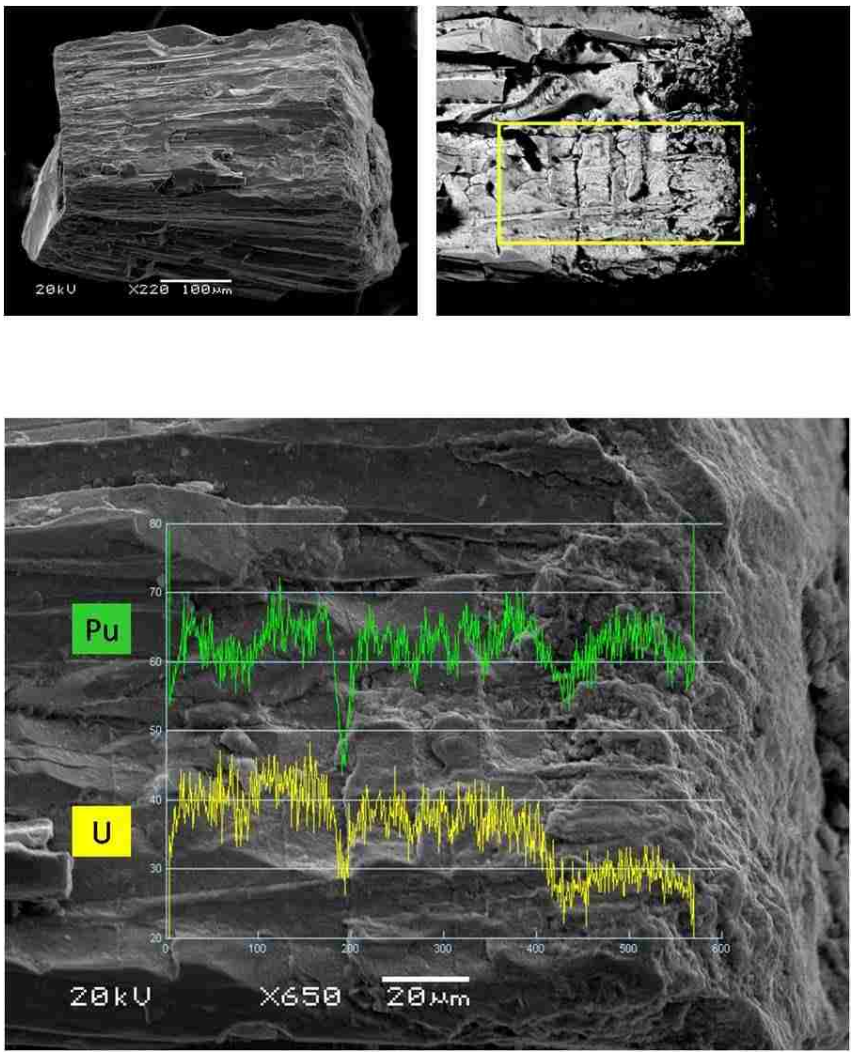


**Figure 49.** The result of signal averaging Pu and U maps along the vertical axis (top to bottom).

## 5.5 Conclusions

Rapid determination of hot particle morphology and surface composition can be accomplished by SEM and EDS. Once isolated, a hot particle can be mounted, imaged and mapped within several hours. The length of the experiment is dependent on the level of detail required, i.e. how much of the particle surface must be characterized. If there are no time or resource

constraints and damage to the sample is permissible, then synchrotron based XRF mapping experiments should be considered. They provide invaluable data about the distribution of elements within the volume of the sample

The combined SEI, EDS and XRF data illustrates that particles originating from the same source under similar conditions can have different morphologies and elemental distributions. It cannot be assumed that a single isolated sample is representative of all particles dispersed during the accident. Extrapolated data from a small population should not be used to represent the source term unless the homogeneity of the particles can be confirmed.

To fully leverage SEM as an analytical tool for nuclear forensic or environmental work, a more comprehensive approach to data analysis and collection needs to be taken. Data obtained by EDS should be referenced against well-characterized Pu and U standards so that relative distribution ratios can be quantified. These standards are not currently available, but should be developed and characterized for future particle studies.

Ideally, imaging and analysis should be performed in parallel. An SEI image acquired would be processed simultaneously to identify regions on the particle surface that fit a set of pre-defined morphological characteristics. Then EDS spectra could be acquired in these regions to match morphology with composition data for each particle. The combined data set could then be referenced against an EDS/SEI database of particles both synthetic and environmental in origin. Synthetic particles would be especially useful because

the production conditions would be known and they could also be used as industrial standards for quality assurance purposes.

A combined imaging, analysis and database system would help organize the large quantities of information that is available in these high resolution datasets. From an environmental perspective, the capability of associating the morphologies observed on the surface of the particles with a chemical structure could provide insight into degradation mechanisms and kinetics. From a nuclear forensic perspective, understanding the conditions required to form the surface morphologies could prove valuable in identifying the production mechanisms and source term of a particle. The utility of imaging will not be fully realized until an integrated imaging and analysis system is developed.

# CHAPTER 6

# RADIOANALYTICAL CHARACTERIZATION OF HOT PARTICLES – GAMMA SPECTROSCOPY

## 6.1 Abstract

Hot particles were isolated from the BOMARC soil samples and analyzed by high resolution gamma spectroscopy. This non-destructive technique provides information about the isotopic constituents for the WGPu matrix, which can be used for source term identification and radiometric dating assuming single source origination. Particles were characterized using a planar broad energy spectrum germanium (BEGE) detector, for photons in the 0-520 keV region. Isotopic ratios for $^{241}$Am, $^{241}$Pu, $^{237}$U, and $^{235}$U relative to $^{239}$Pu were determined for each particle. A detailed description of the peak fitting parameters used for spectral analysis is presented along with the relative isotopic concentrations of the particle population (n = 20).

## 6.2 Introduction

Direct analysis of hot particles by gamma spectroscopy provides information for both environmental and forensic interpretation. The data collection process is straight forward, i.e. the particles are placed in some type of containment vessel for contamination control and reproducible counting geometry, and then placed in the detector shield and counted for a specified time interval. The challenge arises with spectral interpretation. An example of the WGPu hot particle gamma spectrum collected on a BEGE detector over 24 hours is provided (Figure 50).

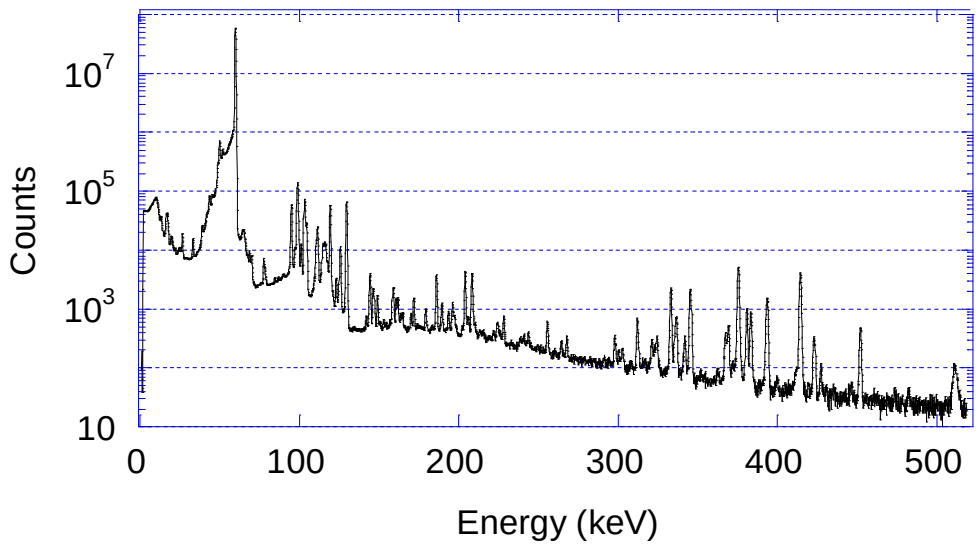


**Figure 50.** Gamma spectrum of a WGPu hot particle using a BEGE detector and 24 hour count time.

The complex collection of overlapping peaks and the elevated background continuum are due to the similarities of the nuclear and electronic structures of the Pu isotopes and various daughter products that are present in the particle matrix. As an example, the prominent triplet of peaks centered at 100 keV (Figure 50) is from a collection of decay events (Table 16). These overlapping peak areas make quantification of individual isotopes difficult even when the matrix constituents are known. Analysis is therefore focused on photon peaks that are unique to individual isotopes, or sets of peaks in close proximity that have only two components.

Peak selection is based on photon energy and yield, and the detection efficiency of the gamma system. Additionally, count times must be such that sufficient counts are collected for statistical purposes. Other factors of concern

include introduced noise such as X-ray escape peaks due to electron transitions in the detector material, sum peaks caused by two independent photons striking the detector within its resolving time, or rapid rises in the background continuum.

**Table 16.** Photon energies of various Pu isotopes and progeny centered around 100 keV (16).

| Radionuclide | Energy (keV) | Yield (%) |
|---|---|---|
| $^{238}$Pu | 98.434<br>99.853 | 9.25E-5<br>7.29E-3 |
| $^{239}$Pu | 98.434<br>98.780<br>103.060 | 5.8E-3<br>1.47E-3<br>2.16E-4 |
| $^{240}$Pu | 98.434<br>104.234 | 4.05E-5<br>7.14E-3 |
| $^{241}$Pu | 98.434<br>103.680 | 4.99E-5<br>1.01E-4 |
| $^{242}$Pu | 98.434<br>103.50 | 2.89E-5<br>2.55E-3 |
| $^{234}$U | 104.819<br>105.604 | 5.8E-4<br>1.11E-3 |
| $^{235}$U | 96.09<br>104.819<br>105.604 | 0.091<br>0.693<br>1.32 |
| $^{237}$U | 97.069<br>101.059<br>102.98 | 15.4<br>24.5<br>6.4E-3 |
| $^{241}$Am | 98.97<br>101.059<br>102.98 | 0.0203<br>1.81E-3<br>0.0195 |

Although absolute activities of individual isotopes can be calculated for each hot particle, it is best expressed as activity ratios generated from individual spectra. Direct comparison of absolute activity data is difficult because of the wide range of activity levels of individual hot particles, i.e. 3000 Bq to 500 kBq

$^{239}$Pu, resulting in detector dead time values between 0.3% and 26.5%. Higher dead time can lead to undercounting of the peak signal, increased pulse pile up and/or summation peaks. Rather than recalibrating the instrument for each individual hot particle, a single calibration curve can be generated assuming that any shifts in the system efficiency would be reflected across most of the energy spectrum. It should be noted that efficiency will be affected by internal attenuation of the particles at lower energies, independent of dead time.

Three isotopic ratios relative to $^{239}$Pu can be determined from a hot particle spectrum: $^{241}$Am, $^{235}$U, and $^{241}$Pu. The $^{241}$Am:$^{239}$Pu ratio is useful in studying the environmental impact of the hot particles on surrounding soils. Hot particles were removed from the cored soil samples and gamma analysis was performed on vertically sectioned slices of the remaining soil (Chapter 4). By comparing the $^{241}$Am:$^{239}$Pu ratio in the soil to those observed in the hot particles, it can be determined if the hot particle matrix is being broken down by dissolution, physical processes, or a combination of both. The $^{235}$U:$^{239}$Pu ratio helps define where the particle originated from within the weapon and how the weapon may have been assembled. Elevated levels of $^{235}$U in the particles indicate that highly enriched uranium (HEU) was also present in the weapon. The $^{241}$Pu:$^{239}$Pu ratio can be used as a direct dating tool to define material production period, provided the original composition of the material is known (7, 46).

## 6.3 Methods and Materials

### 6.3.1 Gamma Spectroscopy System Efficiency and Measurements

Experiments were initiated with two HPGE detectors, a 59.5 mm closed end coaxial detector (GC3020, Canberra Industries) and a 69.5 mm diameter, 20 mm thick planar detector with a carbon composite window (BE 3820, Canberra Industries). A comparison of the full width half maximum (FWHM) and total system efficiencies of both detectors for the same sample set is given (Table 17). The planar detector had superior total system efficiencies and peak resolution across a broad energy range; therefore, the experiments with the coaxial detector were abandoned. Two sources were used for detector calibration. An $^{241}$Am point source with an activity of 40952 Bq ± 5% was used for geometry calibration. A $^{239}$Pu disk source (25 mm diameter, 2396 Bq ± 5%) was used for energy calibration and to determine the relative efficiencies for the major $^{239}$Pu photons.

Gamma spectra for n = 20 hot particles were acquired until sufficient counts were collected in the photon peaks of interest. Specific count times are provided with the data. Two sample geometries were used for these experiments. The hot particle was either fixed to a carbon tape disk and 25 mm steel planchet (sample preparation for imaging studies) or placed in the bottom of a capped 1.5 mL centrifuge tube (initial containment, post soil separation). The particles were centered on the detector face and elevated a maximum of 3 mm above the surface of the detector.

**Table 17.** FWHM and system efficiency values for a planar (BEGE) at various photon energies for selected hot particles.

| Detector | Canberra BE 3820 – Planar | | | | | | |
|---|---|---|---|---|---|---|---|
| **Sample** | **HP1** | **HP2** | **HP3** | **HP4** | **HP5** | **Avg** | **System Efficiency** |
| **Count Time (sec)** | 74517 | 125193 | 120000 | 86400 | 70477 | | |
| **59.5 keV FWHM** | 0.714 | 0.712 | 0.706 | 0.716 | 0.708 | 0.711± 0.003 | 0.243 ±0.012 |
| **129 keV FWHM** | 0.828 | 0.81 | 0.82 | 0.816 | 0.815 | 0.818± 0.005 | 0.185 ±0.01 |
| **414 keV FWHM** | 1.196 | 1.21 | 1.223 | 1.175 | 1.199 | 1.201± 0.015 | 0.062 ±0.003 |
| **Detector** | **Canberra GC 3020 – Coaxial** | | | | | | |
| **Sample** | **HP1** | **HP2** | **HP3** | **HP4** | **HP5** | **Avg** | **System Efficiency** |
| **Count Time (sec)** | 66000 | 17577 | 80158 | 85541 | 82057 | | |
| **59.5 keV FWHM** | 1.183 | 1.191 | 1.281 | 1.226 | 1.127 | 1.202± 0.046 | 0.027 ±0.001 |
| **129 keV FWHM** | 1.249 | 1.327 | 1.427 | 1.271 | 1.223 | 1.299± 0.066 | 0.167 ±0.084 |
| **414 keV FWHM** | 1.541 | 1.988 | 2.458 | 1.497 | 1.601 | 1.817± 0.333 | 0.067 ±0.003 |

6.3.2 Gamma Analysis of Unprocessed WGPu Hot Particles: Peak Selection

Both gamma systems utilized GENIE 2000 Gamma Acquisition & Analysis v3.1a software (Canberra Industries). Peak area analysis was performed using the standard manufacturer software and Interactive Peak Fit V1.2 (IPF, Canberra Industries). Peaks were initially located using the unidentified 2$^{nd}$ differential tool, and final area calculation made using IPF, with a sum/non-linear least square fit algorithm and a step function for continuum calculation. Screen shots of the IPF

peak fitting software are provided for both singlet and doublet peak analysis (Figure 51 and Figure 52).

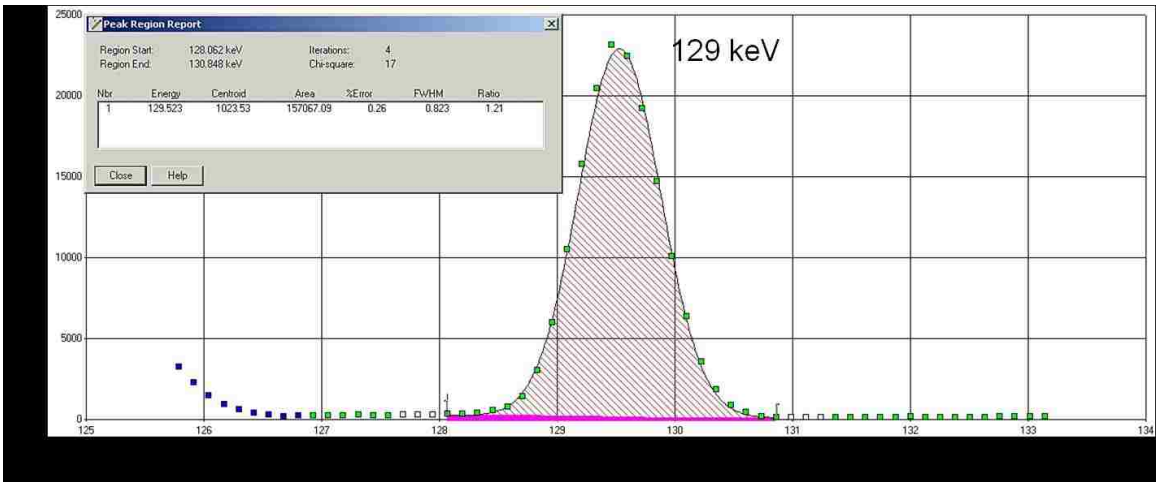


**Figure 51.** Screen shot of the IPF software used for singlet peak integration and background subtraction.

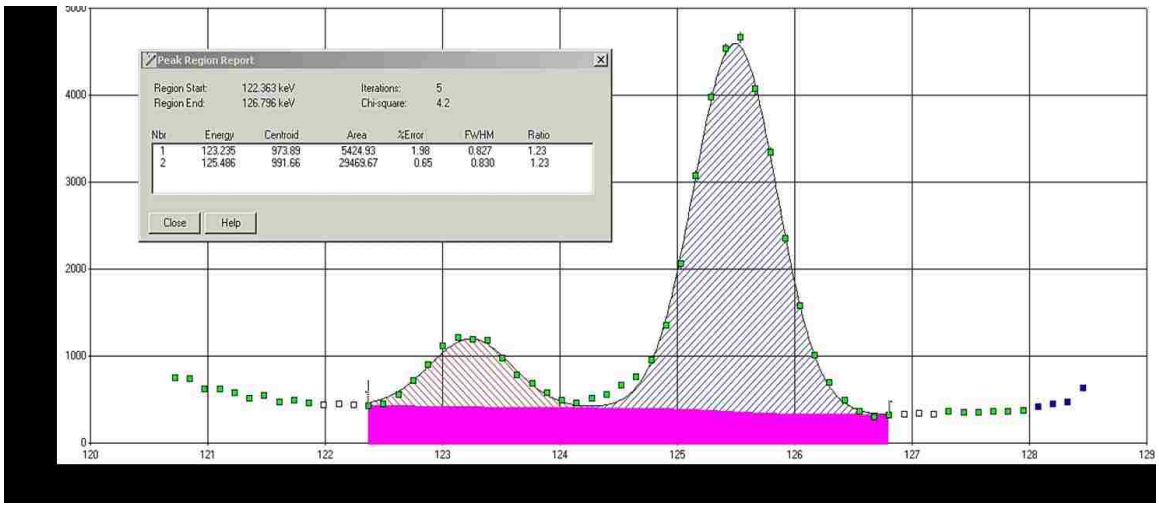


**Figure 52.** Screen shot of the IPF software used for a doublet peak integration and background subtraction.

**Table 18.** Energy and yields of the photons associated with the peaks analyzed in these experiments (16).

| Radionuclide | Energy (keV) | Yield (%) |
|---|---|---|
| **Doublet 123-125 keV** | | |
| **$^{241}$Am** | 123.052 | 1E-3 |
| **$^{239}$Pu** | 123.228 | 1.6E-9 |
| **$^{239}$Pu** | 123.62 | 2.37E-5 |
| **$^{239}$Pu** | 124.51 | 6.81E-5 |
| **$^{239}$Pu** | 125.21 | 5.63E-5 |
| **$^{241}$Am** | 125.3 | 4.80E-3 |
| **Singlet 129 keV** | | |
| **$^{239}$Pu** | 129.296 | 6.31E-3 |
| **Singlet 148 keV** | | |
| **$^{241}$Pu** | 148.567 | 1.86E-4 |
| **Singlet 185 keV** | | |
| **$^{235}$U** | 185.715 | 57.2 |
| **Multiplet 203-208 keV** | | |
| **$^{239}$Pu** | 203.55 | 5.69E-4 |
| **$^{241}$Am** | 204.06 | 2.90E-6 |
| **$^{235}$U** | 205.311 | 5.01 |
| **$^{241}$Am** | 208.005 | 7.91E-4 |
| **$^{237}$U** | 208.01 | 21.2 |
| **Doublet 335-336 keV** | | |
| **$^{241}$Am** | 335.37 | 4.96E-4 |
| **$^{239}$Pu** | 336.113 | 1.120E-4 |

The primary photon peaks used for the ratio analysis are provided (Table 18). The singlet $^{239}$Pu peak was used for relative ratio analyses. This peak was selected because it is above the energy range where the background continuum rises rapidly, has good yield and is in a high efficiency area for the detector (18.4 ± 0.09%). The 123-125 keV doublet (Table 18) was selected for $^{241}$Am because a more accurate background subtraction could be performed at the upper and lower limits of this region. The 148 keV singlet and the 203-208 keV multiplet

were used to determine $^{241}$Pu activity (Figure 53). The 208 keV photon peak in the multiplet is from the decay of $^{237}$U, the minor alpha branch of the $^{241}$Pu decay chain (47). The $^{241}$Am contribution to this peak signal is minimal (Table 18) and can be subtracted using the rest of the peaks in the multiplet. The 185 keV singlet was used to determine $^{235}$U (Figure 53).

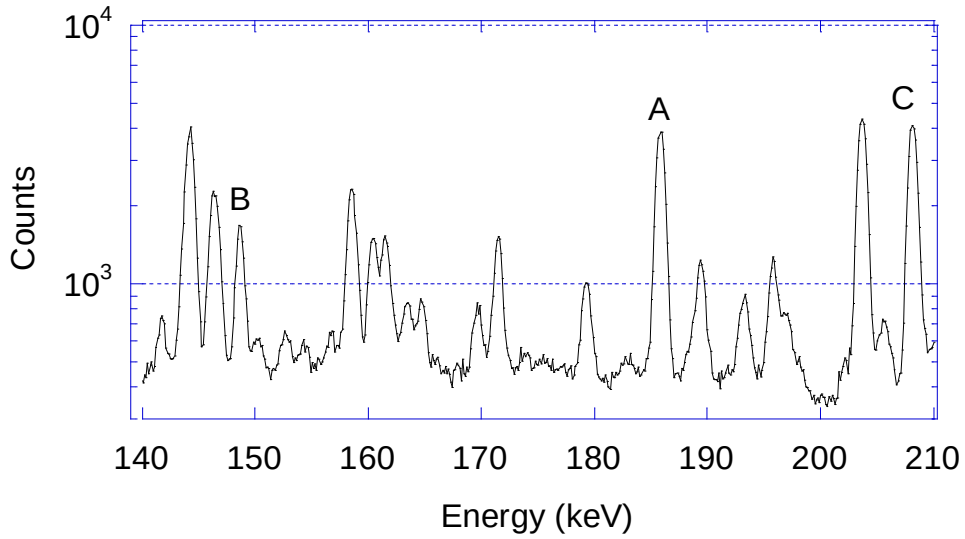


**Figure 53.** Example of a gamma spectrum of a hot particle in the 140-210 keV region. A-C are the peaks used for $^{235}$U, $^{241}$Pu and $^{237}$U analysis, respectively.

## 6.4 Results and Discussion

### 6.4.1. Qualification of Peak Fitting Analysis and Gamma System Calibration

The quality of the peak fitting analyses and the energy/efficiency calibration was evaluated by determining the ratio of the estimated peak area (48) to the observed peak area (EOPA) at both 203 keV and 336 keV (Figure 54). The estimated peak area was determined from the decay corrected weapon

composition data (11). The average EOPA values were 0.952 ± 0.057 and 0.947 ± 0.107 for the 203 and 336 keV peaks, respectively.

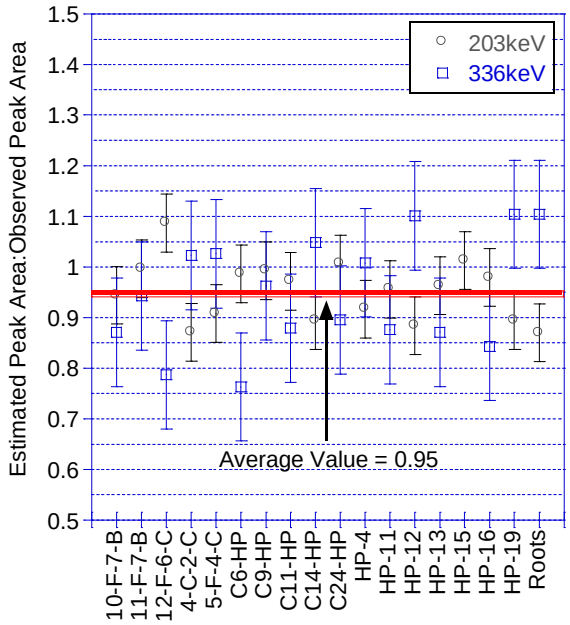


**Figure 54.** Determination of the quality of the peak fitting analysis and gamma system calibration using the EOPA for the 203 and 336 keV photon peaks.

The current gamma analysis protocol is fairly robust, but does underestimate the $^{239}$Pu and $^{241}$Am activities by 5%. The large degree of scatter across the particle population may be intrinsic to individual hot particles, a function of counting statistics, poor peak fitting, or a combination of these traits and others (e.g., a systematic problem with the nuclear data for one or both nuclides). These data can be used to define the characteristics of the population but an effort should be made to determine the source of these errors and minimize them.

### 6.4.2. $^{241}$Am:$^{239}$Pu Activity and Relative Ratio Analysis

The estimated $^{241}$Am and $^{239}$Pu activity and the relative ratios for each hot particle are provided (Table 19). The average $^{241}$Am:$^{239}$Pu ratio for the particle population was 0.22 ± 0.03, which was slightly lower than the expected value of 0.24 (14) but within one standard deviation. Over time, the majority of the $^{241}$Am has remained incorporated in the WGPu matrix.

In the soil studies (Chapter 4), $^{241}$Am was distributed throughout the soil column, with elevated activity directly above the hot particle location and in discrete spikes not associated with the hot particle. It is assumed that the localized spots of $^{241}$Am (and $^{239}$Pu) in the soil are smaller hot particles that were missed during initial core fractionation. Particle mobilization was not specifically studied, but the gamma analysis of the core and isolated particle suggest that the particles are subject to shear stress and mechanical transport. As the particle sheds material by either physical or chemical mechanisms, smaller particles (or colloids) may be preferentially passing through the macropores of the soil column (23,24).

### 6.4.3. $^{241}$Pu:$^{239}$Pu Relative Ratio Analysis and Age Dating

The $^{241}$Pu:$^{239}$Pu activity ratios are provided for the particle population (Figure 55). By direct measurement the $^{241}$Pu:$^{239}$Pu could be determined for n = 17 hot particles. The remaining particles had insufficient counts in the $^{241}$Pu peak due to low activity levels. The $^{241}$Pu:$^{239}$Pu activity ratios values ranged from 0.516 to 0.913, with an average ratio of 0.729 ± 0.079, which was within 1σ of the theoretical value of 0.74 (11).

**Table 19.** Evaluated $^{241}$Am and $^{239}$Pu activities and relative ratios for the particle population. The error associated with the reported values is ± 5% unless specified.

| Particle | $^{239}$Pu Activity (Bq) | $^{241}$Am Activity (Bq) | $^{241}$Am:$^{239}$Pu | Count Time (Sec) |
|---|---|---|---|---|
| **10-F-7-B** | 95908.0 | 18972.0 | 0.20 | 86,400 |
| **11-F-7-B** | 192067.0 | 50060.0 | 0.26 | 70,477 |
| **12-F-6-C** | 46603.0 | 11223.0 | 0.24 | 74,517 |
| **4-C-2-C** | 231227.0 | 66539.0 | 0.29 | 125,193 |
| **5-F-4-C** | 339435.0 | 76803.0 | 0.23 | 12,109 |
| **C6-HP** | 34047.0 | 7104.0 | 0.21 | 86,400 |
| **C9-HP** | 49637.0 | 10657.0 | 0.21 | 83,460 |
| **C11-HP** | 65119.0 | 14803.0 | 0.23 | 190,000 |
| **C14-HP** | 455494.0 | 95090.0 | 0.21 | 76,156 |
| **C24-HP** | 53306.0 | 10961.0 | 0.21 | 82,854 |
| **HP-2** | 2826.0 | 726.0 | 0.26 | 190,000 |
| **HP-4** | 211433.0 | 56342.0 | 0.27 | 129,734 |
| **HP-11** | 48865.0 | 9756.0 | 0.20 | 84,985 |
| **HP-12** | 178705.0 | 34418.0 | 0.19 | 86,400 |
| **HP-13** | 100899.0 | 21272.0 | 0.21 | 156,865 |
| **HP-14** | 4243.0 | 880.0 | 0.21 | 190,000 |
| **HP-15** | 13374.0 | 2671.0 | 0.20 | 86,400 |
| **HP-16** | 87726.0 | 19487.0 | 0.22 | 84,534 |
| **HP-19** | 134646.0 | 25678.0 | 0.19 | 86,400 |
| **Roots** | 240557.0 | 54478.0 | 0.23 | 161,328 |
| **Average 241Am:239Pu Activity Ratio** | | | 0.22 ± 0.03 | |

An alternative route for quantification of $^{241}$Pu activity is measurement of the 208 keV photon peak from $^{237}$U decay (Table 18). There is an interference from $^{241}$Am at this energy, but the yield is very low. The Am is estimated from the activity measured for the more dominant peak (i.e. 59.5 keV) and is yield and efficiency corrected to determine the contribution to the 208 keV peak. It is assumed that $^{237}$U is in secular equilibrium with $^{241}$Pu, therefore the activities are equivalent. The $^{241}$Pu:$^{239}$Pu ratio ranged from 0.501 to 0.875, with an average of

0.732 ± 0.090 for n = 18 particles. The value of this technique is that it provides an alternative ratio for age dating when $^{241}$Am is not completely separated from the Pu matrix during the manufacturing process (7). The estimated date of manufacture of the WGPu using the average $^{241}$Pu:$^{239}$Pu ratio of the particle population and the WGPu isotopic data (Table 1) is 1958 ± 3 years. The calculated date of manufacture is in good agreement with the literature (14).

In cases where the initial concentration of $^{241}$Pu is unknown, the $^{241}$Am:$^{241}$Pu ratio can be used to estimate the age of the Pu matrix. This works under the assumption that the Am remains incorporated with the Pu matrix and that the initial concentration of Am was negligible at the time of manufacture. The average $^{241}$Am:$^{241}$Pu ratio for the particle population was 0.31 ± 0.07, which correlates to a production date of 1959 ± 5 years. The population ratio of $^{241}$Am:$^{241}$Pu is within 1σ of the expected value of 0.33, but could possibly indicate depletion of Am in the WGPu matrix. This correlates with the trends observed for the $^{241}$Am:$^{239}$Pu analysis. The majority of the $^{241}$Am remains incorporated with the WGPu matrix. The loss of Am from the matrix needs to be identified. If the weapon was manufactured in 1958 and the BOMARC accident occurred in 1960, it is possible that the Am (0.003, relative to Pu in 1960) fractionated from the Pu matrix during the fire. This theory is discussed in greater detail in Chapter 8.

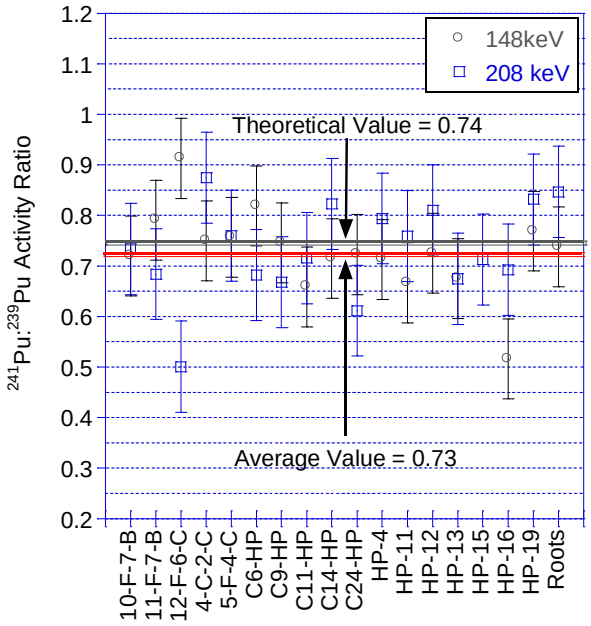


**Figure 55.** The $^{241}$Pu:$^{239}$Pu activity ratios for the hot particle population.

### 6.4.4. $^{235}$U:$^{239}$Pu Relative Ratio Analysis

The presence of $^{235}$U in the hot particles from the decay of $^{239}$Pu is expected to be minimal, i.e., the $^{235}$U:$^{239}$Pu atomic ratio is 0.0014 based on the decay corrected literature values (11). The observed atomic ratios of the particle population are presented (Figure 56). Most of the particles (n = 19) contained at least one order of magnitude more $^{235}$U than expected for a pure Pu matrix. This would indicate that a composite of HEU and WGPu was used in the weapon (49) and that the two matrices were in close proximity during the fire. Elemental analysis studies (Chapter 5) confirmed that a single hot particle can contain mixed Pu/U regions, as well as depleted regions containing only Pu or U. Forensic interpretation of the $^{235}$U:$^{239}$Pu ratio is provided in Chapter 8.

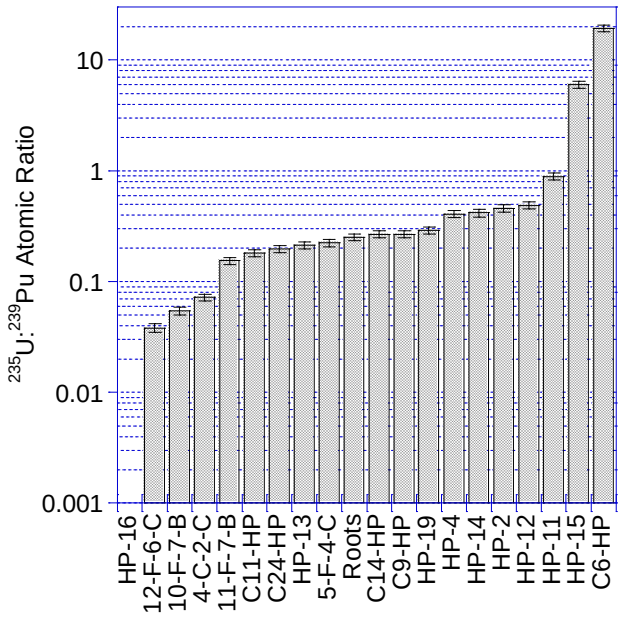


**Figure 56.** The $^{235}$U:$^{239}$Pu activity ratios for the particle population.

## 6.5 Conclusions

Conventional high resolution gamma spectroscopy is a useful tool for the non-destructive analysis of hot particles and should be utilized before any destructive techniques are employed. The advantages of this technique include no extensive sample preparation (other than the initial isolation of the hot particles from the soil matrix), analytical versatility (it can be performed before or after other non-destructive techniques), and it is commonly available and relatively inexpensive. In this work various activity ratios of the minor isotopic components of the WGPu matrix were determined for a population of particles. The heterogeneous nature of the particle population emphasizes the importance of obtaining intact particles versus homogenized soil samples.

The majority of the $^{241}$Am that has built in from the decay of $^{241}$Pu has remained with the plutonium matrix for the BOMARC particle population. The gamma analysis of the fractionated soil cores with the primary hot particles removed (Chapter 4) suggested that hot particles contribute Am and Pu to the near field environment, producing both heterogeneous, or particle-like, and homogenous distribution patterns. Combined, these data sets suggest that Am and Pu are both mobile in the environment and that transport mechanisms are similar. Evidence of the presence of micro-particles (Chapter 4) from gross alpha/beta analysis would suggest a mechanical transport mechanism, but further study will be required to confirm this.

From a forensic standpoint, gamma analysis of the particle population determined that $^{235}$U was present in the weapon as a separate component and has mixed with the Pu matrix most likely due to fire exposure. A more detailed discussion is provided in Chapter 8. In addition, the age of the WGPu matrix was determined using the $^{237}$U photon peak as a chronometer instead of $^{241}$Am, which can be present in significant concentrations in the original source matrix. The use of $^{237}$U is possible because of the high specific activity of the WGPu particles, the increased peak resolution of the detector, and the ability to analyze large data sets congruently.

# CHAPTER 7

# RADIOANALYTICAL CHARACTERIZATION OF HOT PARTICLES – ALPHA SPECTROSCOPY

## 7.1 Abstract

Weapons grade Pu (WGPu) hot particles were isolated from soil cores that were collected from the BOMARC site and were characterized using minimally destructive techniques. The advantage of this type of analysis is that the primary information associated with the particle remains intact throughout the analysis process. Non-destructive radioanalysis is usually performed with gamma spectroscopy for isotopic information and by gas-flow proportional counting for gross alpha-beta activity determination. In this chapter, alpha spectroscopy is used on the unprocessed particle to rapidly determine the $^{241}Am$ + $^{238}Pu$: $^{239+240}Pu$ ratio on the surface of the particles. The data obtained was in good agreement with the values presented in the literature for the BOMARC site. A comparison of surface measurements by alpha spectroscopy and bulk examination from gamma analysis (Chapter 6) is also provided.

## 7.2 Introduction

Alpha spectroscopy is a technique used to identify the energy and quantity of alpha particles emitted by the decay of radioactive material. In many cases the energies and ratios of the emitted alpha particles are unique to individual isotopes and can be used to identify and quantify the amount of a specific

isotope present in a sample. Alpha spectroscopy works by detecting the energy deposited when an alpha particle interacts with a thin silicon wafer.

Alpha analysis usually requires some form of chemical pre-treatment to ensure various matrix and radionuclide interferences are removed prior to analysis. The ideal alpha spectroscopy sample is one in which the material of interest is deposited in a monolayer on a uniform sample backing. A thin deposition layer allows alpha particles to escape from the volume of the sample with minimal attenuation, producing high resolution, full energy peaks for analysis. A variety of methods exist for producing samples for alpha analysis including electrodeposition (50,51) and $CeF_3$ precipitation (52,53). Both of these techniques require that the original sample be in an aqueous solution.

For solid debris analysis, all of the morphological and crystallographic information contained in the sample is lost upon complete dissolution. Since this information may be as valuable as the isotopic information contained within the sample, chemical dissolution of the solid debris should be one of the last steps in any suite of analytical methods. To determine if any useful data could be extracted from the hot particles via alpha spectroscopy prior to dissolution, 15 unaltered hot particles were analyzed by alpha spectroscopy. The results were compared to gamma data collected from the same particles.

## 7.3 Alpha Spectroscopy – Thin versus Thick Sources

Alpha spectra for a thin source (prepared by $CeF_3$ precipitation) and a thick source (hot particle) are provided (Figure 57). The hot particle spectrum is step

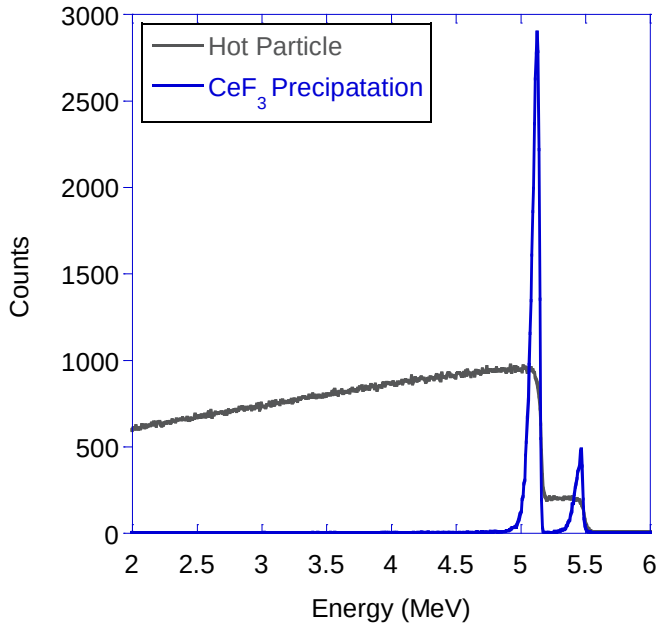


**Figure 57.** Thin and thick source alpha spectra. The thin source was prepared by $CeF_3$ precipitation after the hot particle was dissolved and has clearly defined peaks at 5.16 and 5.49 MeV alpha energies. The thick source is from an unprocessed hot particle and has two steps, which correspond to the primary alpha energies previously mentioned.

shaped and dominated by low energy tailing while the $CeF_3$ spectrum exhibits narrow, well-defined peaks with little tailing. The tailing observed in the hot particle spectrum is caused by the energy loss of alpha particles within the sample. Alpha particles produced on the surface of the particle can reach the detector at full energy and therefore produce the vertical lines on the leading edge of each step (5.157 and 5.486 MeV).

Alpha particles that escape from the volume of the particle will have a range of kinetic energies which produces the broad tail behind the leading edge of each dominant alpha energy peak. The narrow peaks in the $CeF_3$ sample can be used to identify specific alpha emissions and to quantify the isotopic content of a

sample through integration of the area under each peak and adjusting these data for detector efficiency and radiative yield values for the alpha particles of interest. A hot particle spectrum cannot be analyzed using this technique when more than one alpha emitting isotope is present because the alpha energies are spread across a continuum of values and cannot be individually integrated.

Thick source analysis has been conducted in the past on hot particles in small soil volumes for gross activity determination and as a pre-selection criterion (54). Direct alpha analysis has been performed on various hot particles originating from both the Chernobyl and Thule nuclear accidents (55,56). A series of Monte Carlo simulations were run for these particles and deconvolution analysis was attempted to determine isotopic information. The utility of alpha analysis was limited, but when used in conjunction with information from other non-destructive analysis techniques such as high resolution gamma spectrometry and scanning electron microscopy (SEM), WGPu isotopic information was validated without destroying the particle.

## 7.4 Advantages of Direct Alpha Analysis of Hot Particles

Gamma analysis and SEM coupled with energy dispersive spectroscopy (EDS) provide information about the volume and surface elemental composition, respectively. The limitations of gamma analysis are with the counting efficiency and low radiation yield of gamma rays from the Pu isotopes of interest (a more detailed discussion is presented in Chapter 4). In this work, gamma spectra were collected over a 24 hour period to allow for adequate counts in the peaks

associated with Pu decay. Analysis by SEM/EDS can be completed in a short period of time, but isotopic information is not achievable. Acquisition time for alpha analysis of the hot particles was 10 minutes, which provided sufficient counts to determine the $^{241}Am+^{238}Pu:^{239+240}Pu$ ratio. Under the auspices of a nuclear incident, early or rapid detection of the actinide matrix will be critical in the analysis chain of events.

## 7.5 Methods and Materials

### 7.5.1 Alpha Spectroscopy Measurements

Isolated hot particles were centered and fixed to 25 mm (diameter) steel planchets with carbon tape. The instrument used for the measurements was a Canberra Alpha Analyst system, and the data were acquired with Genie 2000 software. The samples were placed 16 mm from the surface of 450 $mm^2$ passivated implanted planar silicon (PIPS) detectors (Canberra A450-18AM) and counting was started when the chambers reached 1.5 torr (0.002 atm). All of the hot particles were counted for 600 seconds and data were acquired in 1024 channel spectra covering an energy range of 1.4 – 8.4 MeV.

### 7.5.2 Alpha Analysis of Unprocessed WGPu Hot Particles

The particles discussed in this work were on the order of 0.1 to 0.5 mm in diameter, much larger than those investigated in the literature (diameter ~10 μm) and, as with the Thule and Chernobyl accidents (55,56), most of the historical information (i.e. type of weapon, Pu isotopic composition, etc.) was known (Table 1). The alpha emitting isotopes that were expected to be present in the

hot particle sample are provided (Table 20) along with the peak energy and intensity information.

**Table 20.** Alpha decays from the hot particle matrix with intensities greater than 1% and the peak to which they contribute in an alpha spectrum.

| Low Energy Step (< 5.168 MeV) | | | High Energy Step (> 5.168 MeV) | | |
|---|---|---|---|---|---|
| **Energy (MeV)** | **Intensity (%)** | **Isotope** | **Energy (MeV)** | **Intensity (%)** | **Isotope** |
| **5.106** | 11.94 | $^{239}$Pu | **5.388** | 1.66 | $^{241}$Am |
| **5.124** | 27.10 | $^{240}$Pu | **5.443** | 13.10 | $^{241}$Am |
| **5.144** | 17.11 | $^{239}$Pu | **5.456** | 28.98 | $^{238}$Pu |
| **5.157** | 70.77 | $^{239}$Pu | **5.486** | 84.80 | $^{241}$Am |
| **5.168** | 72.80 | $^{240}$Pu | **5.499** | 70.91 | $^{238}$Pu |

The $^{241}$Am is included because it becomes a major contributor to the alpha activity of the WGPu matrix as the material ages. Other Pu isotopes are not included for alpha analysis because of low alpha yields ($^{241}$Pu) or trace concentrations in the WGPu matrix ($^{242}$Pu). Daughter products of the primary constituents (Table 20) will also be present in older materials but their contributions to the total alpha emissions are less than 0.1% of total activity and are not discussed in this work.

Using the data provided (Table 20), the high energy step (Figure 58) is the combination of signals from $^{238}$Pu and $^{241}$Am and the low energy step is the combined signal for $^{238,\ 239,\ 240}$Pu and $^{241}$Am. The ratio of $^{238}$Pu+$^{241}$Am:$^{239,\ 240}$Pu can be calculated using the following relationship:

$$\frac{^{238}Pu + {}^{241}Am}{^{239}Pu + {}^{240}Pu} = \frac{B}{A - B} \qquad \text{Equation 3}$$

where A and B are the count signals integrated over a defined area with the high and low energy limits set in regions where the signal is stable (shaded region, Figure 58). Both areas A and B have the same energy/channel width.

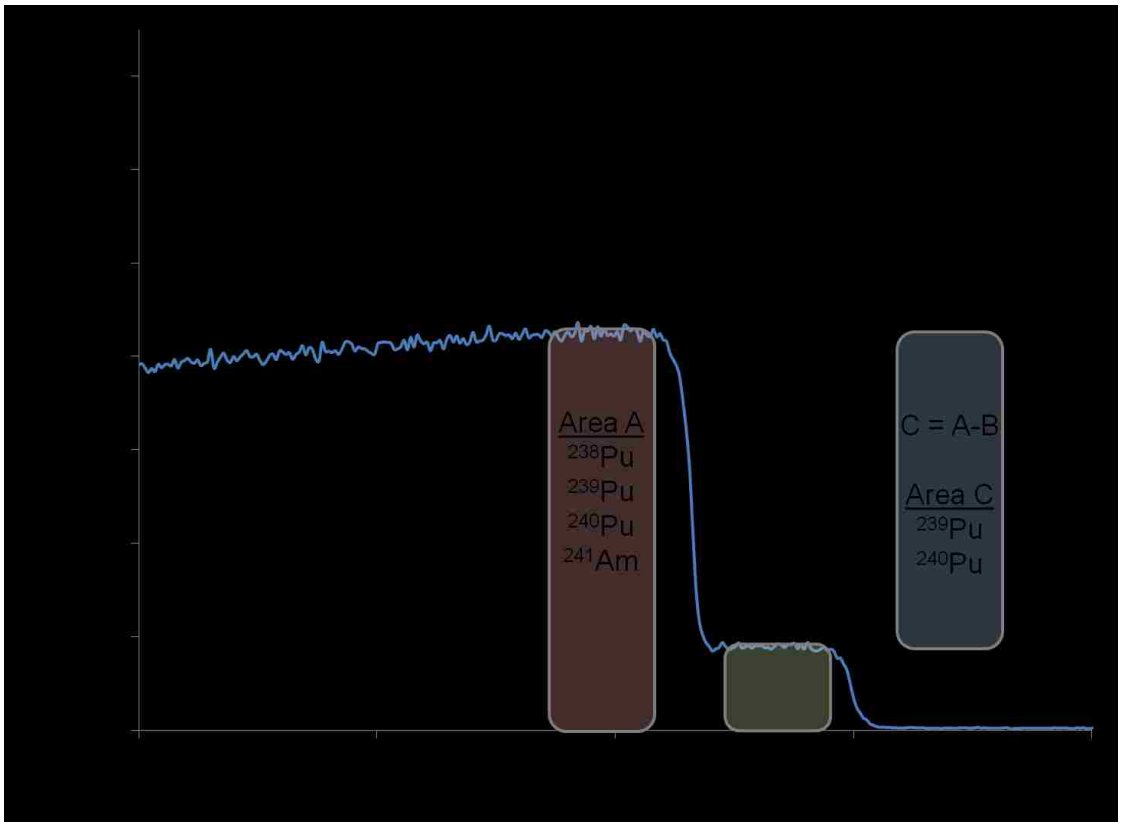


**Figure 58.** Major features of the hot particle alpha spectra and its isotopic contributions. Areas A-C were used to determine the 238Pu+241Am: 239, 240Pu activity ratio.

The $^{238}$Pu and $^{241}$Am contribution to Area A is subtracted producing Area C, the $^{239,240}$Pu signal (Figure 58). With the $^{239,240}$Pu signal resolved, the $^{238}$Pu+$^{241}$Am: $^{239,240}$Pu activity ratio can be calculated. This procedure relies on three assumptions. The first is that there is symmetry in the tailing behavior of

the high and low energy steps, if the lower energy alpha particles ($^{239,240}$Pu) do not exhibit a rapid drop off in signal, it is unlikely that the higher energy alpha particles ($^{238}$Pu and $^{241}$Am) will behave differently. The second assumption is that symmetrical regions of stable signal can be found on both the low and high energy steps (Area A and Area B in Figure 58). The third assumption is that the area of the high energy signal is much smaller than that of the low energy signal. When the magnitude of the high energy signal approaches that of the low energy signal, the error associated with fitting a step function to the data will increase due to the uncertainty of the contribution of the high energy tail to the lower energy step. These assumptions work for a WGPu matrix because the ratio of $^{238}$Pu+$^{241}$Am:$^{239+240}$Pu will always be small and produce a step shaped spectrum.

## 7.6 Results and Discussion

The results of this analytical technique applied to 15 hot particles are provided (Figure 59). The grey box in the center of the graph outlines the area covered by the standard deviation of the average, and the counting error for individual particles is smaller than the area covered by the data marker. The $^{241}$Am+$^{238}$Pu:$^{240,239}$Pu activity ratio for the particle population ranged from 0.137-0.244, with a mean activity ratio of 0.196 ($1\sigma$ = 0.030). This value is in good agreement with the published mean activity ratio of 0.19, based on the $^{241}$Am:$^{239,240}$Pu ratio determined by chemical separation and electroplating (11, 19).

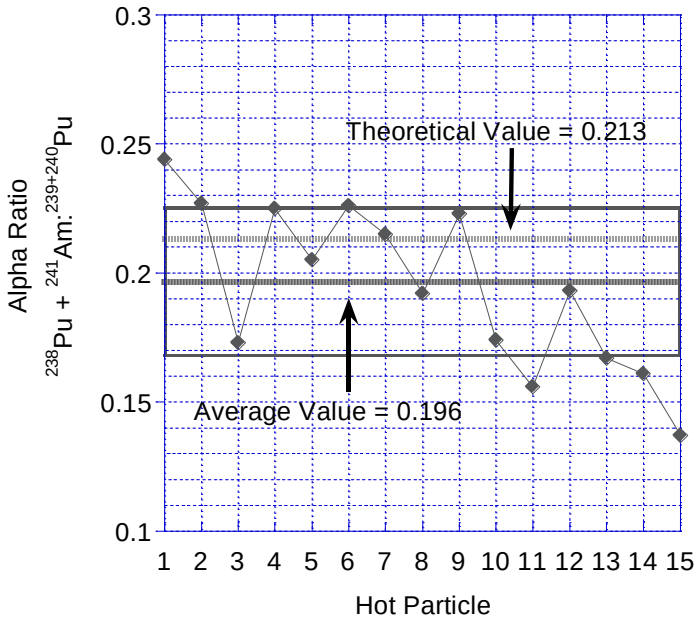


**Figure 59.** The $^{238}$Pu,$^{241}$Am:$^{239+240}$Pu ratios determined by alpha spectroscopy for each unprocessed hot particle. The count time was 10 minutes/particle.

Although the ratio determined in this study incorporates $^{238}$Pu, the total alpha activity contribution is less than 1.3%, and is only 7.5% of the combined $^{241}$Am, $^{238}$Pu activity based on a 51 year decay period and the isotopic information provided by LANL (14). In former studies, the activity ratios were highly variable (0.15-0.24) across individual samples (19) and the average was less than the expected activity ratio of 0.213 (14) but still within 1σ of the value. These findings were consistent with the hot particle data set. The combined data sets suggest that the shifts in the activity ratios are driven by the heterogeneous distribution of the Am in the particle matrix.

### 7.6.1 Comparison of Gamma and Alpha Spectroscopy of Hot Particles

The utility of alpha spectroscopy as a rapid analysis method for unprocessed WGPu particles is evident when compared to high resolution gamma spectroscopy data of the same particle population. Alpha spectra were collected in 10 minutes versus the 24 hour count time required to obtain the $^{241}Am$:$^{239}Pu$ activity ratio by gamma spectroscopy (Chapter 6). The direct comparison of the alpha activity ratio ($^{238}Pu$+$^{241}Am$:$^{239+240}Pu$) to the gamma activity ratio ($^{241}Am$:$^{239}Pu$) can be made for qualitative purposes. The contributions of the $^{238}Pu$ and $^{240}Pu$ to the alpha activity ratio cannot be isolated from the $^{241}Am$ and $^{239}Pu$ signals, respectively. Therefore, the alpha ratio should be approximately 11.2% lower than the gamma ratio (14).

The activity ratios determined by both alpha and gamma analysis are presented (Figure 60). The $^{241}Am$:$^{239}Pu$ activity ratio determined by gamma spectroscopy ranged from 0.191 to 0.261, with an average value of 0.223 ($1\sigma$ = 0.028). Similar to the alpha data, the average ratio is below the expected value of 0.24 predicted by the decay corrected LANL data (14), but within $1\sigma$. When the average alpha ratio is compared to the average gamma ratio, the alpha ratio is 12.1% lower than the gamma ratio and is in good agreement with the theoretical value previously discussed. Variations observed in the isotopic activity ratios by alpha spectroscopy correlate with those present in the gamma data. This indicates that the variations in the isotopic ratios are not statistical phenomena but are real signals and that the depletion of $^{241}Am$ is across the volume of the particle, not a surface phenomenon. This is also supported by

elemental mapping experiments of the hot particle population (Chapter 5) and may provide further insight into the formation conditions of the hot particles (Chapter 8).

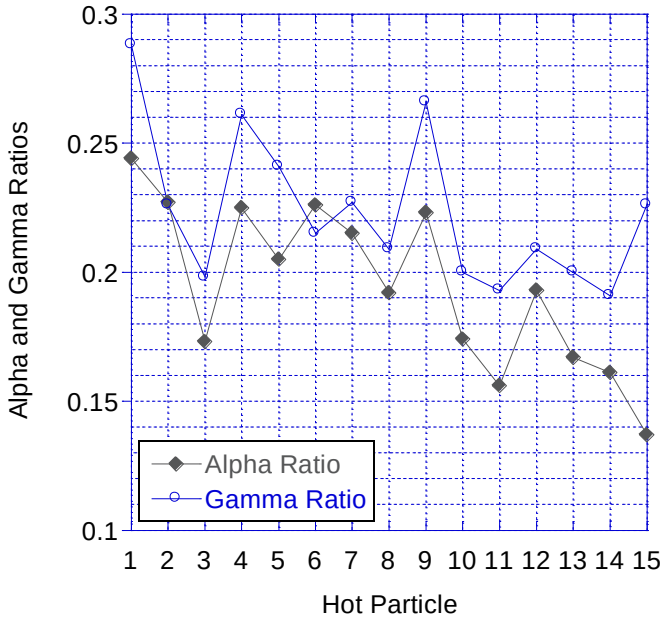


**Figure 60**. The $^{241}$Am:$^{239}$Pu activity ratios by gamma and alpha spectroscopy are shown for individual hot particles.

Another approach is to evaluate the average difference in the observed gamma and alpha activity ratios (Figure 61, Equation 4):

$$R_{gamma} - R_{alpha} = \frac{^{241}Am}{^{239}Pu} - \frac{^{238}Pu + {}^{241}Am}{^{239}Pu + {}^{240}Pu} \qquad \text{Equation 4}$$

A positive difference value indicates that the surface concentration of $^{241}$Am is lower than the bulk concentration. A negative difference means that there is less Am distributed throughout the particle volume. This relationship is governed by the differences in depth penetration for gamma and alpha radiations. The

gamma ratio is unaffected by the particle dimensions, while the alpha ratio is only relevant to the surface layers of the matrix. The average difference in the observed gamma and alpha ratios is 0.029 ± 0.022, which is higher than the expected average difference of 0.027 but within error. The majority of the particles are clustered within the 1σ region; however, several particles have greater differences in alpha and gamma ratios. The cause of fractionation of Am from the particle matrix is difficult to determine. It is possible that Am is preferentially removed from the Pu matrix by environmental conditions, but no evidence of this has been reported for these materials. The heterogeneity of the ratio distributions would be expected to favor surface depletion of Am, or a positive difference value, if environmental fractionation was the primary influence. There is only one particle that exhibits a positive difference value greater than 1σ from the population value.

Evaluation of the soils surrounding the hot particles by gamma spectroscopy and gross alpha/beta analysis (Chapter 4) have shown that hot particles contribute $^{241}$Am and Pu to the near field environment, producing both heterogeneous, or particle-like, and homogenous distribution patterns. The analyses provided in this study support heterogeneous distribution (mechanical); however, a larger population of particles must be evaluated. If it is assumed that the original WGPu matrix at the time of the accident was Pu metal, then it is possible that the Am depleted particles formed as a result of the accident. A more detailed discussion of this premise is provided in Chapter 8.

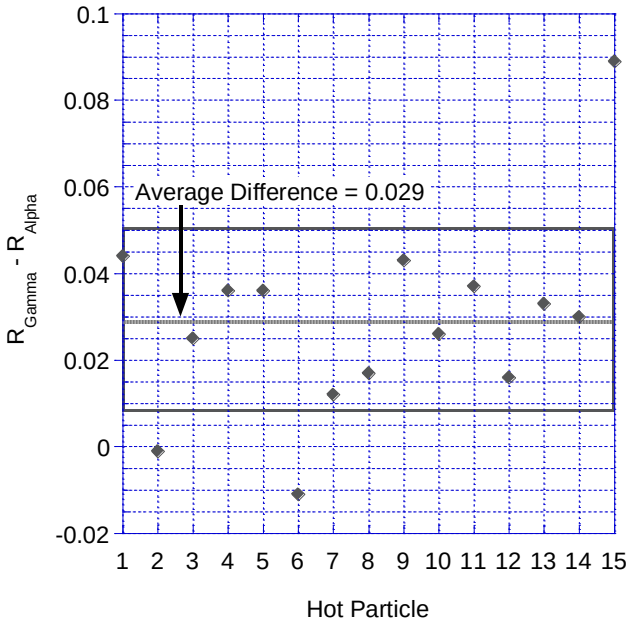


**Figure 61**. The difference in the gamma and alpha ratios, $R_{gamma}$ and $R_{alpha}$ across the hot particle population. The boxed region indicates the 1σ boundary.

## 7.7 Conclusions

Direct alpha spectroscopy of hot particles utilizing the analysis method previously outlined can be used to rapidly determine the $^{238}Pu$+$^{241}Am$:$^{239,240}Pu$ ratio. These values are in good agreement with those reported in the literature for the BOMARC site (11,19). Combining hot particle alpha spectroscopy and gamma spectroscopy data provides a non-destructive method to verify shifts in the $^{241}Am$ concentrations in individual particles that might otherwise be categorized as normal statistical variations using only one of the techniques. It has been shown through analysis of the combined gamma spectroscopy and alpha spectroscopy data sets that the variation in the $^{241}Am$ concentrations found in individual particles was most likely produced by the fractionation of $^{241}Am$

during combustion of the weapon. The $^{241}$Am concentration is lower than expected in the population of hot particles when compared to theoretical values indicating that either the reported $^{241}$Pu concentration in the WGPu matrix is low or $^{241}$Am has been selectively removed. The selective removal of $^{241}$Am is the best explanation for the depressed $^{241}$Am concentrations based on direct comparison of the $^{241}$Am to $^{239}$Pu ratios as measured by alpha and gamma spectroscopy. This stems from the comparison of surface measurements by alpha spectroscopy and bulk examination from gamma analysis.

# CHAPTER 8

# SOURCE TERM CHARACTERIZATION

## 8.1 Interpretation of the Combined Data Sets

The combined gamma, alpha, EDS and elemental mapping data provide information about the composition of the energetic materials, the configuration of the warhead and the conditions that formed the hot particles. Presented below is an overview of the data, excluding the relative plutonium isotopic ratios, that is useful in determining the warhead configuration and conditions that formed the hot particles.

- Gamma and alpha spectroscopy data for 15 particles
  - $^{241}$Am:$^{239}$Pu ratio is variable
  - $^{235}$U:$^{239}$Pu ratio is variable
- EDS analysis of U/Pu distribution for 15 particles
  - U:Pu ratio was not homogenous across the population of particles
  - U:Pu ratio was not homogenous across individual particles
  - Most particles contained a mixture of U and Pu, some surface regions consisted of pure Pu or U
- EDS analysis of minor components for 15 particles
  - Si, O observed in all particles
  - Al observed in 14 of 15 particles
  - Fe observed in 13 of 15 particles
  - Ti observed in 12 of 15 particles
  - Ga observed in 5 of 15 particles

- Nb observed in 4 of 15 particles
- Ni and Cr observed in 3 of 15 particles

- SEM imaging
  - Each hot particle has a different shape, size and surface texture
  - The surface texture of individual hot particles is not uniform over the entire particle
- Elemental Mapping observations
  - Patterns indicating mixing of U and Pu were observed
  - Patterns indicating layering of U and Pu were observed
  - Segregation of Ga from the Pu matrix was observed
  - Non-homogenous Am distribution was observed

There are at least two ways to interpret this data set. The first to be presented is without reference to the historical narrative associated with the warhead and accident. This interpretation of the data would be representative of a forensic scenario; an unknown material needs to be analyzed with little or no information available about its point of origin and limited information available about its recent history. What is noticeably absent from the first discussion is the use of the Pu age data as a reference point. A detailed discussion of why these data may not be useful or even be misleading will be presented in the second interpretation of the data set. The second interpretation of these data involves coupling the analysis to the historical narrative associated with the accident and the U.S. weapons production data from 1955-1960.

## 8.2 First Interpretation – Analysis without the Historical Narrative

Without reference to the background material and historical documents associated with the accident, several general conclusions about the warhead configuration can be made. The presence of enriched $^{235}U$ in the hot particles (19 out of 20) at concentrations (0-92 at% $^{235}U$) several orders of magnitude greater than what would be expected from the decay of $^{239}Pu$ supports the theory that the material did not originate from a pure Pu matrix but rather from a composite highly enriched U, WGPu design (49). The EDS data show that a single hot particle can contain regions with a mixed U/Pu matrix, a pure Pu matrix and a pure U matrix. Elemental maps of two of the hot particles show both mixing and isolated layering of U and Pu. Combined, the EDS and elemental mapping data show that U and Pu were in close contact at the time of the accident, making a strong case for a composite core design.

There are two likely candidates for the arrangement of the U and Pu within a composite core, a U/Pu alloy or separate U and Pu metal components in close contact. The presence of Ga, indicated by both the EDS and elemental mapping data, eliminates the U/Pu alloy as a candidate for the composite core material. Gallium at low concentrations (1-2 wt%, 3.4-6.5 at%) is used to stabilize the Pu in the δ-phase and is used in most weapons because of its desirable mechanical characteristics (38,49,57). Uranium has limited solubility, 0.3 atom % U, in δ-Pu (38,58). It is unlikely that a U/Pu alloy could be fabricated with δ-Pu that could contain the 2-92 atom % $^{235}U$, which was found in 19 of the 20 hot particles.

A third, but unlikely candidate material for use in a composite core would be a solid $UO_2$-$PuO_2$ matrix. From a chemical stability standpoint the $UO_2$-$PuO_2$ system would be a good choice of material because it is more chemically and thermally stable when compared to Pu or U metal (59,60,61) and can be formed into solid solutions from pure $UO_2$ to pure $PuO_2$, provided the stoichiometry of the system is controlled during fabrication (59). The negative aspects of these materials are low densities, 10.95 g/cm$^3$ (62) for $UO_2$ and 11.46 g/cm$^3$ (63) for $PuO_2$, and the 60-67 at% of oxygen incorporated into the lattice (59). Because of the low densities of these oxides and the presence of diluting oxygen atoms, a warhead designed around this material will require a larger mass and larger volume of material to achieve criticality relative to a metal in the same configuration (Table 21). The larger mass of metal oxide required for criticality and corresponding larger volume of material would require a larger and heavier package to contain the device reducing its desirability as a weapons material.

**Table 21.** Comparison of the physical characteristics of U and Pu metals and metal oxides required to achieve a critical mass.

| Material (Ref) | Isotopic Content | Density (g/cm$^3$) | Critical Mass (kg) Unreflected Sphere | Estimated Radius (cm) |
|---|---|---|---|---|
| **$UO_2$ (64)** | 94 wt% $^{235}$U | 10.95 | 110 | 13.4 |
| **U (49)** | 93.2 wt% $^{235}$U | 18.8 | 52 | 8.71 |
| **$PuO_2$ (64)** | Not Reported | 11.46 | 35 | 9.00 |
| **δPu (49)** | 4.5wt% $^{240}$Pu, 1 wt% Ga | 15.8 | 16.5 | 6.29 |

The combined gamma and alpha spectroscopy, EDS and elemental mapping data cannot conclusively eliminate a mixed $UO_2$-$PuO_2$ solid solution as the source term for the particles, but using the same argument based on the presence of Ga in the particles, it is unlikely that a mixed $UO_2$-$PuO_2$ system would be fabricated with Ga incorporated into the matrix.

Working under the assumption that the particles originated from a composite core material that consisted of a U metal component and δ-Pu metal component, the mixing of U and Pu that is observed in the hot particles provides some insight into the process that may have formed them. The most likely explanation for the U and Pu distribution patterns observed in the particles is mixing of melted U and δ-Pu components. Melting of either metal component would imply that the weapon had to have been exposed to high temperatures.

The spotty distribution pattern of Ga in the hot particles observed by EDS (5 of 15 particles) and the Ga inclusions present in the elemental maps are also indicative of heating the Ga-stabilized δ-Pu to the liquid phase and then slowly cooling the material producing both Ga-poor and Ga-rich phases within the Pu metal (63). Heating followed by slow cooling of Pu metal is also supported by the cracked, flaking layers observed on the surface of the hot particles by SEM imaging. Plutonium metal is prone to producing this type of cracking and splitting behavior because of the stresses induced by large volume shifts that accompany phase transitions between 0 ºC and 600 ºC (65).

The presence of Ga in the particles also provides an upper bound for the temperatures reached during the heating cycle. Although elemental Ga has the

unusually low melting point of 29.767 ºC (35) , its boiling point is 2204 ºC (35). Gallium in the presence of stoichiometric quantities of $O_2$ will form $Ga_2O_3$ which has only a slightly higher boiling point of 2420 ºC (66). The presence of Ga metal or $Ga_2O_3$ trapped in the particles indicates that the hot particle matrix did not exceed 2420 ºC for an extended period of time. In particles where no Ga was detected by EDS it is difficult to say if the temperature of the particle exceeded 2420 ºC; Ga may still be present, but at concentrations not detectable by EDS.

The Am present in the particles can also be used to identify the maximum temperature experienced by the material during heating and as an indicator of the amount of $O_2$ present during the heating cycle. Americium metal has a calculated boiling point of 2067 ºC (67), while the oxide of Am formed during combustion in air, $AmO_2$ (67) has a melting point estimated between 2100 ºC and 2200 ºC (68). If the Pu matrix is heated above 2067 ºC, without $O_2$ present the Am would be expected to boil off depressing the $^{241}$Am:$^{239}$Pu ratio in the hot particle. This phenomena has been observed with combustion of Pu metal and shown to reduce the Am:Pu ratio in large particles (>20 μm) while increasing the Am:Pu ratio in small particles (<3 μm) due to the re-condensation of vaporized Am (69). In the presence of excess $O_2$ and at temperatures below 2067 ºC the Am oxide (m.p. 2100 ºC – 2200 ºC) would be expected to form. Rather than boil off like the Am metal, the Am oxide would remain with the Pu matrix and produce particles with consistent $^{241}$Am:$^{239}$Pu ratios.

Shifts in the $^{241}$Am:$^{239}$Pu ratios are observed for individual hot particles by gamma and alpha spectroscopy, indicating that these particles were not formed

under or exposed to uniform conditions. Elemental maps of 4 of the 5 hot particles show Am homogenously distributed within the Pu matrix, while one hot particle exhibited a heterogeneous Am distribution, indicating that fractionation of Am did occur. Assuming that the original matrix was Pu metal, the population data for the $^{241}$Am:$^{239}$Pu ratio, combined with the elemental mapping data, indicates that some particles were formed under conditions that would permit Am to fractionate from the Pu matrix. The most likely explanation of this behavior is that some of the Pu matrix melted prior to oxidation, boiling off the Am and producing particles with low $^{241}$Am concentrations. Pu metal at temperatures below 2067 ºC may have acted as $^{241}$Am sink, condensing the vaporized $^{241}$Am and elevating the $^{241}$Am:$^{239}$Pu ratio. Although the particle size dependence is not observed, this type of behavior has been reported in (69). This mechanism has a lower temperature limit of 2067 ºC, the same temperature range as the boiling point of Ga.

To make full use of the Ga and Am signatures within the hot particles, one critical set of data is missing: detailed information about the crystal structure of the solids that contain both Ga and Am. Oxidation state, coordination number, oxygen ratios and bond lengths, information that can be determined from both XANES and XAFS experiments (70,71), would allow for identification of the final chemical states of both Am and Ga in the matrix. With this information it would be possible to better answer questions about whether the source term material was a metal or an oxide, as well as describe the conditions that formed the particles such as oxygen concentrations and combustion temperatures. In both

cases XANES and XAFS experiments should be added to complete this data set.

Qualitative analysis of the particles by EDS for matrix constituents besides U and Pu indicates that all of the particles contained Si and O, and most of the particles contained Al, Fe and Ti. A combined Ni and Cr signal was detected in 3 of 15 particles and Nb was detected in 4 of 15 particles. It is important to remember that these EDS analyses were performed to determine the distributions of U and Pu, so no effort was made to quantitatively analyze the relative concentrations of these minor components. For reference, a general theoretical limit of detection by EDS is about 0.08 wt % (72), but will be dependent on the EDS system, the specific element being targeted and the matrix that contains it.

Identification of the sources of Al, Si and Fe in the hot particles is of questionable value because it is difficult to determine whether these elements were incorporated into the original hot particle matrix or if these elements were introduced via environmental exposure because they are common to the soil from which the particles were removed (21,73). Separation of Si and Fe from the matrix and analysis of the isotopic composition of these elements by mass spectroscopy may provide more insight into their point of origin (i.e. Si has 3 stable isotopes, Fe has 4). The presence of Ti, Nb, Ni and Cr in the hot particles cannot be easily explained by using an environmental contamination argument. Although no detailed data are available on the concentrations of Ti, Nb, Ni and Cr in the soil that contained the hot particles, the average concentration of these

metals in the earth's crust is 1 to 3 orders of magnitude less than that of Fe (74), making observation by EDS of these elements at natural concentrations unlikely.

The identification of Nb in the hot particle matrix is especially interesting because 6 wt % Nb can be alloyed with U to produce a U metal alloy that is less prone to oxidation then a pure U metal (75,76). The presence of Nb with U would indicate that the U in the hot particle was manufactured with the intent of stabilizing it against oxidation for long term storage. This infers that the U found in the hot particle was not initially fabricated for or by those working with improvised materials for immediate use.

The Ni and Cr present in the matrix, when coupled with Fe or Ti, could be the remnants of stainless steel or nickel alloy components. Nickel may be present in the matrix because it is known to be used to plate finished Pu assemblies in an effort to control the spread of alpha (Pu) contamination during handling (77). No information specific to the use of Ti in a Pu matrix was identified, but Ti is commonly used in applications requiring high strength, light weight components or as an alloying agent with Fe or Ni. The results of the analysis without reference to the historical narrative are summarized below.

- The original phase of the Pu present in these particles was most likely Ga stabilized δPu
- The U present in the particles may have been alloyed with Nb
- The use of U and Pu alloys designed to be chemically stable over long periods of time indicates that this material was designed for long term stability

- The U and Pu were fabricated as a composite material, consisting of separate but closely associated U and Pu components
- The presence of the Pu and U alloys combined with a composite construction indicates that this material was produced using sophisticated manufacturing techniques
- The presence of significant quantities of $^{235}U$ with the Pu matrix indicates that the design of a warhead based on this material most likely consisted of a Pu trigger coupled to a U fuel
- The Am and Ga distributions indicate that the hot particles are a product of heating and oxidation with temperatures in excess of 2000 $^{0}C$
- Titanium, Ni and Cr are present in some of the hot particles above environmental concentrations indicating they may have been used in components that were in intimate contact with the Pu and U

## 8.3 Second Interpretation – Analysis with the Historical Narrative

As shown above, analysis of an unknown material outside of any historical context or background information limits the depth of analysis that can be performed. If the preceding data set is taken with the historical context then a much more detailed description of the warhead can be produced. A summary of the facts and observations taken from the historical record that are relevant to the analysis of the hot particles are given.

- The source of the Pu and U was a U.S. warhead mounted to a BOMARC missile (8)

- The warhead was destroyed on June-7-1960 (8)
- The Pu used was produced in 1958 (estimated) (14)
- The warhead was destroyed by the combustion of the high explosive charge contained within the weapon, not by the missile fire (9)
- The high explosive surrounding the warhead was completely consumed by the fire (9)
- The high explosive used in the warhead was Cyclotol (78)
- Oralloy, enriched $^{235}U$ was present in the warhead (9)
- The Pu and U components in the warhead melted through the casing (9)
- Pieces of slag, tentatively identified as Al, were co-located with the melted Pu and U on the floor of the missile shelter (9)
- An intact tritium bottle attached to the warhead assembly was recovered (8)
- The total length of the warhead assembly is estimated to be 30-90 cm from a series of redacted photographs from the accident site (8)

The most obvious and extremely useful pieces of information are the identification of the material as the product of a U.S. warhead accident that occurred in 1960. This information provides an upper bound for the date of manufacture of the device, and more importantly it identifies the material as a product of weapon-manufacturing activities in the U.S. With this knowledge, consideration of all other potential sources for this material can be removed from the discussion and the focus can be squarely placed on U.S. manufacturing techniques and warhead designs used through 1960.

Considering the warhead design, the presence of the tritium bottle identifies this as either a fission-fusion or tritium boosted-fission device. The fact that all of the hot particles collected were either pure Pu or contained a mixture of Pu and U (Oralloy) indicates that this was most likely a tritium boosted fission device (49). The arrangement of Pu and U in this type of device typically consisted of two, hollow subcritical shells into which a deuterium-tritium gas mixture would be injected (49) and then the whole assembly would be imploded using a high explosive charge.

The report that the tritium bottle was recovered intact and attached to the warhead assembly also gives a great deal of insight into the heating conditions to which the warhead was exposed during the missile fire. Data from a B53 bomb, a weapon that utilized a tritium bottle that was designed during the same period, indicates that the tritium bottles were actuated using a small explosive charge that consisted of 25 mg of lead styphnate and 175 mg of ball powder (79). The lead styphnate is of interest because it has a detonation temperature of 275 ºC (80). Assuming that the tritium bottle for this warhead and the B53 were of similar design, and that the tritium bottle was located within 90 cm of the Pu and U assembly, the fact that the tritium bottle was recovered without the explosive charge being fired indicates that the region surrounding the warhead was not subject to temperatures exceeding 275 ºC for an extended period of time.

A temperature of 275 Cº will have little effect on the Pu or U components contained within the warhead (58,81,82) but the same cannot be said for the

high explosive charge surrounding the Pu and U shells. Cyclotol, a mixture of RDX and TNT, typically in ratios of 50:50 or 75:25, was used as the high explosive charge in this warhead (78,83). RDX has a melting point of 204 ºC and a deflagration point of 230 ºC, TNT has a melting point of 81 ºC and a deflagration point of 300 Cº (84). The deflagration point of an explosive is the temperature at which a small sample of the explosive, without additional $O_2$, bursts into flame, decomposes rapidly or detonates (83).

The warhead must have experienced temperatures in excess of 204 ºC to ignite the RDX, but below 275 ºC to prevent the detonation of the lead styphnate charge in the tritium bottle. Once ignited, the flame temperature of RDX under 1 atm pressure is reported to be between 2430 ºC and 2830 ºC (85) and fits well with the minimum temperature of 2000 ºC based on the Am and Ga distributions presented in the first data interpretation. The combustion products of RDX consist of $H_2$, $H_2O$, $N_2$, CO, NO and $CO_2$ (85) and indicate that there is a negative oxygen balance during combustion when no additional $O_2$ is available (85). The TNT component of Cyclotol also exhibits a negative oxygen balance during combustion (83). Once ignited, the Cyclotol would produce temperatures capable of melting both the U and Pu components (81,82) potentially mixing the two (58) under $O_2$-poor conditions. To further complicate matters, both Pu and U metals are known to oxidize upon heating under atmospheric conditions, with Pu capable of exhibiting a self-sustaining reaction in bulk metallic pieces (60,61,69,86,87,88). Even though the specific mechanism of heating and combustion will never be known, the products of Pu and U combusted under

these conditions could be a combination of pure or mixed metals in a variety of oxidation states.

Though few data are available on the combustion products of Pu and U metals in the presence of an organic based fuel, the Vixen A trials (89) carried out by the British at the Maralinga test site in Australia could be representative of the conditions of the BOMARC accident. To determine the respirable release fraction of Pu in a fire, 200 g cylinders of Pu metal were burned outdoors in a petrol fire (89). Although the data from these tests are not available, it may be useful in the future to compare any data about particle morphology and composition from the Vixen A trials to the BOMARC data set.

Combustion of Pu metal in the form of bulk metallic pieces in a flowing air column has been performed (61) and, although the intent of these experiments was to study the release of respirable Pu oxide particulates by the combustion of Pu metal, there are several observations in these studies that match the description of the BOMARC accident site. In the experiments the author observes that after ignition the oxide layer would crack and sometimes the entire mass of the sample would collapse, releasing molten Pu (61). At the BOMARC site, a melted mass of U and Pu was reported below the warhead support (9) and the cracked oxide layer observed by the author (61) may have served as the source of the particles identified at the BOMARC site. Unfortunately no particle size distribution data for particles formed above the respirable fraction (>10 μm) was reported, but the formation of particles up to 200 μm was acknowledged (61). The core temperature of the metal at ignition was reported to be between

375-520 ºC and at the time of Pu liquefaction, the core temperature of the metal was reported between 800-1000 ºC (61).

When these data are combined a much clearer picture of the accident conditions can be created. Ignition of the high explosive charge initiated the combustion of the U and Pu components at temperatures above 2400 ºC, under potentially $O_2$-poor conditions. Once ignited the Pu had to remain above 800 ºC to produce the Pu slag located on the floor of the shelter. These high temperature conditions would explain why the Am and Ga distributions found in the hot particles are not uniform, why the isotopic ratio of $^{241}$Am to $^{239}$Pu is variable from particle to particle and why the average $^{241}$Am:$^{239}$Pu ratio for the population of hot particles is below the theoretical $^{241}$Am:$^{239}$Pu ratio based on a production date of 1958 (14) matching the trend reported in (69).

Particles with homogenous Am distributions, no Ga and small $^{241}$Am:$^{239}$Pu ratios would be indicative of material that was exposed to high temperatures (> 2200 ºC) long enough for both the Am and Ga to boil out of the Pu matrix prior to oxidation. Material exposed to the mid-temperature range, below 2200 ºC but above 640 ºC (90), between the boiling point of Ga and the melting point of the Pu matrix, would exhibit heterogeneous Am and Ga distributions. Particles from this material would be the most likely to exhibit elevated $^{241}$Am:$^{239}$Pu ratios because of their proximity to the high temperature regions and their ability to act as condensation points for Am escaping from material exposed to high temperatures. Particles with homogenous Am and Ga distributions along with $^{241}$Am:$^{239}$Pu ratios that match the theoretical value would have experienced low

temperature conditions, <640 ºC (90) maintaining the Am and Ga in the Pu matrix while only undergoing oxidation.

Formation of an oxide layer followed by cracking during combustion of the Pu and U was the most likely source of the particles collected on the site. Imaging of the surfaces of the particles revealed that many of them have highly cracked and fractured surfaces, matching the description of the oxide layer. The Al slag deposited on the floor of the missile shelter along with the U and Pu slag was likely the material from which the basic assembly casing of the warhead was manufactured, based on other weapon designs (90). Pure Al metal has a melting point of 660 ºC (91), but it is more likely one of the Al alloys was used to produce the casing because of their superior mechanical properties. Aluminum alloys generally have melting points of 500-700 ºC (91); this is well below the temperature range experienced by the internal components of the warhead during the accident, so melting of an Al casing would not be unexpected. Aluminum is commonly alloyed with Si, Fe, Ti, Cu, Ni, Cr, Ga etc., (91) at levels above the theoretical detection limit of 0.08 wt% for EDS (72). If the Al and its minor constituents could have mixed with the Pu and U during the melting process (92,93), this could explain the presence of these minor elements in the hot particles. It should be pointed out that this does not preclude environmental contamination or the use of these elements in other alloys or unidentified components as their primary source. A series of quantitative EDS mapping experiments may help clarify the origin of the minor components, and has the potential to identify the specific alloy of Al used in the warhead casing.

Additional information gathered about the BOMARC warhead and accident using the historical record is summarized below:

- The total length of the warhead assembly is estimated to be 30-90 cm from a series of redacted photographs from the accident site (8)
- The warhead was a tritium-boosted fission device
- The high explosive used in the warhead was Cyclotol
- The casing of the warhead was fabricated from Al or an Al alloy
- The warhead was not exposed to temperatures above 275 ºC for an extended period of time, but was hotter than that for a brief period
- The high explosive ignited at a temperature between 230 ºC and 275 ºC
- The temperature range experienced by the Pu and U components was between 375 ºC and 2800 ºC
- The Pu slag observed on the floor of the shelter formed at temperatures above 800 ºC
- The Am distribution in the Pu matrix may be indicative of the temperature experienced by the material
- Cracking of the oxide layer formed during Pu combustion could be the source of the hot particles
- The minor elements found in the hot particle could have been introduced by the melting and mixing of the Al casing with the Pu and U components

## 8.4 Pu Isotopics within the Historical Narrative

Analysis of the Pu isotopic distribution in the particle matrix material can be used to answer basic questions such as, whether the Pu is from a warhead or from nuclear reactor fuel, or much more specific questions such as the age of the Pu or the specific reactor type that produced it (7). From a purely technical point of view determination of the isotopic composition of a Pu matrix is a relatively straight forward task that can accomplished using a variety of techniques (7) including alpha and gamma spectroscopy, as presented in this work. Interpretation of these results is not nearly as simple a task. The following discussion of the U.S. Pu production history during the period preceding the BOMARC accident will illustrate how the knowledge of the production history of Pu can provide a context that makes it more difficult to interpret the Pu isotopic data.

From the historical record, the BOMARC accident occurred in June 1960, setting a firm upper limit for the date of the Pu production. Los Alamos estimated a date of Pu production of 1958 (14) and analysis of the hot particles by gamma spectroscopy in this work places the date of Pu production between 1955 and 1960, with a best estimate of late 1957. Based on a date of Pu production between 1955 and 1960 the technology available and facilities used to manufacture the Pu found in the hot particle matrix were identified.

In the U.S., only two facilities have been involved in the large scale production of Pu for weapons, the Savannah River Site (14) and the Hanford Site (94). In 1958, both facilities were producing Pu for the U.S. weapons

program. In 1954 the Savannah River Site made its first Pu delivery, using heavy water moderated reactors and separating the Pu from the reactor fuel exclusively using the PUREX process (95). Hanford had been involved with Pu production since the days of the Manhattan Project, and produced Pu using water cooled, graphite moderated reactors (96). Chemical separation of the Pu from the reactor fuel at the Hanford Site had been performed using three processes; bismuth phosphate precipitation, REDOX and PUREX (97). By 1958, chemical separation of Pu at Hanford was only performed using REDOX and PUREX, with PUREX accounting for 79% of its annual Pu production (97). The final product of the PUREX process is a Pu nitrate solution from which the metal was synthesized by a process of fluorination followed by high temperature reduction to metallic Pu with calcium (77). Both the Savannah River site and Hanford site produced Pu metal using this technique (77,95). The metallic Pu was then available for fabrication into weapons components at either the Hanford site or at the Rocky Flats plant.

Using the historical data, the Pu present in the hot particles was produced at either the Savannah River Site or the Hanford Site and the Pu was most likely chemically separated from the reactor fuel using the PUREX process. From this overview, identifying the source of the Pu based on the isotopic composition of the Pu should be a relatively simple; only two sites produced Pu, and each site used different reactor designs, therefore the Pu isotopic composition in the hot particles should match the isotopic signature of the production reactors from one of the sites (7).

Unfortunately, one factor that the historical Pu production data does not address in detail is the potential for recycling and mixing of Pu during weapons production. Through the mid-1950's and continuing into the 1960's there was a rapid growth of the U.S. nuclear weapons stockpile that included the retirement of older weapons (98). For example, in 1955, 806 new weapons were added to the U.S. stockpile with 87 retired; by 1960 the number of new weapons added had increased to 7,178, with 838 retired from the stockpile during the same year (98). To meet the high demand for Pu during this period (94), recycling of Pu from scraps, residue and retired weapons to meet production demands did occur (99).

As an example of Pu recycling, at the Hanford site Pu was recovered from lathe turnings, casting skulls and Pu scraps from other processes in the RECUPLEX facility (77). The RECUPLEX facility recycled the Pu by dissolving the material and then passing it through a TBP-based solvent extraction process independent of the REDOX or PUREX facilities. The Pu nitrate solution from the RECUPLEX facility was then reintroduced to the Pu finishing process (77) along with the Pu from the REDOX and PUREX facilities. The mixing of Pu from the different process streams and different reactor fuel loads would result in a blend of Pu isotopics, effectively erasing the isotopic signatures of the original sources. Although Pu recycling of retired weapons was not reported at the Hanford site, the RECUPLEX plant demonstrates that this technology was available and how it could be employed. Rocky Flats, Los Alamos National Laboratory and the Savannah River Site also had Pu scrap and residue recycling programs, and

recycling of retired weapons components was reported to have occurred at Rocky Flats (99).

In the period between 1955 and 1960 (98), assuming 100% recycling of Pu from retired weapons, and that the Pu from each retired weapon was recycled into a single weapon without further mixing of Pu, then 20-33% of the stockpile could contain recycled Pu that was from 0-10 years old at the time of weapon manufacture and could have originated from the Savannah River Site, Hanford Site or a combination of the two. In this context, interpretation of the Pu isotopics yields little concrete information about the source term of the Pu even though precise and accurate Pu isotopic measurements were made.

## 8.5 Concluding Remarks

These data sets demonstrate the utility of applying multiple techniques to forensic type analysis of nuclear materials. They also illustrate the limitations of this type of analysis when little or no background information is available about the material. Even if only basic knowledge of the manufacturing processes and purpose of the material can be combined with analytical data, a much more accurate description of the source of the material can be presented. The origin of trace contaminants can be defined with greater certainty and the conditions that formed the material can be described in greater detail leading to a better interpretation of the data. Whenever or not an unknown material is analyzed, as much effort as is put into the technical analysis should also be placed on building an accurate provenance.

BIBLIOGRAPHY


1. Wolf, S. F.; Bates, J. K.; Buck, E. C.; Dietz, N. L.; Fortner, J. A.; Brown, N. R. Physical and Chemical Characterization of Actinides in Soil from Johnston Atoll. *Environmental Science & Technology* 1997, *31* (2), 467-471.
2. DoD. *Narrative Summaries Of Accidents Involving U.S. Nuclear Weapons 1950-1980;* Department of Defense, 1981.
3. Burns, P. A.; Cooper, M. B.; Duggleby, J. C.; Mika, J. F.; Williams, G. A. *Plutonium-Contaminated Fragments at the Taranaki Site at Maralinga;* Australian Radiation Laboratory: Yallambie, 1986.
4. Zheltonozhsky, V.; Muck, K.; Bondarkov, M. Classification of hot particles from the Chernobyl accident and nuclear weapons detonations by non-destructive methods. *Journal of Environmental Radioactivity* 2001, *57,* 151-166.
5. Margulies, T. D.; Schonbeck, N. D.; Morin-Voilleque, N. C.; James, K. A.; LaVelle, J. M. A comparative study of $^{239,240}$Pu in soil near the former Rocky Flats Nuclear Weapons Facility, Golden, CO. *Journal of Environmental Radioactivity* 2004, *75,* 143-157.
6. Salbu, B.; Krekling, T.; Oughton, D. H.; 0stby, G.; Kashparov, V. A.; Brand, T. L.; Day, J. P. Hot Particles in Accidental Releases From Chernobyl and Windscale Nuclear Installations. *Analyst* 1994, *119,* 125-130.
7. APS & AAAS. *Nuclear Forensics Role, State of the Art, and Program Needs;* AAAS Center for Science Technology and Security Policy: Washington, DC, 2008, Joint Working Group of the American Physical Society and the American Association for the Advancement of Science.
8. Whitfield, J. M. *Airmunitions Letter No 136-11-56C;* Airmunitions LTR 136-11-56C; Headquaters Ogden Air Material Area United States Air Force: Hill Air Force Base, Utah, 1960.
9. Defense Nuclear Agency. DNA Case FOIA 88-106, 1990. 138.pdf. www.dod.gov/pubs/foi/reading_room/138.pdf (accessed September 18, 2009).
10. Associated Press. BOMARC Fire Laid To Helium Blast. *New York Times,* June 24, 1960, 7.
11. Rademacher, S. E.; Hubbell, J. L.; Harcek, B. G. *Boeing Michigan Aeronautical Research Center (BOMARC) Missile Shelters and Bunkers Scoping Survey Report (Volume 1);* National Technical Information Service: Springfield, VA, 2008, NTIS, 5285 Port Royal Road, Springfield, VA 22161-2103.
12. ATSDR. Public Health Assessment Boeing Michigan Aeronautical Research Center/McGuire Missile, 2002. ATSDR. http://www.atsdr.cdc.gov/hac/PHA/boeing/boe_toc.html (accessed

May 13, 2009).

13. Rademacher, S. Recent Remedial Action Success on BOMARC Nuclear Weapons Accident Site. *Wingman* 2009, *2* (2), 36-39.
14. Rademacher, S. E. *The Influence of Heterogeneity in Gamma Spectroscopy Analyis of Soil Contaminated with Weapons Greade Plutonium at the BOMARC Missile Accident Site McGuire AFB NJ;* NTIS: Springfield, Va, 2001.
15. Krane, K. S. *Introductory Nuclear Physics;* John Wiley & Sons: New York, New York, USA, 1988.
16. BNL. Chart of the Nuclides. www.nndc.bnl.gov/chart/ (accessed May 15, 2009).
17. Eriksson, M.; Ljunggren, K.; Hindorf, C. Plutonium hot particle separation techniques using real-time digital image systems. *Nuclear Instruments and Methods in Physics Research A* 2002, *488,* 375-380.
18. Ketcham, R. A.; Carlson, W. D. Acquisition, optimization and interpretation of X-ray computed tomographic imagery: applications to the geosciences. *Computers & Geosciences* 2001, *27,* 381-400.
19. Lee, M. H.; Clark, S. B. Activities of Pu and Am Isotopes and Isotopic Ratios in a Soil Contaminated by Weapons-Grade Plutonium. *Environmental Science & Technology* 2005, *39* (15), 5512-5516.
20. National Atlas of the United States. http://nationalatlas.gov (accessed September 30, 2009).
21. Szabo, Z.; Otto, Z. S.; Oden, J. H.; Rice, D. E. *Radiochemical Sampling and Analysis of Shallow Ground Water and Sediment at the BOMARC Missile Facility, East-Central New Jersey, 1999-2000;* U.S. Geological Survey: Reston, Va, 2005.
22. ONJSC. Office of the New Jersey State Climatologist. http://climate.rutgers.edu/stateclim/?section=njcp&target=NJCoverview (accessed May 14, 2009).
23. Rousseau, M.; Di Pietro, L.; Angulo-Jaramillo, R.; Tessier, D.; Cabibel, B. Preferential Transport of Soil Colloidal Particles: Physicochemical Effects on Particle Mobilization. *Vadose Zone Journal* 2004, *3,* 247-261.
24. Joacobsen, O. H.; Moldrup, P.; Larsen, C.; Konnerup, L.; Petersen, L. W. Particle transport in macropores of undisturbed soil columns. *Journal of Hydrology* 1997, *196,* 185-203.
25. Ketcham, R. A.; Carlson, W. D. About High-resolution X-ray CT. http://www.ctlab.geo.utexas.edu/overview/index.php (accessed May 22, 2009).
26. NIST. XCOM: Photon Cross Sections Database. http://physics.nist.gov/PhysRefData/Xcom/Text/XCOM.html (accessed May 22, 2009).

27. Gonzalez, R. C.; Woods, R. E. *Digital Image Processing,* 3rd ed.; Pearson Education Inc: Upper Saddle River, NJ, 2008.
28. Russ, J. C. *The Image Processing Handbook,* 4th ed.; CRC Press: New York, NY, 2002; p 591.
29. The MathWorks, Inc. Matlab Version 7.4 and Image Processing Tool Box. Natick, Ma, 2007.
30. Ketcham, R. A. BLOB3D. 2005, www.ctlab.geo.utexas.edu/software/index.php.
31. ITT Visual Information Solutions. IDL Virtual Machine. Boulder, Co 2007.
32. Vacuum Tube. http://en.wikipedia.org/wiki/Vacuum_tube (accessed September 21, 2009).
33. Renshaw, J. C.; Lloyd, J. R.; Livens, F. R. Microbial interactions with actinides and long-lived fission products. *Comptes Rendus Chimie* 2007, *10* (10-11), 1067-1077.
34. Skoog, D. A.; Leary, J. J. *Principles of Instrumental analysis,* 4th ed.; Harcourt Brace and Company: Orlando, 1992.
35. CRC. *CRC Handbook of Chemistry and Physics, 85th Edition,* 85th ed.; CRC Press: Washington, D.C., 2004.
36. McFarthy, J. F.; Zachara, J. M. Subsurface transport of contaminants. *Enivronmental Science and Techology* 1989, *23* (5), 496-502.
37. Warwick, P. W.; Hall, A.; Pashley, V.; Bryan, N. D.; Griffin, D. Modelling the effect of humic substances on the transport of Eu through porous media: a comparison of equilibrium and equilibrium/kinetic models. *Journal of Contaminant Hydrology* 2000, *42,* 19-34.
38. Hecker, S. Plutonium and Its Alloys. *Los Alamos Science* 2000, *26,* 290-335.
39. Aragon, A.; Espinosa, A.; de la Cruz, B.; Fernandez, J. A. Characterization of radioactive particles from the Palomares accident. *Journal of Environmental Radioactivity* 2008, *99,* 1061-1067.
40. Lind, O. C.; Salbu, B.; Janssens, K.; Proost, K.; Garcia-Leon, M.; Garcia-Tenorio, R. Characterization of U/Pu particles originating from the nuclear weapon accidents at Palomares Spain, 1966 and Thule, Greenland, 1968. *Science of the Total Environment* 2007, *376,* 294-305.
41. Pollanen, R.; Ketterer, M. E.; Lehto, S.; Hokkanen, M.; Ikaheimonen, T. K.; Siiskonen, T.; Moring, M.; Rubio Montero, M. P.; Martin Sanchez, A. Multi-technique characertization of a nuclear bomb particle from the Palomares Accident. *Journal of Environmental Radioactivity* 2006, *90,* 15-28.
42. Lind, O. C.; Salbu, B.; Janssens, K.; Proost, K.; Dahlgaard, H. Characterization of uranium and plutonium containing particles

originating from the nuclear weapons accident in Thule, Greenland, 1968. *Jouornal of Environmental Radioactivity* 2005, *81,* 21-32.

43. Moring, M.; Ikäheimonen, T. K.; Pöllänen, R.; Ilus, E.; Klemola, S.; Juhanoja, J.; Eriksson, M. Uranium and plutonium containing particles in a sea sediment sample. *Journal of Radioanalytical and Nuclear Chemistry* 2001, *248* (3), 623-627.
44. Ravel, B. Hephaestus Version 0.17. 2007, http://cars9.uchicago.edu/~ravel/software/.
45. Gonzalez, R. C.; Woods, R. E.; Eddins, S. L. *Digital Image Processing Using MATLAB;* Pearson Prentice Hill: Upper Saddle River, NJ, 2004.
46. Keegan, R. P.; Gehrke, R. J. A method to determine the time since last purification of weapons grade plutonium. *Applied Radiation and Isotopes* 2003, *59,* 137-143.
47. Willmes, H.; Ando, T.; Gehrke, R. J. Gamma Emission Probabilities in the Decay of 241-Pu and 237-U, Determined from the In-growth of 241-Am. *International Journal of Applied Radiation and Isotopes* 1985, *36* (2), 123-128.
48. Dragnev, T. Intrinsically Calibrated Gamma and X-Ray Measurements of Plutonium. *Applied Radiation and Isotpes* 1992, *44* (3), 613-619.
49. Glasstone, S. *An Intoduction To Nuclear Weapons;* United States Atomic Energy Commission, 1963.
50. Puphal, K. W.; Olsen, D. R. Electrodeposition of Alpha-Emitting Nuclides from a Mixed Oxalate-Chloride Matrix. *Analytical Chemistry* 1972, *44* (2), 284-289.
51. Talvitie, N. A. Electrodeposition of Actinides for Alpha Spectrometric Determination. 1972, *44* (2), 280-283.
52. Sill, C. W.; Williams, R. L. Preparation of actinides for alpha spectrometry without electrodeposition. *Analytical Chemistry* 1981, *53,* 412-415.
53. Sill, C. W. Precipitation of Actinides as Fluorides or Hydroxides for High Resolution Alpha Spectrometry. *Nuclear and Chemical Waste Management* 1987, *7,* 201-215.
54. Vapirev, E. I.; Kamenova, T. S.; Mandjoukov, I. G.; Mandjoukova. Visualization, Indentification and Spectrometry of a Hot Particle. *Radiation Protection* 1990, *30* (2), 121-124.
55. Pollanen, R.; Siiskonen, T. Direct High-Resolution Alpha Spectrometry from Nuclear Fuel Particles in an Outdoor Air Sample. 2008, *124* (4), 454-463.
56. Pollanen, R.; Siiskonen, T.; Moring, M. . J. J. Direct Alpha Spectrometry for Characterizing Hot Particle Properties. *Radiation Measurements* 2007, *42,* 1666-1673.
57. Hecker, S.; Stevens, M. Mechanical Behavior of Plutonium and Its Alloys. *Los Alamos Science* 2000, *26,* 336-355.

58. Peterson, D. E.; Foltyn, E. M. The Pu-U (Plutonium-Uranium) System. *Bulletin of Alloy Phase Diagrams* 1989, *10* (2), 160-164.

59. International Atomic Energy Agency. *The Plutonium-Oxygen And Uranium-Plutonium-Oxygen Systems: A Thermochemical Assessment;* Technical Report Series No. 79; IAEA: Vienna, 1967.

60. Haschke, J.; Stakebake, J. Handling, Storage, And Disposition Of Plutonium And Uranium. In *The Chemistry Of The Actinide And Transactinide Elements,* 3rd ed.; Morss, L., Edelstein, N., Fuger, J., Eds.; Springer: Dordrecht The Netherlands, 2008; Chapter 29, Vol. 5.

61. Mishima, J. *Plutonium Release Studies II. Release From Ignited, Bulk Metallic Pieces;* U.S. Atomic Energy Commission: Richland, 1966.

62. Grenthe, I.; Drozdzynski, J.; Fujino, T.; Buck, E.; Albrecht-Schmitt, T.; Wolf, S. *The Chemistry Of The Actinide And Transactinide Elements;* Springer: Dordrecht The Netherlands, 2008; Vol. 1, 5 vols..

63. Clark, D. L.; Hecker, S. S.; Jarvinen, G. D.; Neu, M. P. Plutonium. In *The Chemistry Of The Actinide and Transactinide Elements,* 3rd ed.; Morss, L. R., Edelstein, N. M., Fuger, J., Eds.; Springer: Dordrecht Netherlands, 2008; Vol. 2, 5 vols..

64. Mark, C.; Taylot, T.; Eyster, E.; Maraman, W.; Wechsler, J. Can Terrorists Build Nuclear Weapons? http://www.nci.org/k-m/makeab.htm (accessed November 17, 2009).

65. Boring, A.; Smith, J. Plutonium Condensed-Matter Physics. *Los Alamos Science* 2000, *26,* 90-127.

66. Okamoto, H. Ga-O (Gallium-Oxygen). *Journal of Phase Equilibria and Diffusion* 2008, *29* (6), 550-551.

67. Runde, W.; Schulz, W. Americium. In *The Chemistry Of The Actinide And Transactinide Elements,* 3rd ed.; Morss, L., Edelstein, N., Fuger, J., Eds.; Springer: Dordrecht Netherlands, 2008; Chapter 8, Vol. 2, 5 vols..

68. Okamoto, H. Am-O (Americium-Oxygen). *Journal of Phase Equilibria and Diffusion* 2006, *27* (2), 197.

69. Martz, J.; Haschke, J. A mechanism for combustive heating and explosive dispersal of plutonium. *Journal of Alloys and Compounds* 1998, *266,* 90-103.

70. Conradson, S. Where Is the Gallium? Searching the plutonium lattice with XAFS. *Los Alamos science* 2000, *26,* 356-363.

71. Conradson, S.; Schecker, J. XAFS: A Technique to Probe Local Structure. *Los Alamos Science* 2000, *26,* 422-435.

72. Reed, S. *Electron Microprobe Analysis And Scanning Electron Microscopy In Geology;* Cambridge University Press: Cambridge, 1996.

73. Means, J.; Yuretich, R.; Crerar, D.; Kinsman, D.; Borcisk, M. *Hydrogeochemistry Of The New Jersey Pine Barrens;* New Jersey

Geological Survey: Trenton, 1981.

74. Baum, E.; Knox, H.; Miller, T. *Nuclides and Isotopes Chart of the Nuclides,* 16th ed.; KNAPL Inc, 2002.

75. Thoma, D. U-6 wt.% Nb A Composite Alloy. *Nuclear Weapons Journal* 2003, 2-3.

76. McKoon, R. Characterization of U-6Nb Ingots Produced via the Electron Beam Cold Hearth Refining Process. *Electron Beam Melting and Refining State of the Art 1997 Conference*, Reno, 1997.

77. Gerber, M. Plutonium Finishing. In *History of the Plutonium Prodcution Facilities at the Hanford Site Historic District, 1943-1990;* U.S. Deparment of Energy: Richland, Wa, 2002; Chapter 2.

78. Aragon, E. *Los Alamos Source Data For B53 MOD1 Nuclear Explosive Safety Study;* Los Alamos National Laboratory: Los Alamos, 1993.

79. Sandia National Laboratories. *B53-1 Special Study Report (U);* Sandia National Laboratories: Albuquerque, 1993.

80. Gildea, P.; Brandon, S.; Brown, B.; Haroldsen, B.; Lipkin, J.; Replogle, W.; Shepodd, T.; Zanini, D. *Energetic Component Treatability Study;* Sandia National Laboratory: Albuquerque, 1997.

81. Koike, J.; Kassner, M.; Tate, R.; Rosen, R. The Nb-U (Niobium-Uranium) System. *Journal of Phase Equilibria* 1998, *19* (3), 253-260.

82. Okamato, H. Ga-Pu (Gallium-Plutonium). *Journal of Phase Equilibria and Diffusion* 2009, *30* (2), 211-212.

83. Meyer, R.; Kohler, K.; Homburg, A. *Explosives,* 5th ed.; Wiley-VCH: Weinheim Germany, 2002.

84. Mathieu, J.; Stucki, H. Military High Explosives. *Chimia* 2004, *58* (6), 383-389.

85. Volkov, E.; Paletsky, A.; Korobeinichev, O. RDX Flame Structure at Atmospheric Pressure. *Combustion, Explosion, and Shock Waves* 2008, *44* (1), 43-54.

86. Epstein, M.; Malinovic, B.; Plys, M. *Uranium Pyrophoricity Phenomena and Prediciton;* U.S. Department of Energy: Oak Ridge, 2000.

87. Haschke, J. Corrosion of uranium in air and water vapor: consequences for environmental dispersal. *Journal of Alloys and Compounds* 1998, *278,* 149-160.

88. Savannah River National Laboratory. *Uranium Metal to Oxide Conversion by Air Oxidation;* Washington Savannah River Company: Aiken, 2005.

89. Luna, R. *A New Analysis of the Vixen A Trials;* U.S. Department of Energy: Albuquerque, 1994.

90. Okamoto, H. Am-Pu (Americium-Plutonium). *Journal of Phase Equilibria* 1999, *20* (4), 451.

91. Automation Creations, Inc. MatWeb Material Property Data. http://www.matweb.com (accessed January 10, 2010).

92. Kassner, M.; Adamson, M.; Adler, P. The Al-U (Aluminum-Uranium) System. *Journal of Phase Equilibria* 1990, *11* (1), 82-89.

93. Kassner, M.; Peterson, D. The Al-Pu (Aluminum-Plutonium) system. *Journal of Phase Equilibria* 1989, *10* (4), 459-465.

94. Marceau, T.; Harvey, D.; Stapp, D.; Cannon, S.; Conway, C.; Deford, D.; Freer, B.; Gerber, M.; Keating, J.; Noonan, C.; Weisskopf, G. *History Of The Plutonium Production Facilities At The Hanford Site Historic District, 1943-1990;* U.S. Department of Energy: Richland, 2002.

95. Reed, M.; Swanson, M.; Gaither, S.; Joseph, J.; Henry, W. *Savannah River Site st Fifty;* U.S. Government Printing Office: Washington, D.C., 2002.

96. Stapp, D. Reactor Operations. In *History Of The Plutonium Production Facilities At The Hanford Site Historic District, 1943-1990;* U.S. Department of Energy: Richland, Wa, 2002; Chapter 2.

97. Freer, B.; Conway, C. Chemical Separations. In *History Of The Plutonium Production Facilities At The Hanford Site Historic District, 1943-1990;* U.S. Department of Energy: Richland, Wa, 2002; Chapter 2.

98. Cochran, T. *U.S. Inventories of Nuclear Weapons and Weapons-Usable Fissile Materials ;* Natural Resources Defense Council: Washington, D.C., 1995.

99. U.S. Department of Energy. *Linking Legacies Connecting The Cold War Nuclear Weapons Production Processes To Their Environmental Consequences;* U.S. Depatment of Energy: Washington, D.C., 1997.

# VITA

Graduate College
University of Nevada, Las Vegas

Richard Charles Gostic

Degrees:

Associate in Science, 1993
Suffolk County Community College

Bachelor of Science, Aeronautics and Applied Mathematics, 1995
Dowling College

Master of Science, Nuclear Engineering, 2002
Massachusetts Institute Of Technology

Dissertation Title: Characterization of Plutonium Particles Originating From the BOMARC Accident -1960

Dissertation Examination Committee:

Chairperson, Kenneth R. Czerwinski, Ph.D.
Committee Member, Kenton J. Moody, Ph. D.
Committee Member, Ian D. Hutcheon, Ph. D.
Graduate Faculty Representative, Gary Cerefice, Ph. D.